Application of Ab-initio Quantum Chemistry Techniques to Hypersonic Flows for Plasma Blackout Alleviation

by

Kevin M. Sabo

Submitted to the Department of Aeronautics and Astronautics
in partial fulfillment of the requirements for the degree of

Doctor of Philosophy in Aeronautics and Astronautics

at the

MASSACHUSETTS INSTITUTE OF TECHNOLOGY

May 2022

Author . . . .
Department of Aeronautics and Astronautics
May 6, 2022

Certified by. . . . .
Wesley L. Harris
C. S. Draper Professor of Aeronautics and Astronautics
Thesis Supervisor

Certified by. . . . .
William H Green
H. C. Hottel Professor in Chemical Engineering
Thesis Committee Member

Certified by. . . . .
Mark Drela
T. J. Kohler Professor of Aeronautics and Astronautics
Thesis Committee Member

Certified by. . . . .
Dr. Gregory Power
Thesis Committee Member

Accepted by. . . . .
Jonathan P. How
R. C. Maclaurin Professor of Aeronautics and Astronautics
Chair, Graduate Program Committee

Application of Ab-initio Quantum Chemistry Techniques to Hypersonic Flows for Plasma Blackout Alleviation

by

Kevin M. Sabo

Submitted to the Department of Aeronautics and Astronautics
on May 6, 2022, in partial fulfillment of the
requirements for the degree of
Doctor of Philosophy in Aeronautics and Astronautics

Abstract

Plasma blackout in hypersonic flows produced by weakly-ionized air plasma sheaths is a phenomenon that attenuates or completely blocks communications with vehicles flying in a high-enthalpy flow environment. The ability to mitigate this issue can be useful from various re-entry vehicles to in-atmosphere hypersonic vehicles, especially with aerospace largely pushing into the hypersonic field across the industry.

This thesis asks how effective are electrophilic compounds at reducing the number density of electrons within a hypersonic plasma sheath environment. This reduction in the electron number density reduces the critical plasma frequency, thus allowing for the successful propagation and transmission of electromagnetic signals.

This work presents three contributions. First, a framework is proposed for the construction of viscous hypersonic chemistry models using *ab-initio* quantum chemistry techniques, which accounts for both spin-adiabatic and spin-nonadiabatic chemical processes. Next, an analysis is performed on the pressure-dependence of the chemical reactions that are typically seen in hypersonic flow environments, showing that pressure-dependent chemical rate coefficients are a key aspect in these environments and thus should not be ignored. Lastly, a first principles approach to assessing the feasibility of such a system and the resulting sizing requirements is presented, including a method for identifying and calculating the predominant chemical timescales which govern the electron quenching process. Together, these contributions provide a fundamental way to model and solve the problem of alleviating plasma blackout using electrophilic compounds.

Thesis Supervisor: Wesley L. Harris
Title: C. S. Draper Professor of Aeronautics and Astronautics

Acknowledgments

First, I would like to thank and acknowledge the Draper Scholar Program for providing financial and technical support over the past few years. The many fruitful opportunities, discussions, and sharing of ideas provided for a valuable learning experience that only served to augment the overall MIT experience.

Mom and Dad, while our many discussions throughout the past few years have sometimes reflected on how we have had a modest and comfortable life, you both definitely sacrificed for me to get me to this place in life, not only in terms of resources, but also in terms of time. I know you both joked and teased about me getting into some top-notch school ever since I was born, but who would have ever thought I'd be writing and thanking you both in an acknowledgments section of a PhD thesis from MIT? Pretty cool, right? Not many parents have accomplished what you have both done in raising a child and helping him find his way to one of the top engineering schools in the world. I hope I can replicate that level of love and guidance for my kids in whatever they choose to do and hopefully give them an even better life than you both gave me, but that will prove to be a challenge due to how high you both set the bar. I love you both and truly can't express that enough.

To my labmates - Dominique, Lee, Chelsea, Geoff, Vaishnavi, Carter, and Ben - I can't thank you all enough for the countless fruitful discussions about both work and non-work related stuff. Thank you all for being there for me on a daily basis and keeping me sane in this immensely stressful environment. I can write so many great things about each of you, but I only have so much real estate in this document before it becomes a risk of starting another lumber price explosion due to the immense paper usage that would result. You've all helped me become a better engineer, scientist, and person, offering me so many rich and diverse perspectives on so many different topics relating to both work and life. It is impossible for me to envision any reality in which I'm successful in this work without you all.

To my many friends, of whom I am now realizing it is impossible to list you all without inevitably forgetting someone, this work would not have happened without

your constant support as well. From the many problem sets, phone calls, nights on Discord, hours-long Zoom calls, gym sessions, dunk sessions, dinners, rock climbing outings, Dominion matches, vacations and travels, Celtics games (*shudders in Lakers gear*), the list goes on... these fun and memorable experiences are what I will remember from my time here at MIT. It's been quite the unforgettable experience, and one that I will always cherish.

To Dave and Todd, I told you both that you would get your own paragraph in here. Thanks for being lunch buddies throughout the years. You've both taught me many things about engineering outside the classroom as well as about life in general. While a lot of my coursework has shaped and molded how I think about engineering problems, you have both tempered my thought process and taught me the important practical lessons that are absolutely necessary for being a successful engineer. From the late nights doing 62x experiments to bowing an airfoil strut, to eating lunch and talking about the most random things on our minds, you've both been nothing short of an crucial, integral part to my reaching this culminating point in my MIT career.

To my committee, I've known all of you for years now. Mark, we've worked together since my junior year here at MIT, back when you had the magical mustache that was rumored to hold all of your powers as AlphaMan. From the BLI experiments to the wind-tunnel refurbishing to the debates as to who can bake a better baked good, you've been nothing short of amazing as a mentor and friend. Bill, I remember walking into your office not knowing anything about chemical kinetics, anxious out of my mind, and now I'm here writing a thesis involving chemical kinetics! Thank you for taking me under your wing, and not only having the confidence in my ability to learn the incredibly rich subject matter involved in chemical kinetics modeling, but giving me that confidence to do so. Your approachability and kindness is something that I will attempt to always replicate throughout my future career. Greg, thank you for being one of the best bosses I've had thus far in my career. You taught me the ropes of modern hypersonic analysis and introduced me to the wonderful world of beer brats. When you open your dream brewery, let me know and I'll be sure to buy a keg from you!

Lastly, to Wes. I met you during my freshman year and have worked with you ever since, despite you nearly breaking my hand with your death grip of a handshake when we first met! It has been a long ride, and one you have been a part of since effectively day one. You set me on a path for success ever since undergrad, even when I couldn't fully understand or envision it, and still probably wouldn't have believed it even if I could have done those things. You've taught me how to think about both engineering and life, asking questions that get to the heart of issues and constantly push the boundaries of my capabilities. I've had the privilege of standing on the shoulders of giants here at MIT, and I'm proud to have had the privilege of viewing the world from yours. The privilege I have had to be under your tutelage for so long cannot be overstated, and I can't thank you enough for your unwavering support in my endeavours - past, present, and future.

Contents

List of Figures

List of Tables

Listings

Chapter 1

Introduction

1.1 Motivation for Studying Hypersonic Flows

1.1.1 Science Motivation

The modeling of the hypersonic environment around an aircraft presents a unique environment in which chemical reactions may occur. These chemical reactions add a few new elements to the study of aerodynamic flows.

The first of these elements is that of tracking the time rates of change of chemical species that exist in the flow field about a hypersonic body or vehicle. These chemistry phenomena lead to a variety of rich problems, such as plasma blackout and potential methods for alleviating it [1], development of state-of-the-art simulation tools for the complex hypersonic environment [2], as even for determining the potential source of precursor molecules for the formation of life [3].

A second element is the addition of new scaling dependencies, namely the wide array timescales. The chemical reactions occur over a wide range of timescales, often times much faster than an equivalent fluid timescale. Also, the activation of internal energy modes within the atoms and molecules that constitute a hypersonic gas and how slowly or quickly they relax becomes crucially important for both physical and numerical reasons. The timescales give way to interesting flow regimes, such as chemical equilibrium or non-equilibrium flows, or even chemically frozen flows. Upon

activating new energy modes, local thermodynamic non-equilibrium also becomes a key phenomenon as the vibrations of molecules govern their reactivity and ultimately affect how quickly chemical reactions may occur.

A third element is readily viewable by examination of the governing equations of hypersonic flows: the addition of chemistry stiffens the governing equations [4, 5] leading to the requirement of having numerical schemes that are built for handling stiff partial differential equations, all while capturing the required timescales, and generating a solution in a reasonable amount of time, particularly for large domain, steady-state solutions [5].

The thesis of this work aims to explore deeply and extend the work done by Good and Rossi [1] and Good [6]. The scientific motivation pertains to that of using *ab-initio* quantum chemistry methods - those methods requiring only the inputs of physical constants and fundamental principles - in order to generate a chemical model for the complex chemistry of sulfur and fluorine gas compounds mixed with high-temperature air in a hypersonic flow environment. On the one hand, the goal of the work is to show the utility of modern *ab-initio* techniques in their predictive performance, particularly for hypersonic flows. On the other hand, the goal of the work is to not only verify, but extend the initial solution by Good and Rossi [1] for alleviating plasma blackout and the associated loss of telemetry signals from hypersonic vehicles, as well as to also provide a high-fidelity modeling framework for the chemistry and associated data required for such a solution.

1.1.2 Engineering Motivation

The engineering motivation for this work stems from the phenomenon of plasma blackout and its associated telemetry loss. Recent planetary exploration missions, such as the Mars Pheonix Lander (2008) and the Mars InSight Lander (2018), have prolonged periods of telemetry loss in flight due to the presence of a high number density of electrons about the signal transmitter. This phenomenon is frequently referred to as *plasma blackout*.

The loss of telemetry for a planetary science lander is a planned event [7]. Thus,

losing telemetry in regards to descent trajectories and entry dynamics will not compromise the success of the mission. However, losing telemetry data in sustained hypersonic flight may result in mission failure, in particular for a hypothetical situation in which an autonomous vehicle needs mission planning (e.g. flight path) updates while in flight. In the rare and unfortunate event of a mission loss during a telemetry blackout period, the ability to transmit critical data up until mission loss for analysis could prove useful for future missions success.

Hypersonic systems have recently come to the forefront of research again and are gaining support [8]. These systems vary from reentry systems to boost-glide systems to scramjet powered systems. One design goal for some of these systems is to fly from one location to another across the planet in as little as an hour. For a scramjet, in-atmosphere system, to achieve this goal will require the ability to fly at around Mach 8 to Mach 10, or perhaps even higher. At these speeds, plasma sheaths may develop at certain altitudes due to the inherently high total enthalpies in the flow-field and generate high electron number densities, potentially disrupting telemetry and other communication systems in the process.

Good and Rossi [1] offered a novel solution to this problem: use eletrophilic elements - elements which readily attach to free-electrons - to quench the plasma sheath and lower the electron density, ultimately reducing the signal attenuation. This work aims to explore with greater fidelity the feasibility of such a system. By using ab-initio techniques to develop an improved electrophilic compound gas chemistry model for existing computational fluid dynamics (CFD) codes, a useful methodology for assessing the feasibility of such a solution will be developed. This methodology will offer engineers the capability to generate a viscous hypersonic chemistry model from *ab-initio* techniques, simulate a hypersonic environment with electrophilic compounds, and determine if such an electron quenching system is feasible for mitigating signal attenuation via a first principles approach.

23

1.2 Background

Hypersonic aerodynamics provides a complex field full of unique and physics-rich topics that regularly requires multiple disciplines in order to solve a problem, both in the scientific and engineering aspects.

Recently, the United States government, as well as much of the world, has regained interest in hypersonics [8]. A desired system that is worth highlighting is that of a scramjet powered aircraft. These aircraft will fly at speeds of Mach 5 and higher, being subjected to a potentially high-enthalpy, chemically reactive environment. This complex environment, depending on the mission profile, may produce electrons from chemical reactions that can attenuate or outright block telemetry and other communication system signals. It regularly requires a multi-disciplinary approach to accurately characterize this complex environment [9, 10].

Jung et al [11] simulate both the hypersonic environment of a plasma sheath and a transmitter signal (EM wave) around the Atmospheric Reentry Demonstrator (ARD) capsule for multiple flight altitudes, orientations, and boundary conditions. They utilize an implicit, finite volume CFD code for their fluid simulations and assume a laminar, steady, thermochemical nonequilibrium flow field. They also utilize the frequency-dependent finite-difference time-domain method for electromagnetic (EM) waves in order to simulate the propagation of a 2.267 GHz signal - the link frequency used between the ARD and its tracking and data relay satellite. As one representative case, they investigated an axisymmetric model and compare the simulated results with that of the experimental test flight of the ARD capsule.

Figure 1-1 shows the number density of electrons, n_e, within the simulated plasma sheath around the ARD vehicle. The dark red bands display the critical electron number density at which the signal is completely blocked by the electrons. Figure 1-2 displays the simulated EM wave transmitted by the transmitter and its propagation into the surroundings of the ARD. One clearly sees the EM waves are blocked and reflected by the critical (dark red) bands of the electrons referenced to in Figure 1-1.
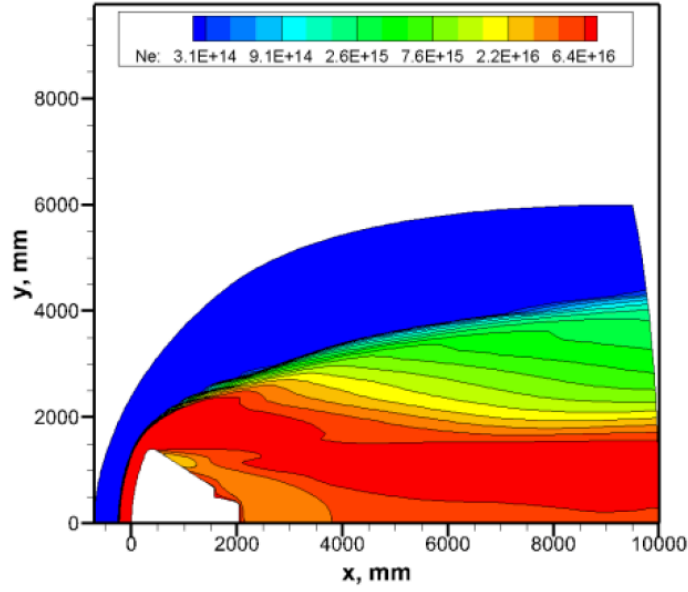
Figure 1-1: Number density of electrons n_e for the axisymmetric simulation by Jung et al.[11] The dark red and orange bands show the critical electron density at which the transmitter signal is completely blocked by the electrons.

a) x-y plane
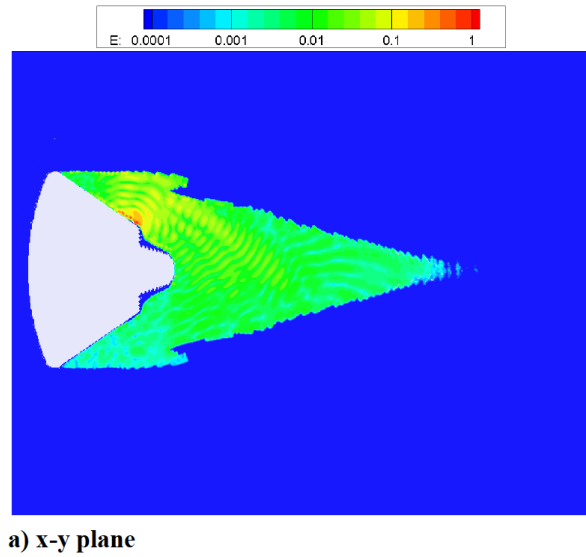
Figure 1-2: Propagation of EM signal from transmitter (located at bright orange and red spot on shoulder of vehicle).

Jung et al[11] state that, for their three-dimensional models, there are discrep-

25

ancies between the simulations and the experimental data, explicitly stating that "these discrepancies may come from the uncertainty of reaction models of associative ionizations" and that "it is necessary to do further study about this issue." While modern design tools exist that simulate hypersonic plasma sheaths and the EM wave propagation within these plasma sheaths, there is still work to be done in increasing the fidelity of these models, especially with regard to the chemical kinetics modeling.

This research addresses the plasma blackout problem and identifies a solution through the use of electrophilic compounds to quench the flow field of electron content. It will be shown in section 1.2.1 that reducing the electron number density (e.g. quenching the electrons) is the required solution for alleviating the plasma blackout problem. In order to alleviate plasma blackout, a marriage of hypersonic aerodynamics with *ab-initio* chemical kinetics modeling is used to develop a framework for constructing a viscous hypersonic aerothermochemical model using modern theoretical and computational techniques. Dimensionless parameters and length and time scales required for the alleviation of plasma blackout via electrophilic compounds will be derived based on the results produced from this framework.

1.2.1   The "Plasma Blackout" Problem in Hypersonic Plasma Sheaths

The "plasma blackout problem" is a problem that still is encountered today with spacecraft on reentry [7]. However, future in-atmosphere hypersonic vehicles may also have to contend with this problem. A variety of systems have been proposed to tackle this problem, some of which Jung et al [11] identify from other various authors. The proposed solutions listed are:

- wave frequency modification (of the telemetry signal transmitter)

- shape modification of the leading-edge of a reentry vehicle

- E $\times$ B layer

- magnetic window through the plasma sheath

Curiously, there is no mention of the use of electrophilic elements for the quenching of electrons in their work.

It is critical to understand why electrons and the quenching of electrons are the key target of this proposed work. Starkey[12] develops a model to study the phenomenon of telemetry blackout in the context of air-breathing hypersonic vehicle safety. The critical component of the model is that of the *plasma frequency*, ω_p, the frequency at which a signal of equal or lesser frequency will be attenuated (partially lost) or blocked (completely lost). This plasma frequency is defined as:

$$\omega_p \equiv \sqrt{\frac{n_e q_e^2}{\epsilon_0 m_e}} \tag{1.1}$$

with n_e the electron number density, q_e the charge of an electron, ϵ_0 the permittivity (dielectric constant) of free space, and m_e the mass of the electron. What is also critical to note is that any equivalent ion frequency, ω_i, is of the same form:

$$\omega_i \equiv \sqrt{\frac{n_i q_i^2}{\epsilon_0 m_i}} \tag{1.2}$$

where i indicates the particular ionic species evaluated. Dividing equation 1.1 by equation 1.2 yields

$$\frac{\omega_p}{\omega_i} \sim \sqrt{\frac{m_i}{m_e}} \sim \mathcal{O}\left(10^2\right) \tag{1.3}$$

indicating that the smaller mass of the electron dominates the signal attenuation capability of the plasma. An analogous way to think about this phenomenon is that the much smaller electron can "move" more quickly to attenuate or block the signal as compared to a heavier ion of the same equivalent charge. For the analogy, take the author as an EM signal from a typical microwave telemetry transmitter ($f \sim \mathcal{O}(10^9)$ Hz) and the reentry vehicle's plasma sheath ($n_e \sim \mathcal{O}(10^{16})$ electrons / m^3) as an NBA defense. The author has no hope of penetrating the defense to score, whereas if the defense has a few less people or is relatively out-of-shape (reduced electron number density or higher masses of negative charge, respectively), or if the author were Giannis Antetokounmpo (a high energy EM wave) and could simply barrel

27

through the defense, the issue of scoring (successfully transmitting the signal) would be moot.

Lin et al [10] also discuss electromagnetic wave propagation in a plasma sheath and how it relates to the plasma frequency, but also develop scaling laws that govern the decay of the electron number density under different chemically reacting flow conditions. For chemically frozen flow about a conical body with non-catalytic walls and no ingestion of electrons from the inviscid flow regions behind the shock, the electron density is found (via conservation of mass and assuming laminar boundary layer flow) to decay as $x^{-2.5}$:

$$n_e \sim R_N^3 x^{-2.5} \tag{1.4}$$

where R_N is the nose radius. Under equilibrium flow conditions, the plasma concentration can be obtained from a Mollier Chart.

Blottner [13] also developed electron number density scaling laws. Blottner showed that for conical bodies with non-catalytic walls, when associative ionization reactions are frozen, the electron decay rate scales as $(x/R_N)^{-1.5}$. For a frozen boundary layer flow along a conical body with a catalytic surface, the scaling of the decay rate increases to $(x/R_N)^{-2.5}$.

Levinsky and Fernandez [14] explore distances of $x/R_N \geq 200$ downstream of the nose where the loss of electrons via diffusion and dilution is overtaken by the production of electrons in the peak temperature regions of the boundary layer (which has sufficiently enveloped the entropy layer by this point [10]). The results obtained by Levinsky and Fernandez approximate that the electron production scales as $(px/u_s)^3$. Here, p is the surface pressure, x the downstream distance, and u_s the surface velocity. This approximation is only valid under the assumptions that recombination, reattachment, and dissociative cooling can be neglected, and that only forward reactions are considered with no depletion of the reacting molecular species. However, even under these strict assumptions, the results are useful up until equilibrium is approached further downstream, where the scaling laws must be modified.

Even with the benefits suggested by the scaling analyses, more can potentially be done to improve the reduction of the electron number density. One such way is the use of electrophilic compounds, as previously mentioned. Good [6] and Good and Rossi [1] have studied electron attachment in thermally ionized air via the use of fluorine. Fluorine is the second most electrophilic elements and its hexafluoride compounds (e.g. SF_6, WF_6) are some of the most electrophilic compounds candidates (refer to Shui et al [15] for their surveying of electrophilic compound candidates). Good and Rossi [1] have experimentally determined rate coefficients for a few reaction pathways involving SF_6 and F. In their work, electron attachment occurs via a three body attachment reactions:

$$F + e^- + M \rightleftharpoons F^- + M \tag{1.5}$$

and via dissociative attachment reactions such as

$$SF_6 + e^- \rightleftharpoons SF_5^- + F \tag{1.6}$$

Another important reaction is the rate-limiting step of the dissociation of SF_6:

$$SF_6 + M \rightleftharpoons SF_5 + F + M \tag{1.7}$$

Experimentally determined rate coefficients (e.g. shocktube experiments, electron beam experiments for measuring attachment cross-section) and recommendations for other unexplored reactions (e.g. oxidation reactions with SF_6) are given in Good and Rossi [1]. The main mechanisms discussed for the effectiveness of reattachment pertained to using SF_6 to cool a region of the flow via injection and allow for electron reattachment to occur within this cooled region. When done in an expanded flow region, which is relatively cool compared to the stagnation region of a vehicle such as a capsule, the process was shown to work over a range of altitudes, shown in Figure 1-3.
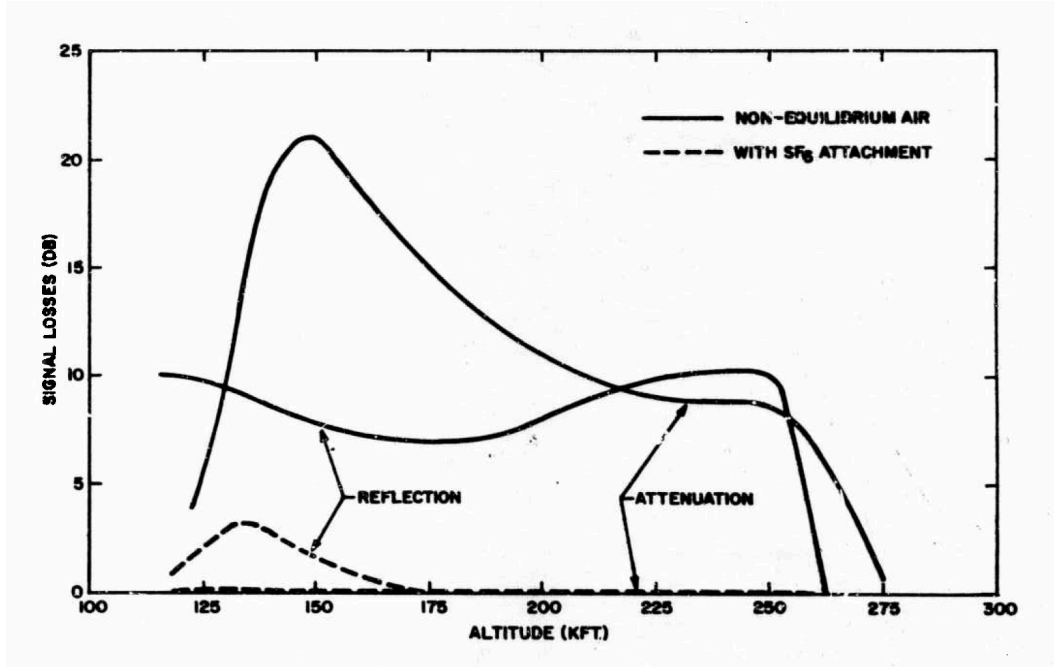
Figure 1-3: Signal loss as a function of altitude for the Trailblazer II vehicle by Good and Rossi [1]. Non-equilibrium air with and without SF_6 attachment is shown, clearly indicating the potential for electrophilic electron quenching.

While Good and Rossi [1] claim that plasma blackout alleviation via electrophilic compounds is feasible, Good and Rossi state that "a detailed design is now required" to develop the system. Given their recommendation to study other reactions, such as oxidation reactions with SF_6, and that modern day detailed designs and analyses rely heavily on computational tools, a detailed model of non-equilibrium electrophilic chemistry (air and SF_6 compounds), as well as the transport coefficients for such species for viscous computations, needs to be developed for an arbitrary hypersonic vehicle configuration (i.e. in- or trans-atmospheric hypersonic vehicle [8]) in order to validate their original claim. Such a detailed chemistry model can also be used in the plasma blackout analyses conducted by folks such as Jung et al [11] and Takahashi et al [16].

1.2.2 *Ab-Initio* Methods for Electrophilic Compounds in a Hypersonic Flow Environment

Ab-initio methods have been investigated in hypersonic chemistry modeling within the past decade. Some of the more recent works will be discussed here as these works give a general overview of what the current hypersonic *ab-initio* chemistry field looks like [17, 18, 19, 20].

Andrienko and Boyd[17] investigated O_2-N collisions using *ab-initio* techniques. Quasi-classical trajectory (QCT) calculations and Master Equation simulations are used on the two lowest *ab-initio* potential energy surfaces (PESs) to study the reaction system of:

$$O_2 + N \rightarrow NO + O \tag{1.8}$$

with particular focus on the rovibrational (rotational and vibrational energy state dependent reaction) relaxation and dissociation of molecular oxygen, as well as other relaxation rates that are found to be important above 8000K. Equation (1.8) is a non-rate-limiting step of the Zel'dovich mechanism [21] in the overall reaction of

$$N_2 + O_2 \rightarrow 2NO \tag{1.9}$$

Uncertainties lie in the overall reaction rate of Equation (1.9), but more particularly in Equation (1.8) at moderate altitudes and moderate hypersonic speeds. At these lower speeds and altitudes, O_2 is present in larger concentrations, thus the necessity to properly model the reaction rate of equation (1.8). Using *ab-initio* generated PESs, Andrienko and Boyd probe the reaction system and propose a new Arrhenius curve-fit for the reaction rates of equation (1.8) over a temperature range of 3000K - 20,000K, with advised cautionary use at temperatures above 10,000K due to the breakdown of a non-equilibrium quasi-steady state assumption (details seen in Andrienko and Boyd [17]).

In 2017, Andrienko and Boyd[18] simulate the vibrational energy transfer in O_2-N_2

collisions using QCT on an *ab-initio* PES. These relaxation time results were compared against experimental data and the empirically derived correlation of Millikan and White [22], displaying mixed results. At lower translational temperatures below 10,000K, the master equation simulations show good agreement with data and the Millikan and White correlation; however, at larger translational temperatures of 15,000K, there was a roughly 20% decrease in the relaxation time produced by the master equation simulation and disagreement with the Millikan and White curve-fit. While Andrienko and Boyd demonstrate the insights that the master equation simulation with QCT calculations along ab-initio PESs can produce, there is still clearly much work to be done when it comes to predicting specific chemical reaction rate quantities, such as vibrational relaxation times, especially at very large translational temperatures which are often encountered in hypersonic flows.

Valentini and Schwartzentruber [19] use a different methodology to that of Andrienko and Boyd [17, 18]. Valentini and Schwartzentruber calculate the collision processes of N + N_2 and N_2 + N_2 using a process called direct molecular simulations (DMS). They show that N_2 + N_2 relaxation times agree quite well with the Millikan and White correlation [22], but the relaxation times for N + N_2 have about an order of magnitude discrepancy. They also compare other results from these DMS studies to QCT results, showing some slight discrepancies between the two approaches. Regardless, many CFD solvers today use the Millikan and White vibrational relaxation time model, despite its inconsistencies.

However, the objective of Valentini and Schwartzentruber [19] was to take the *ab-initio* methodology one step further and integrate it into a CFD solver. They fit the results from the DMS by using a Millikan-White-type expression [19, 22]:

$$p\tau_{v,i} = exp\left[A_i\mu^{1/2}\theta_v^{4/3}\left(T^{-1/3} - 0.015\mu_i^{1/4}\right) - C_i\right] + p\tau_{c,i} \tag{1.10}$$

where i indicates the reaction pathway being modeled (either N + N_2 or N_2 + N_2) with its associated constants, and the high-temperature correction term

32

$$p\tau_{c,i} = \frac{k_b T_t}{\sigma_i \bar{c}} \tag{1.11}$$

where $\bar{c}$ is the average relative speed from kinetic theory, and

$$\sigma_i = \sigma_v \left(\frac{50,000[\text{K}]}{T_t} \right) \tag{1.12}$$

where σ_v is a characteristic vibrational cross-section. The corresponding fits from DMS are valid between 6000K and 40,000K. This relaxation time can be inserted into the vibrational energy conservation equation for a particular species i. This capability negates the need for Park's [23] two-temperature model with all vibrating species using the same vibrational temperature, because if one has accurate data from DMS or another *ab-initio* method for each individual vibrating species i, then they may simulate the vibrational energy conservation for each individual vibrating species i.

Chaudhry et al [20] present a method for implementing a microscopic description of gas behavior into CFD, particularly for that of the nitrogen ensemble studied by Valentini et al [24] and Valentini and Schwartzentruber [19]. This microscopic description of the gas is then integrated to yield the macroscopic quantities of interest using a Boltzmann distribution. Chaudhry et al use a hypersonics CFD code to compare updated chemical kinetics models for rate coefficients and vibrational energy source terms using *ab-initio* data. The CFD results are then compared to the DMS results to verify the accuracy of the updated chemical kinetics models from the CFD. Chaudhry et al find that simply updating the CFD models to use DMS (and/or QCT) data does not yield a match with the DMS results because the vibrational energy distributions of a dissociating gas ensemble are non-Boltzmann. They suggest that fitting the *ab-initio* data to a non-Boltzmann distribution of particles should fix the mismatched results between the CFD and DMS. Therefore, the building of chemical models, particularly for those of dissociating gases, in this proposed work will use non-Boltzmann distributions when calculating required macroscopic properties when at sufficiently high vibrational energy levels.

There clearly exists work to be done in regards to atomic-atomic, atomic-diatomic, and diatomic-diatomic chemical reactions. However, no work in *ab-initio* hypersonic non-equilibrium chemistry modeling has been seen to date with more "exotic" poly-atomic compounds, such as sulfur-hexafluoride (SF_6). This modeling of SF_6 using *ab-initio* techniques provides insights into electron quenching in a hypersonic plasma sheath, particularly which reactions and compounds the electrons are most sensitive. The modeling also provides insights into other physical assumptions and mechanisms in *ab-initio* chemical modeling and in its future applications to hypersonic flows.

1.3   Thesis Definition and Contributions

As previously identified in Section 1.2, quenching electrons in a hypersonic plasma sheath alleviates the plasma blackout problem and reduces signal attenuation and loss. A schematic of a hypersonic plasma sheath around a blunted cone can be seen in Figure 1-4. The solution to this plasma blackout problem will be of use to future hypersonic vehicles in situations where telemetry contact is a top priority.
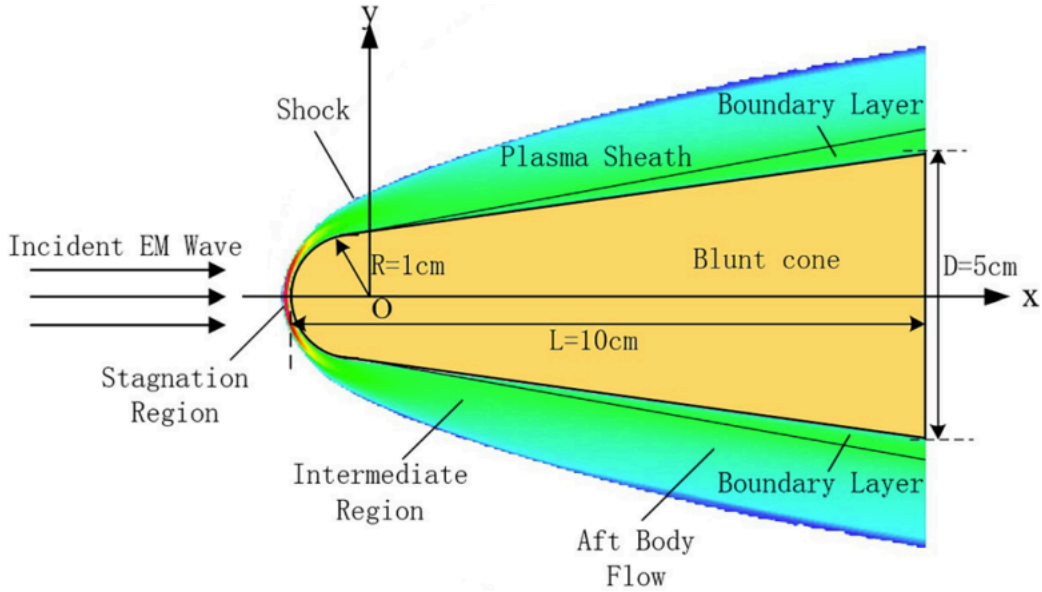
Figure 1-4: Schematic of a hypersonic plasma sheath about a blunted cone, courtesy of Sun et al [25].

The goal of this proposed thesis work is threefold. First, an investigation into the dimensionless parameters, length, and time scales that govern the quenching of electrons via the use SF_6 is carried out to assess the feasibility of utilizing SF_6 for alleviating plasma blackout. Second, key modeling assumptions related to the chemical reaction rate coefficients, such as non-pressure dependent chemical reactions, will be relaxed in an effort to increase the fidelity of the chemistry modeling. Third, the use of *ab-initio* methods in quantum chemistry will be employed to facilitate the calculations of reaction rate coefficients and other macroscopic quantities of interest, such as transport coefficients, in order to provide a *ab-initio* framework for generating viscous thermochemical non-equilibrium models.

The use of dimensionless parameters, length, and time scales gives a high-level view of the processes at play in this problem. Fundamental concepts are employed in a Damköhler number analysis in order to assess the use of a SF_6 injection system for a simple capsule geometry. This analysis shows the fundamental timescales associated with the electron quenching process, based on the chemistry being used for

the alleviation, and the process for sizing such a system with respect to the chemical modeling.

Pressure dependence is explored for the reaction rate coefficients. The stagnation, intermediate, and aft body regions of the hypersonic plasma sheath differ in pressure and temperatures. The pressure often differs by several orders of magnitude and the temperature differs by one or two orders of magnitude. The magnitude of these differences depend on free stream conditions, vehicle shape, and flight Mach number. The chemical rate coefficients have low and high-pressure limits and a smooth, highly non-linear, pressure dependent "fall-off" region between them. Where the "fall-off" region begins and ends is a function of both pressure and temperature, but the whereabouts of this region for chemical reactions in hypersonic flow environments has not been seen in literature. This pressure dependence may affect the production and depletion of electrons and other chemical species, all of which must be properly accounted for in this work. This work shows that the rate coefficients depend on pressure for unimolecular reactions, and these reactions are firmly in the low-pressure region, thus requiring collision partners to thermally deactivate the excited unimolecular compounds.

The use of *ab-initio* quantum chemical methods to construct and calculate chemical rate coefficients and macroscopic quantites will be employed for this thesis work. A methodology for hypersonic chemists will be developed for the construction of hypersonic chemistry models without access to experimental data for both spin-adiabatic and spin-nonadiabatic reactions. A method for computing transport coefficients via collision integrals utilizing *ab-initio* data is also briefly presented, with recommendations for how to achieve accurate results.

1.4   Outline of Thesis Document

Chapter 1 has been seen to be an overview of the motivation and background to the plasma blackout problem. The literature review identifies plausible pathways forward to alleviating plasma blackout, but focuses primarily on the idea of using electrophilic compounds to quench free-electrons, which are the primary cause of blackout. With

the idea of using electrophilic compounds as the main solution path identified, the review focuses on the work that has been done on the plasma blackout problem to date. Afterwards, a review of hypersonic aerothermochemical modeling and *ab-initio* chemical kinetics modeling techniques shows the plausibility of modeling this proposed solution to the plasma blackout problem. Finally, the literature review shows the identification of key gaps along the way that must be addressed in order to produce a high-fidelity model within the framework of the overarching modeling methodologies relating to hypersonic thermochemical non-equilibrium flows and plasma blackout.

Chapter 2 details the viscous thermochemical non-equilibrium (TCNE) modeling for the aerothermodynamic portions of this work. It will detail the "guts" of the CFD physics modeling implemented into MIT's Solution Adaptive Numerical Simulator (SANS). The *ab-initio* chemical kinetics modeling will be discussed in the next chapter, as the TCNE model discussion operates on the pretext that the chemical rates have already been supplied. At the conclusion of this chapter, assuming the rates have already been supplied, a methodology will have been presented and summarized to effectively allow for the complete modeling of a viscous TCNE flow from scratch. The calculation of chemical reaction rates is the subject of the next chapter, which will allow for the relaxation of needing a supplied rate, completing the methodology outright.

Chapter 3 focuses on the *ab-initio* chemical kinetics modeling for the new chemical reactions that are considered for the sulfur hexafluoride in air low-temperature plasma model. This discussion will pertain to the calculation of the actual chemical reaction rate coefficients. The bulk of the reactions pertain to what are labeled the "interfacial" reactions that create compounds containing sulfur, fluorine, oxygen, and nitrogen compounds, and combinations thereof. Discussion of the models used for predicting the chemical rate coefficient, k, and their limitations is the primary focus of this chapter.

Chapter 4 outlines the tooling used for the computations, the theory of which is briefly mentioned in the previous chapters. First, the CFD solver being utilized is the Solution Adaptive Numerical Simulator (SANS) developed by Professor David

Darmofal's group here in MIT's department of Aeronautics and Astronautics. Next, the quantum chemistry packages used will be discussed and are those of Gaussian, Inc. [26] and GAMESS [27]. Lastly, the tools used for calculating the rate coefficient data from the quantum chemistry outputs are those of Arkane in the RMG suite [28] developed by Professor William H. Green's Group here in MIT's department of Chemical Engineering, and that of NAST [29, 30] developed by Professor Sergey Varganov's group at the University of Nevada, Reno.

Chapter 5 presents the results and analysis of the *ab-initio* quantum chemistry results and the resulting chemical kinetic rate coefficients for the "interfacial species" that tie together the air-plasma and SF_6 plasma models. The pressure dependence of such reactions will be assessed, and the resulting temperature and pressure bounds will be stated and discussed.

Chapter 6 presents a 2D TCNE multi-component Euler model utilizing a simplified Atmospheric Reentry Demonstrary (ARD) geometry model for 11-species air. The air-SF_6 model is used in the context of a 0D reactor model with inputs for the air-plasma composition taken from the ARD model results. The results are then presented in the context of a defined Damköhler number, which provide engineering guidance on the use of such an electrophilic compound system for the alleviation of plasma blackout.

Chapter 7 concludes the thesis by discussing the feasibility of electrophilic compound injection for the alleviation of plasma blackout. It also identifies future work paths for both scientific and engineering research in the realms of both plasma blackout and *ab-initio* quantum chemical methods for use in hypersonic flows.

Chapter 2

Hypersonic Thermochemical Non-equilibrium Modeling

2.1 Overview and Assumptions

The viscous thermochemical non-equilibrium (TCNE) model for a two-temperature hypersonic flow is presented in this section. The two-temperature model framework is primarily inspired by Gnoffo et al [31], with several extensions applied to the chemical modeling and transport coefficient modeling as presented in the following subsections. The use of a two-temperature model allows for the simulation of local thermodynamic non-equilibrium effects, both for the thermodynamics of the flow field as well as the chemical kinetics in the form of preferential-dissociation models.

2.2 Governing Equations

This section presents the governing equations used in the TCNE model implemented in SANS. The terms will be defined, and the components that make up those terms explained in further detail in the sections that follow.

2.2.1 Species Conservation

Each species requires its own conservation equation of the following form:

$$\underbrace{\frac{\partial \rho_s}{\partial t}}_{(1)} + \underbrace{\nabla \cdot (\rho_s \vec{u})}_{(2)} = \underbrace{\nabla \cdot (\rho D_s \nabla y_s)}_{(3)} + \underbrace{\dot{w}_s}_{(4)} \tag{2.1}$$

Term (1) monitors the unsteadiness of a particular species, s density within an element, while term (2) monitors the flux of species s across the element boundaries. Term (3) models the diffusion of species s across element boundaries. Finally, term (4) models the production/depletion of species s within an element.

The species production term is expressed via the law of mass action as:

$$\dot{w}_s = (10^6) M_s \sum_{r=1}^{N_r} (\nu''_{s,r} - \nu'_{s,r}) \left[k_{f,r} \prod_{s'=1}^{N_s} \left(\frac{c_{s'}}{10^6} \right)^{\nu'_{s',r}} - k_{b,r} \prod_{s'=1}^{N_s} \left(\frac{c_{s'}}{10^6} \right)^{\nu''_{s',r}} \right] \tag{2.2}$$

where M_s is the molecular weight, $\nu'_{s,r}$ and $\nu''_{s,r}$ correspond to the stoichiometric coefficients of the reactant and product for species s, respectively, for chemical reaction r, $k_{f,r}$ and $k_{b,r}$ are the forward and reverse rate coefficients for reaction r, and c_s is the concentration for species s. The unit conversion factor of 10^6 is employed to account for rate coefficient data conventionally being reported in centimeter units.

2.2.2 Mixture Momentum Conservation

The momentum of the fluid mixture is modeled and only requires a single equation. It follows primarily that of the traditional Navier-Stokes equation for compressible flows, with special care paid to the method of computing the viscosity coefficient, μ_s, contained in the viscous stress tensor, $\vec{\vec{\tau}}$. This single equation is expressed as:

$$\underbrace{\frac{\partial (\rho \vec{u})}{\partial t}}_{(1)} + \underbrace{\nabla \cdot (\rho \vec{u} \otimes \vec{u})}_{(2)} = \underbrace{-\nabla p}_{(3)} + \underbrace{\nabla \vec{\vec{\tau}}}_{(4)} \tag{2.3}$$

Terms (1) and (2) are similar to those above, except here they track the mixture

momentum unsteadiness within an element and the flux of it across element boundaries, respectively. Term (3) and (4) model the pressure and viscous forces acting on and/or along element boundaries, respectively. Here, the mixture pressure is calculated by Dalton's law of partial pressure with slight modification for the electron species:

$$p = \sum_{s \neq e}^{N_s} \rho_s R_s T_{tr} + \rho_e R_e T_V \tag{2.4}$$

The symmetric stress tensor, $\vec{\vec{\tau}}$, is expressed as follows:

$$\vec{\vec{\tau}} = \begin{bmatrix} \tau_{xx} & \tau_{xy} & \tau_{xz} \\ \tau_{yx} & \tau_{yy} & \tau_{yz} \\ \tau_{zx} & \tau_{zy} & \tau_{zz} \end{bmatrix} \tag{2.5}$$

with each component, in tensor form, expressed as

$$\tau_{ij} = \mu \left(\frac{\partial u_i}{\partial x_j} + \frac{\partial u_j}{\partial x_i} \right) + \delta_{ij} \lambda \frac{\partial u_k}{\partial x_k} \tag{2.6}$$

where δ_{ij} is the Kronecker delta, and Stokes' hypothesis is used to set $\lambda = -\frac{2}{3}\mu$. For this work, the viscosity is that of the mixture viscosity, or $\mu = \mu_m$, which is defined in section 2.4.5.

2.2.3 Vibrational-Electronic Energy Conservation

Following the work of Gnoffo et al [31], the vibrational-electronic temperature makes up the second temperature of the two-temperature model. It assumes that the vibrational and electronic modes are in a state of local thermodynamic equilibrium, thus their respective energies satisfy the equipartition principle and thus their temperatures are equal ($T_v = T_{el}$). Thus, a combined vibrational-electronic temperature, T_V, is used instead, and the tracking of the combined vibrational-electronic energy, e_V, is modeled. The transport equation for the vibrational-electronic energy is expressed as:

$$\underbrace{\frac{\partial\left(\rho e_V\right)}{\partial t}}_{(1)}+\underbrace{\nabla\cdot\left(\rho\vec{u}e_V\right)}_{(2)}=\underbrace{-p_e\nabla\cdot\vec{u}}_{(3)}+\nabla\cdot\left(\underbrace{k_V\nabla T_V}_{(4)}+\underbrace{\rho\sum_s^{N_s}h_{V,s}D_s\nabla y_s}_{(5)}\right)$$

$$+\underbrace{S_{VT}}_{(6)}+\underbrace{S_{ET}}_{(7)}+\underbrace{S_{e-ion}}_{(8)}+\underbrace{S_{prod}}_{(9)} \tag{2.7}$$

with p_e being the pressure of the free-electrons, modeled as

$$p_e = \rho_e R_e T_V \tag{2.8}$$

and

$$e_V \equiv e_v + e_e \tag{2.9}$$

$$h_{V,s} \equiv h_{v,s} \tag{2.10}$$

$$k_V \equiv k_v \tag{2.11}$$

where e_v represent the mass-averaged vibrational energy as

$$e_v \equiv \sum_s^{N_s} \frac{\rho_s e_{v,s}}{\rho}, \tag{2.12}$$

the electron energy for free-electrons is

$$e_e = \frac{3}{2}R_e T_V, \tag{2.13}$$

and the vibrational enthalpy is

$$h_{V,s} = c_{v,V} T_V \tag{2.14}$$

and k_V is the vibrational thermal conductivity coefficient, which will be examined in section 2.4.4.

With the definitions above in mind, a transport equation for the vibrational-

42

electronic energy is constructed. As before, terms (1) and (2) track the mass-averaged vibrational-electronic energy unsteadiness within an element and the flux of it across element boundaries, respectively. Term (3) monitors the work advected by the electron pressure across each element boundary. Term (4) tracks the combined conduction of energy from the vibrational and electronic modes. Term (5) tracks the diffusion of the combined enthalpies of each species across element boundaries. Term (6) accounts for the vibrational-translation relaxation process between molecules and their collisions with all other species, excluding free-electrons. Term (7) tracks the energy exchanged between electrons and heavy particles via elastic collision. Term (8) tracks the energy lost from electron impact ionization between electrons and neutral particles (only singly ionized species are being considered in this model). Term (9) tracks the production (recombination reactions) and depletion (dissociation reactions) of vibrational energy.

Source terms, such as (6) and (9), often have a variety of models that can be implemented. For example, the vibrational relaxation process can be modeled with the linearized Landau-Teller model and supplementary Millikan-White-type relaxation time data [22]. However, recent works [32] demonstrate more sophisticated modeling approaches derived from kinetic theory and show promise to be more robust in regions of large deviations from local thermodynamic equilibrium. With continually improving modeling techniques in mind, SANS has been constructed to allow for easy implementation and testing of these terms.

This work uses the linearized Landau-Teller model for vibrational relaxation with the Millikan-White relaxation time and Park's high-temperature correction models:

$$S_{VT} = \rho \left(\frac{e_{v_{s,m}}(T_{tr}) - e_{v_{s,m}}(T_V)}{\tau_{s,m}} \right) \tag{2.15}$$

where the mass-averaged vibrational energies are evaluated using the specified temperatures. It should be mentioned that the mass-averaging process naturally eliminates atomic and electron species as their vibrational energies are 0 by definition. The vibrational energy is expressed as:

$$
e_{v_{s,m}}(T) = \begin{cases} \sum\limits_{m \neq \text{atoms}}^{n_s} \dfrac{\bar{R}}{M_s} \dfrac{\Theta_{v_{s,m}}}{\exp(\Theta_{v_{s,m}}/T)-1} & \text{molecules} \\[2ex] 0 & \text{atoms} \end{cases} \tag{2.16}
$$

where the summation of the characteristic vibrational modes are used for the poly-atomic species, and the diatomic species reduces to the conventional non-summation form due to their single characteristic vibrational temperature. The vibrational re-laxation time for each mode follows the work of Freno et al [33]:

$$
\tau_{s,m} = \left(\sum_{s'=1}^{n_s} \frac{X_{s'}}{\tau_{s,m,s'}} \right)^{-1} + \left(N_A \sigma_{v_s} \sqrt{\frac{8}{\pi} \frac{\bar{R}T}{M_s}} \sum_{s'=1}^{n_s} \frac{\rho_{s'}}{M_{s'}} \right)^{-1} \tag{2.17}
$$

where the mole fraction is expressed as

$$
X_s = \frac{\rho_s/M_s}{\sum\limits_{s'=1}^{n_s} \rho_{s'}/M_{s'}} \tag{2.18}
$$

and the vibrational relaxation time is modeled by the Millikan-White expression

$$
p_{atm}\tau_{s,m,s'} = \exp\left(a_{s,m,s'}\left(T^{-1/3} - b_{s,m,s'}\right) - 18.42 \right) \tag{2.19}
$$

with p_{atm} being the pressure in units of atmospheres. Here, the parameters $a_{s,m,s'}$ and $b_{s,m,s'}$ are modeled by

$$
a_{s,m,s'} = 1.16 * 10^{-3} \mu_{s,s'}^{1/2} \Theta_{v_{s,m}}^{4/3} \tag{2.20}
$$

$$
b_{s,m,s'} = 0.015 \mu_{s,s'}^{1/4} \tag{2.21}
$$

where $\mu_{s,s'} = \frac{M_s M_{s'}}{M_s + M_{s'}}$ is the reduced mass of species s and s' in units of grams. Avagadro's number is represented as N_A, and the vibrational collision cross section σ_{v_s} is modeled as

$$
\sigma_{v_s} = \sigma'_{v_s} \left(\frac{50,000 \text{ K}}{T} \right)^2 \tag{2.22}
$$

with σ'_{v_s} the vibrational collision cross section at 50,000 K, here approximated as $\sigma'_{v_s} = 3 * 10^{-21}$ m^2.

The elastic energy exchanges between electrons and heavy particles in term (7) is modeled via the expression derived from Lee [34]:

$$S_{ET} = 3\rho_e R \left(T_{tr} - T_V\right) \sqrt{\frac{8RT_V}{\pi M_e}} \sum_{s \neq el}^{N_s} \frac{\rho_s N_A \sigma_{es}}{M_s^2} \tag{2.23}$$

The effective electron-neutral energy exchange cross-section is currently set to $\sigma_{es} = 10^{-20}$ m^2 as recommended by Candler et al [35], although curve-fits exist for these cross-section data [31]. For collisions with ionic species s, the effective energy exchange cross-section is [34]:

$$\sigma_{es} = \frac{8\pi}{27} \frac{e^4}{(kT_V)^2} \ln \left(1 + \frac{9(k_b T_V)^3}{4\pi e^6 n_e}\right) \tag{2.24}$$

where e is the charge of an electron, and k_b is the Boltzmann constant.

The impact ionization energy of term (8) is modeled by tracking the rate of ion products being formed and depleted, and their resulting addition or subtraction of energy through the ionization effects:

$$S_{e-ion} = -\sum_s^{n_{s,ion}} \dot{n}_{s,e} \hat{I}_s \tag{2.25}$$

Here, $\dot{n}_{s,e}$ is the molar rate of ionic species s being produced from electron-impact ionization reactions, and $\hat{I}_s$ is the first (molar) ionization energy of the parent neutral particle.

The production and depletion term has been modeled by:

$$S_{prod} = \sum_s^{n_{s,mol.}} \left(\dot{w}_{s,diss} \tilde{D}_s + \dot{w}_{s,rec} e_v\right) \tag{2.26}$$

where $\tilde{D}_s$ is the approximate energy lost from dissociation events and e_v is the vibrational energy gained from recombination events. Using this model, the work in this work has selected a value for $\tilde{D}_s = c\hat{D}_s$, with $c = 0.3$. Here, $\hat{D}_s$ is the required energy to dissociate a molecule s, namely its dissociation energy.

2.2.4 Total Energy Conservation

Lastly, the mass-averaged total energy of the fluid is modeled via the following transport equation:

$$\underbrace{\frac{\partial\left(\rho E\right)}{\partial t}}_{(1)} + \underbrace{\nabla\cdot\left(\rho\vec{u}E\right)}_{(2)} = \underbrace{-\nabla\cdot\left(p\vec{u}\right)}_{(3)} + \nabla\cdot\left(\underbrace{k_{tr}\nabla T_{tr}}_{(4)} + \underbrace{k_V\nabla T_V}_{(5)} + \underbrace{\rho\sum_{s}^{N_s} h_s D_s \nabla y_s}_{(6)}\right) + \underbrace{\Phi}_{(7)}.$$

$$(2.27)$$

Terms (1) and (2) monitor the rate of change of and the advection of the total energy E inside an element and across element boundaries, respectively. Term (3) represents the flow work advected across each element boundary. Terms (4) and (5) represent the conduction of transrotational energy (with k_{tr} explained in section 2.4.4) and vibrational-electronic energy, respectively. Term (6) tracks the diffusion of enthalpy across element boundaries of each species. Term (7) tracks the work done by fluid shear. Note that effects from heat transfer via radiative transport have been neglected in this model.

The total energy E is defined as the energy from translational modes, internal modes, the kinetic energy of the mixture itself, and the formation enthalpy of each species:

$$E = \sum_{s}^{N_s} \frac{\rho_s e_{tr,s}}{\rho} + e_v + e_e + \sum_{s}^{N_s} \frac{\rho_s \Delta H_{f,s}^{\circ}}{\rho} + \frac{u^2}{2} \qquad (2.28)$$

The work produced by fluid shear, Φ, is expressed wholly as:

$$\Phi = \frac{\partial}{\partial x}\left(u\tau_{xx} + v\tau_{xy} + w\tau_{xz}\right) + \frac{\partial}{\partial y}\left(u\tau_{yx} + v\tau_{yy} + w\tau_{yz}\right) + \frac{\partial}{\partial z}\left(u\tau_{zx} + v\tau_{zy} + w\tau_{zz}\right)$$

$$(2.29)$$

2.3 Chemical Kinetics Modeling

Chemical reaction rate coefficient data is also often reported in units of $[(\text{cm}^3)^{d-1} / \text{mol s}]$, where d is the reaction order for a chemical reaction r. These data are also typically given in some modified-Arrhenius form:

$$k_f(T) = A \left(\frac{T}{T_{norm}} \right)^{\beta} \exp(-E_a/T) \tag{2.30}$$

where A is a constant, T_{norm} is a normalizing temperature (this work uses $T_{norm} = 1$ K), β is a curve-fitting exponent, and E_a is the activation energy of the reaction, which may be normalized by the Boltzmann constant k_b, ideal gas constant R, or sometimes reported in temperature units directly without mention of the normalizing constant. This work will also leverage existing rates used in literature from two different kinetics models, namely Park's model [36] and the model of Marrone and Treanor [37].

The reverse rate coefficient for reaction r is computed via use of the equilibrium constant:

$$k_{b,r} = \frac{k_{f,r}}{K_{eq,r}} \tag{2.31}$$

First, the equilibrium constant in pressure units for reaction r, $K_{p,r}$, is computed with the aid of the JCZS2i Thermochemical plots produced by Miller et al [38]:

$$K_{p,r} = \exp \left\{ \left(\frac{\Delta S_r}{R} - \frac{\Delta H_r}{RT} \right) \right\} \tag{2.32}$$

where

$$\frac{\Delta H_r}{RT} = \sum_{s}^{N_s} (\nu''_{s,r} - \nu'_{s,r}) \frac{H_s}{RT} \tag{2.33}$$

$$\frac{\Delta S_r}{R} = \sum_{s}^{N_s} (\nu''_{s,r} - \nu'_{s,r}) \frac{S_s}{R} \tag{2.34}$$

Then, the transformation of the equilibrium constant from pressure units to concentration units for reaction r is accomplished via:

$$K_{eq,r} = K_{p,r} \left(\frac{p_{atm}}{RT} \right)^{\sum_s^{N_s} (\nu''_{s,r} - \nu'_{s,r})} \tag{2.35}$$

where $p_{atm} = 101,325$ Pa. Note that for reaction rate coefficients reported in centimeter units, a conversion factor of 10^6 divides the quantity (p_{atm}/RT) before the exponent $\sum_s^{N_s} (\nu''_{s,r} - \nu'_{s,r})$ is applied. Equation (2.35) is used in equation (2.31) for the calculation of the reverse rate coefficient k_b for reaction r. From here, these forward and reverse rates are substituted into equation (2.2), closing out the rate coefficient modeling framework.

2.3.1 Park's Kinetic Model

Park's preferential-dissociation [36] model relies on an activation temperature $T_a = T_{tr}^q T_v^{1-q}$ with $q = 0.5$, resulting in a geometric average between the transrotational and vibrational temperatures. Park's resulting rate coefficient curve-fits are in the form of (2.30) with $T_{norm} = 1$ K:

$$k_f(T_a) = A T_a^\beta \exp(-E_a/T_a) \tag{2.36}$$

2.3.2 Marrone-Treanor Model

The Marrone-Treanor model [37] multiplies a vibrational coupling factor with the thermal rate coefficient k_f^{th}, where k_f^{th} the typical modified-Arrhenius data found in the form of equation (2.30). This formulation is expressed as

$$k_f(T_{tr}, T_V) = Z(T_{tr}, T_V) k_f^{\text{th}}(T_{tr}) \tag{2.37}$$

where the coupling factor takes the form

$$Z(T_{tr}, T_V) = \frac{Q(T_{tr})Q(T_f)}{Q(T_V)Q(-U)} \tag{2.38}$$

with

$$Q(T_i) = \frac{1 - \exp\{(-E_a/T_i)\}}{1 - \exp\{(\Theta_v/T_i)\}} \tag{2.39}$$

where T_i takes on the values of T_{tr}, T_v, T_f, or $-U$. T_f is defined as

$$T_f = \left(\frac{1}{T_v} - \frac{1}{T_{tr}} - \frac{1}{U}\right)^{-1} \tag{2.40}$$

The parameter U is a constant with a value of $U = E_a/3$.

2.4 Transport Coefficient Modeling

2.4.1 Collision Integral Modeling

Tabulated Phenomonological Collision Integrals

Laricchiuta et al [39] have proposed the use of a Lennard-Jones like phenomenological collision integrals formulation for neutral-neutral and neutral-ion collisions for high-enthalpy fluid mechanics applications in the temperature range of $T = 10^2$ through $T = 10^5$. The approach considers only purely elastic collisions, thus ignoring inelastic effects from other processes such as resonant charge transfer in atom-parent ion collisions (e.g. N-N$^+$ and O-O$^+$). They utilize a modified phenomenological intermolecular potential function

$$\phi(r) = \epsilon_0 \left[\frac{m}{n(x) - m}\left(\frac{1}{x}\right)^{n(x)} - \frac{n(x)}{n(x) - m}\left(\frac{1}{x}\right)^{m}\right] \tag{2.41}$$

with $x = r/r_e$ and the other parameters and full formulation described in [39]. The potential is clearly Lennard-Jones like in form, and the varying of the parameters dictates the modeling of neutral-neutral and neutral-ion collisions.

The model results are tabulated in terms of an empirical parameter $\beta_{s,s'}$, which depends on the polarazabilities of the interacting molecules, α_s and $\alpha_{s'}$, and $T^* = kT/\epsilon_0$. Here, ϵ_0 is a parameter that depends on the equilibrium radius, r_e, and polarizabilities as well as an effective long-range London coefficient for neutrals. For ions, there is an additional parameter that accounts for the roles of dispersion and

induction attraction components that affect the equilibrium distance. Further details can be found in [39]. The resulting tabulated expressions are of the form

$$\ln \Omega_{s,s'}^{(i,j)*} = [a_1(\beta_{s,s'}) + a_2(\beta_{s,s'})x^*] \frac{\exp\{[(x - a_3(\beta_{s,s'}))/a_4(\beta_{s,s'})]\}}{\exp\{[(x - a_3(\beta_{s,s'}))/a_4(\beta_{s,s'})]\} + \exp\{[(a_3(\beta_{s,s'}) - x)/a_4(\beta_{s,s'})]\}}$$
$$+ a_5(\beta_{s,s'}) \frac{\exp\{[(x - a_6(\beta_{s,s'}))/a_7(\beta_{s,s'})]\}}{\exp\{[(x - a_6(\beta_{s,s'}))/a_7(\beta_{s,s'})]\} + \exp\{[(a_6(\beta_{s,s'}) - x)/a_7(\beta_{s,s'})]\}}$$

$$(2.42)$$

where $x = \ln T^*$ and the coefficients a_i are found via a tabulated polynomial fit of the form

$$a_i(\beta_{s,s'}) = \sum_j^2 c_j \beta_{s,s'}^j \tag{2.43}$$

In order to recover the actual (non-reduced) collision integrals, the collision cross-sections are found via the relation

$$\sigma^2 = (x_0 r_e)^2 \tag{2.44}$$

where x_0 is described by the tabulated power function in [39]

$$x_0(\beta_{s,s'}) = \xi_1 \beta_{s,s'}^{\xi_2} \tag{2.45}$$

Screened Coulomb Potential Collision Integrals

For ion-ion, ion-electron, and electron-electron interactions, the collision integrals are modeled using a screened coulomb potential. Stallcop et al [40] tabulated their results and they are given in the form

$$\sigma^2 \Omega_{s,s'}^{(N,N)*} = 5 \times 10^{15} \left(\frac{\lambda}{T^*}\right) \ln\left[D_N T^*(1 - C_N \exp\{(-c_N T^*)\}) + 1\right] \tag{2.46}$$

of which the curve-fit values D_N, C_N, and c_N can be found in [41]. The Debye

shielding length λ and the reduced temperature T^* for these interactions can also be found in [41].

Post-Processing Collision Integral Data for Use in SANS

A final curve-fit of the neutral-neutral collision integrals is performed to help minimize the computational cost of computing collision integral values and their derivatives. While the neutral-neutral tabulation is of an analytical form, computing the numerous exponentials (and thus their derivatives) is a computationally expensive set of operations.

In order to reduce this computational cost, an exponential curve-fit of the form used by Gupta et. al. [42] is fit to the output of the neutral-neutral tabulated model data. The curve-fit is of the following form:

$$\sigma^2 \Omega_{s,s}^{(i,i)*} = \exp\left(C\right) T^{(A \ln(T)+B)} \tag{2.47}$$

Minimizing the number of exponential functions to compute over the course of a simulation provides a slight speed improvement with negligible loss of accuracy.

With the collision integrals calculated, the pure-gas viscosities and thermal conductivites can be computed from kinetic theory for use with the mixing rules, which are discussed in section 2.4.5.

2.4.2 Diffusion Coefficients

This work models the effective mixture diffusion coefficient D_s via a constant Lewis number approach for simplicity. A Lewis number value of 1.4 is used for neutral species and a Lewis number of 2.8 is used for ionized species. The computation of the diffusion mass flux follows the approximation to multi-component diffusion as discussed by Sutton and Gnoffo [43]. Fick's law is used in conjunction with the mixture diffusion coefficient:

$$\vec{J}_s = -\rho D_s \nabla y_s \tag{2.48}$$

and is corrected via:

$$\vec{J}_{s,corrected} = \vec{J}_s - y_s \sum_{i}^{N_s} \vec{J}_i \qquad (2.49)$$

The corrected form of the diffusion mass flux is then substituted into equations (2.1), (2.7), and (2.27), where appropriate.

2.4.3 Viscosity Coefficients

In order to calculate the mixture viscosity with the use of a mixing rule, only the pure-gas viscosity coefficients must be calculated for each species. From kinetic theory, the viscosity coefficient, μ_s, for a pure, neutral gas is

$$\mu_s = \frac{5}{16}\sqrt{\frac{k}{\pi N_A}} \frac{\sqrt{M_s T_{tr}}}{10^{-20}\sigma^2\Omega_{ss}^{(2,2)*}} \qquad (2.50)$$

where 10^{-20} is used to convert from square Angstroms to square meters.

Typically, the viscosity for an ionized gas species is of a different form, which can be found in Spitzer [44]. However, with the shielded-Coulomb potential collision integral curve-fits produced by Stallcop et al [40], they show that equation (2.50) can be used for the computation of the viscosity coefficients of pure ionized gas species as well.

2.4.4 Thermal Conductivity Coefficients

The mixture thermal conductivity coefficients also are computed via the use of a mixing rule, which also relies on the species thermal conductivity coefficients as a result. The separate translational and internal (rotational and vibrational) modes are calculated for each species in the multi-temperature model based on molecular-kinetic theory as follows:

$$k_{t,s} = \frac{5}{2}\mu_s c_{v,t,s} \qquad (2.51)$$

$$k_{r,s} = \frac{6}{5}\frac{\Omega_{ss}^{(2,2)^*}}{\Omega_{ss}^{(1,1)^*}}\mu_s c_{v,r,s} \tag{2.52}$$

$$k_{V,s} = \frac{6}{5}\frac{\Omega_{ss}^{(2,2)^*}}{\Omega_{ss}^{(1,1)^*}}\mu_s c_{v,V,s} \tag{2.53}$$

The combined transrotational modes are modeled simply as the summation of the translation and rotational modes:

$$k_{tr,s} = \mu_s \left[\frac{5}{2}c_{v,t,s} + \frac{6}{5}\frac{\Omega_{ss}^{(2,2)^*}}{\Omega_{ss}^{(1,1)^*}}c_{v,r,s} \right] \tag{2.54}$$

2.4.5 Mixing Rules

The calculation of mixture transport properties of multi-component gases can be derived from rigorous kinetic theory arguments (a derivation can be found in Hirschfelder [45], as well as many other kinetic theory textbooks). Ultimately, the solution of the following ratio of determinants must be carried out in order to compute a full multi-component gas mixture transport property, μ_m:

$$\mu_m = -\frac{\begin{vmatrix} \mathbf{H} & \mathbf{X} \\ \mathbf{X}^T & 0 \end{vmatrix}}{|\mathbf{H}|} \tag{2.55}$$

where the elements of $\mathbf{H}$, H_{ij}, as shown by Palmer and Wright, are [41]

$$H_{ij} = B\frac{X_i}{\sqrt{T}}\sum_{k=1}^{n_s}\frac{X_k\sqrt{\mu_{ik}}}{(m_i+m_k)}\sigma^2\Omega_{ik}^{(2,2)^*}\left[\frac{5}{3}\frac{\sigma^2\Omega_{ik}^{(1,1)^*}}{\sigma^2\Omega_{ik}^{(2,2)^*}}(\delta_{ij}-\delta_{jk}) + \frac{m_k}{m_j}(\delta_{ij}+\delta_{jk})\right] \tag{2.56}$$

with the constant B (in cgs units) expressed as

$$B = \left(6.4\times10^{-16}\right)\sqrt{\frac{\pi N_A}{2k_b}}, \tag{2.57}$$

and the mole fraction vector, $\mathbf{X}$,

$$\mathbf{X} = \begin{bmatrix} X_1 & X_2 & ... & X_n \end{bmatrix}^T.$$ (2.58)

The calculation of equation (2.55) and its derivatives must be carried out for each element. As it is currently written, this calculation becomes more expensive as the number of species increases. The calculation of the mixture transport coefficients can be reduced instead by using a mixing rule to approximate the solution to the full determinant calculation.

There are several mixing rules that are traditionally used, and two of them will be examined below. First, Wilke's mixing rule will be briefly reviewed, as it is a commonly used mixing rule. Then, the Armaly-Sutton 0.2 mixing rule with be shown written in a form congruent to that of Wilke's mixing rule, which gives similar levels of computational performance with increased accuracy for weakly-ionized plasma flows [41].

Wilke's Mixing Rule

Wilke's mixing rule is expressed in the modular form as shown in equations (2.59) and (2.63). The mixture transport coefficient is computed by a product of the species s mole fraction and its pure-gas transport coefficient, μ_s, and then divided by Wilke's scaling factor expressed by ϕ_s.

$$\mu_m = \sum_s^{N_s} \frac{X_s \mu_s}{\phi_s}$$ (2.59)

A few definitions of collision integral ratios are seen in the derivations of this rule and are defined here for convenience. First, the ratio of viscosity and momentum transfer collision integrals is expressed as

$$A_{s,s'}^* = \frac{\Omega_{s,s'}^{(2,2)*}}{\Omega_{s,s'}^{(1,1)*}}$$ (2.60)

Next, the ratio of the viscosity collision integrals with their pure-gas counterparts are defined as

$$B_{s,s'} = \frac{\Omega^{(2,2)*}_{s,s'}}{\Omega^{(2,2)*}_{s',s'}} \tag{2.61}$$

$$F_{s,s'} = \frac{\Omega^{(2,2)*}_{s,s'}}{\Omega^{(2,2)*}_{s,s}} \tag{2.62}$$

Several assumptions have been made about the collision integrals ratios $A^*_{s,s'}$, $B_{s,s'}$, and $F_{s,s'}$. First, Wilke assumed that $A^*_{s,s'} = 5/3$ for all interactions. $B_{s,s'}$ and $F_{s,s'}$ are both assumed to be 1. These assumptions result in the scaling factor ϕ_s being expressed as

$$\phi_s = \sum_{s'}^{N_s} X_s \left[1 + \sqrt{\frac{\mu_s}{\mu_{s'}}} \left(\frac{M_{s'}}{M_s}\right)^{1/4}\right]^2 \bigg/ \left[8\left(1 + \frac{M_s}{M_{s'}}\right)\right]^{1/2} \tag{2.63}$$

Armaly-Sutton 0.2 Mixing Rule

The Armaly and Sutton mixing rule also makes use of equation (2.59) and has its scale factor expressed as (2.64), as found in [41]. In this mixing rule, the assumptions for the collision integral ratios $A^*_{s,s'}$ and $B_{s,s'}$ are all dependent upon the interaction type, while $F_{s,s'}$ remains equal to 1.

All interactions have $A^*_{s,s'} = 1.25$, except for those of an atom with its own ion. For air species, namely N-N$^+$ and O-O$^+$ collisions, the Armaly-Sutton 0.2 Mixing Rule sets $A^*_{s,s'} = 0.21$ (thus the 0.2). $B_{s,s'}$ has more specificity in its value for interaction types. For neutral-neutral pairs, it is set to 0.78. For neutral-ion interactions, it is set to 0.15. For neutral-electron interactions, it is set to 0.2. Finally, for ion-ion, ion-electron, and electron-electron interactions, it is set to 1.0. There are some mathematical inconsistencies that arise as $B_{s,s'} = F_{s,s'}$; however, these parameters are best-fit parameters, as explained in [41]. With these parameters defined, the scaling factor is expressed as:

$$\phi_s = X_s + \sum_{s' \neq s}^{N_s} \left\{ X_{s'} \left[\frac{5}{3} \frac{1}{A^*_{s,s'}} + \frac{M_{s'}}{M_s} \right] \bigg/ \left[1 + \frac{M_{s'}}{M_s} \right] \times \right.$$

$$\left. \left[F_{s,s'} + B_{s,s'} \sqrt{\frac{\mu_s}{\mu_{s'}}} \left(\frac{M_{s'}}{M_s} \right)^{1/4} \right]^2 \bigg/ \left[8 \left(1 + \frac{M_s}{M_{s'}} \right) \right]^{1/2} \right\} \qquad (2.64)$$

2.4.6 Verification of Procedure

The verification of the transport coefficient procedure is done in comparison with work by Gupta et al [42]. Gupta et al have given their curve-fit parameters for their collision integral data as well as other transport coefficients. All data for generating the collision integrals according to the procedure outlined in this chapter, as well as their curve-fit information, may be found in appendix D.
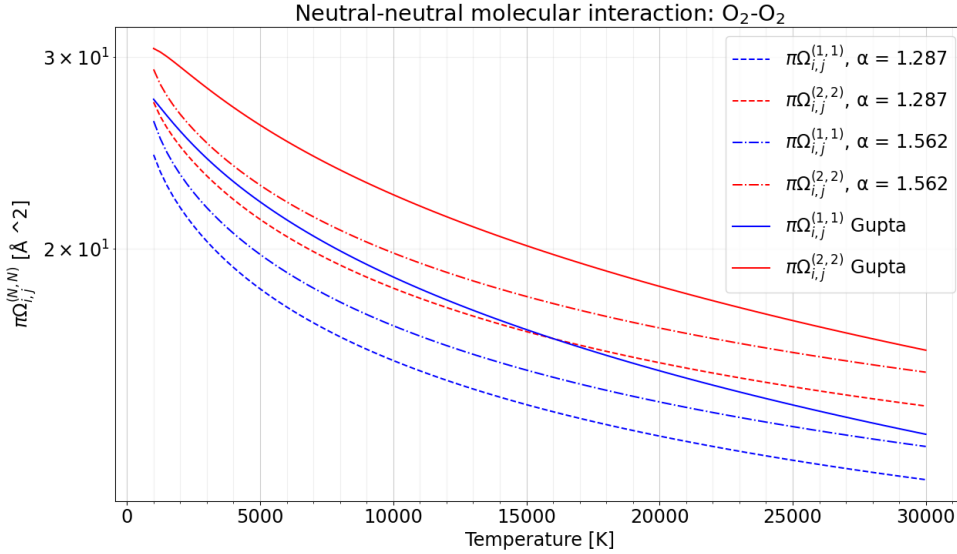
Figure 2-1: Collision integral comparison for O_2-O_2 collision using a polarizability value of $\alpha = 1.287$ as calculated at the *MP2/6-311+G(3df)* level of theory in this work, $\alpha = 1.562$ as seen in experimental data from Olney et al [46], and from the curve-fits of Gupta et al [42].

A comparison of the Armaly-Sutton mixing rule implemented in this work with

the data of Murphy et al [47] and Murphy [48], shown in Figure 2-2, demonstrates that this mixing rule approach provides a reasonable estimate to mixture transport properties. Palmer and Write [41] also demonstrated that this approach can provide these estimates at a reduced computational cost.
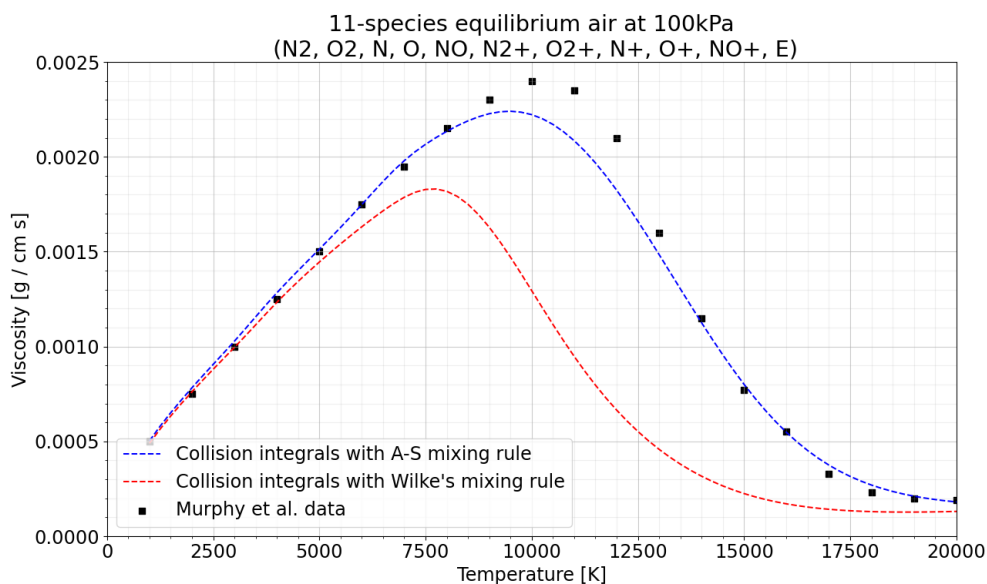
Figure 2-2: Both Wilke's and Armaly-Sutton mixing rules employed for 11-species equilibrium air at 100 kPa using the *MP2/6-311+G(3df)* level of theory for the required polarizability values pure gas viscosity computations.

Chapter 3

Ab-initio Chemical Kinetics Modeling for Low-Temperature air-SF$_6$ Plasma Interfacial Species

3.1   Identification of O, N, F, and S Compounds

In order to generate a chemical model, one must know which chemical species to model. For this work, examination of 89 species previously identified in sulfur hexafluoride and air plasmas was carried over a temperature range from 300K to 6000K for various initial concentrations of air and SF_6. The equilibrium concentrations were calculated for this parameter space and a species concentration cut-off criterion was employed to down-select to a computationally tractable amount of species. It was then cross-checked with the available literature of chemical reactions involving sulfur-fluoride compounds with oxygen and nitrogen species at the temperatures and pressures that are typically encountered by hypersonic vehicles.

With the identification of these compounds, a simple set of chemical reactions were hypothesized that successfully traces chemical pathways from an initial 11-species air and SF_6 mixture to the final set of identified products. These reactions were then modeled via Transition State Theory (TST), Nonadiabatic Statistical Theory

(NAST), and other simplified methods utilizing first-principles. For this work, reactions involving electrons were not explored for the "interfacial" species reactions. Select model reactions from this work will be used to aid in explaining the aforementioned models, with the results for the remaining reactions documented in Appendix B.

3.2   Canonical Transition State Theory (CTST)

From the work of Eyring, Vigner, and Polanyi and Evans, canonical (also "classical" or "conventional") transition state theory (CTST) provides a useful framework to estimate the upper bounds for electronically (i.e. spin) adiabatic chemical reaction rates. Nonadiabatic chemical reactions (which involve multiple potential energy surfaces) are generally not suitable for CTST, and instead will be the topic of the section 3.4. Several assumptions are made in the formulation of CTST:

1. Electronic and nuclear motions of atoms/molecules are separate (Born-Oppenheimer assumption)

2. Reactants and products are equilibriated/thermalized among their states (Boltzmann distributed)

3. Reactants go to products or products go to reactants, does not reverse direction midway through (no recrossing events over the reactant-product dividing surface)

4. Energy modes of TS are separable, allowing for the reaction coordinate to be treated classically as a translation (partition functions are separable)

There exists extensions to CTST that improve upon these assumptions, such as canonical variational transition state theory (CVT). In CVT, one now relaxes the third assumption and allows for recrossing events to occur. The variational approach allows for the position of the dividing surface between reactants and products to be variationally optimized such that the number of recrossing events is min-

60

imized. In more practical terms, the position of the dividing surface is optimized such that the predicted rate coefficient is minimized (CTST generally provides an upper-bound/overestimate of the rate coefficient):

$$\frac{dk_{CVT}(T)}{dq^{\ddagger}} = 0 \tag{3.1}$$

where $q^{\ddagger}$ is the reaction coordinate at the dividing surface location. A more comprehensive review of CVT and other extensions to variational transition state theory can be seen in Bao and Truhlar [49]. For this work, only CTST is used.

The rate coefficient derived from CTST for a bimolecular reaction

$$A + B \longrightarrow X^{\ddagger} \longrightarrow \text{products} \tag{3.2}$$

with reactants A and B that proceeds through a transition state $X^{\ddagger}$ to some products is expressed as:

$$k_{CTST} = \frac{k_b T}{h} \frac{Q^{\ddagger}}{Q^A Q^B} e^{-E_0/k_b T} \tag{3.3}$$

or in terms of the Gibbs standard free energy using the van t'Hoff relation:

$$k_{CTST} = \frac{k_b T}{h} e^{-\Delta G_0^{\ddagger}/RT} \tag{3.4}$$

This idealized PES contains distinct energy wells for the reactants and products and a multi-dimensional saddle point where the transition state exists. At these locations, distinct reactant, product, and transition state geometries exist. Finding these geometries and their associated properties requires the solution of an electronic structure (wave function) optimization problem. These optimizations target the minimum of the energy wells for the reactants and products, and the saddle point for the transition state. The computational results are associated geometric, statistical, and thermodynamic information pertaining to the complexes being examined.

Using the thermodynamic information from the compounds in the reaction, one can estimate the chemical reaction rate by using equation (3.4) as the reaction pro-

ceeds from reactants to products along the reaction coordinate. A range of temperatures can be selected, providing rate estimates for each of the temperatures, and a resulting modified-Arrhenius curve-fit can be applied to generate a more traditionally reported rate estimate.

As previously mentioned, CTST is be utilized to provide suitable (upper-bound) estimates for the spin-adiabatic reactions for this work. For spin-diabatic reactions, a non-adiabatic approach is required to handle the transition from one PES to another. Also, electronic structure calculations now have to optimize to a different target, namely a minimum energy crossing point (MECP) between the two PES's.

Quantum Tunneling Corrections - Eckart Potential

Chemical reactions proceeding along a reaction path with a transition state have a chance to tunnel across the potential energy barrier that separates the reactants from the products. This is particularly important at lower reactant population energies where small fractions of the reactants have sufficient energy to overcome the energy barrier to form products. A commonly used correction factor to model the quantum tunneling effects is derived from the analysis of Eckart [50] using a 1D potential. With this 1D potential model, the probability of such a tunneling event occuring at some energy state E is

$$\kappa(E) = 1 - \frac{\cosh 2\pi(a - b) + \cosh 2\pi d}{\cosh 2\pi(a + b) + \cosh 2\pi d} \tag{3.5}$$

where the derivation of the values for a, b, and d can be found in Eckart [50]. The 1D Eckart potential and its parameters are visualized in the figure below, taken from Johnston and Heicklen [51].
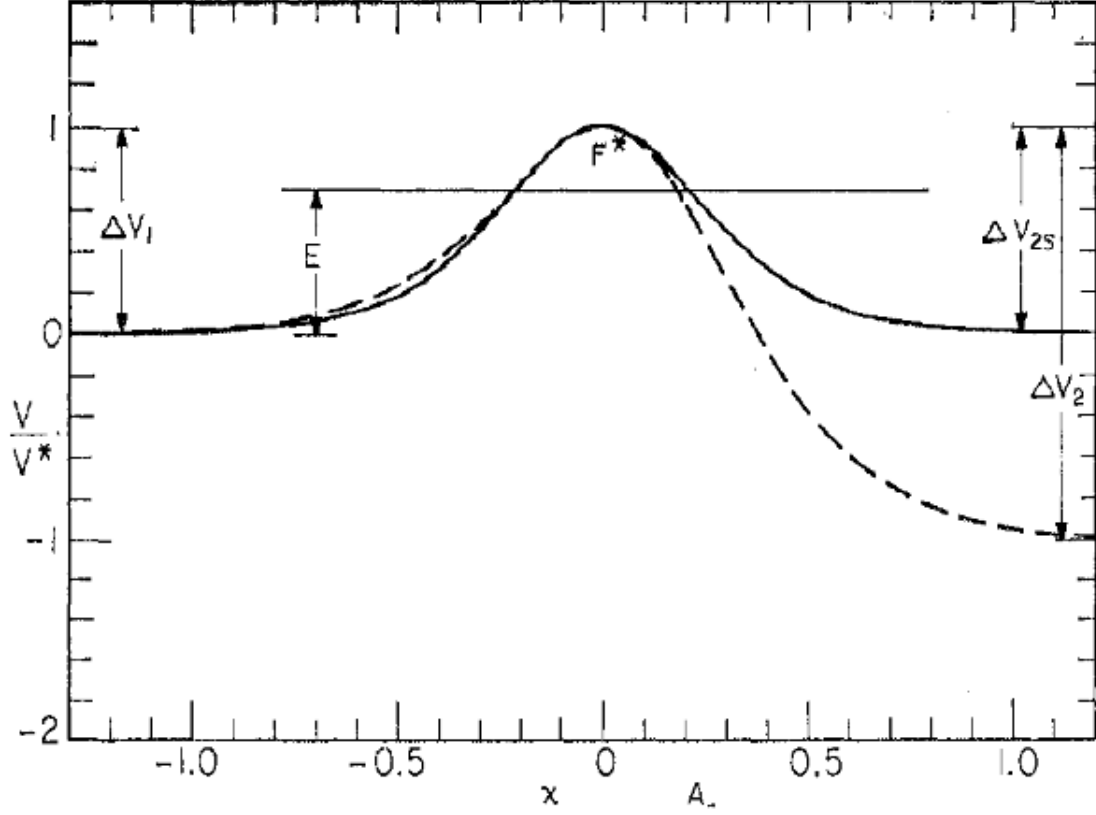
Figure 3-1: Symmetric vs Asymmetric Eckart Potential Function [51].

Utilizing the Laplace transform of equation (3.5) provides the thermalized tunneling factor correction as a function of temperature:

$$\kappa(T) = e^{\Delta V_1/k_b T} \int_0^\infty \kappa(E) e^{-(E/k_b T)} d(E/k_b T) \qquad (3.6)$$

which can then be multiplied into the rate found via equation (3.4) at the various temperatures. This tunneling effect is often of the order of 1% or less at temperatures well above $1,000$ K, where hypersonic vehicles generally operate, but due to the inexpensiveness of the correction calculation, it is carried out to verify the small effects that should be observed from tunneling events. The final rate coefficient is then found by simply multiplying together equations (3.4) and (3.6).

$$k_{CTST,corr}(T) = k_{CTST}(T)\kappa(T) \qquad (3.7)$$

63

Typically, the tunneling corrections are important at lower temperatures as the population (Boltzmann) average energy resides below the energy barrier produced by the transition state. At higher temperatures, where the average energy of the population largely resides above this barrier, tunneling becomes insignificant as the majority of reactants can proceed over the barrier to form products. In this work, the tunneling corrections are found to be negligible ($\kappa(T) \leq \mathcal{O}(10^{-3})$).

3.3 Phenomenological Pressure-Dependent Rate Coefficients

Chemical reactions containing unimolecular species, such as

$$A + B \rightleftharpoons C \tag{3.8}$$

have rate coefficients that may depend on the current pressure of the thermodynamic system. Often, these reactions require collision partners for thermal activation or deactivation so that a chemical reaction may proceed or stop, respectively. If more collision partners are available, more energy can be exchanged, increasing the rates of activation and deactivation events. If less collision partners are available, the activated unimolecular complex may go on to form different products or isomerize into a different compound if it contains enough energy in its activated state. Clearly, the amount of collision partners available influences the rates of chemical reactions and the resulting product populations. The amount of available collision partners is directly related to the pressure of the thermodynamic system being examined, and so some form of pressure dependence is expected for these types of reactions.

In order to estimate the effects of pressure on the rate coefficients, the procedure developed by Allen, Goldsmith, and Green [52] will be used in this work. They have developed an accurate and efficient procedure to utilize high-pressure limit rate coefficient data to estimate phenomenological rate coefficients $k(T, P)$ as a function of temperature T and pressure P for unimolecular isomers in a chemical network.

A brief overview of said procedure will be outlined here, while further details are discussed in their publication.

The procedure utilizes a chemical master equation which tracks both the change in the population $p_i(E,t)$ of the unimolecular isomer i over energy E for some time t, as well as the changes in concentrations $y_{nA}(t)$ and $y_{nB}(t)$ for reactants A and B that are in some nth reactant configuration. With this information, and several assumptions discussed in their paper, the master equation is written as

$$
\begin{aligned}
\frac{d}{dt}p_i(E,t) = \ & \omega_i(T,P)\int_0^\infty P_i(E,E',T)p_i(E',t)dE' - \omega_i(T,P)p_i(E,t) \\
& + \sum_{j\neq i}^{N_i} k_{ij}(E)p_j(E,t) - \sum_{j\neq i}^{N_i} k_{ji}(E)p_i(E,t) \\
& + \sum_{n=1}^{N_r} y_{nA}(t)y_{nB}(t)f_{in}(E)b_n(E,T) - \sum_{n=1}^{N_r+N_p} g_{ni}(E)p_i(E,t)
\end{aligned}
\tag{3.9}
$$

$$
\begin{aligned}
\frac{d}{dt}y_{nA}(t) = \ & \frac{d}{dt}y_{nB}(t) \\
= \ & \sum_{i=1}^{N_i}\int_0^\infty g_{ni}(E)p_i(E,t)dE - \sum_{i=1}^{N_i} y_{nA}(t)y_{nB}(t)\int_0^\infty f_{in}(E)b_n(E,T)dE
\end{aligned}
$$
$$\tag{3.10}$$

where N_i, N_r, and N_p are the number of isomers, reactants, and products, respectively; $\omega_i(T,P)$ is the collision frequency; $P(E,E',T)$ is the probability of collisional transfer from energy E' to E; $k_{ij}(E)$ is the rate coefficient for isomerization; $f_{in}(E)$ is the rate coefficient for association; $g_{ni}(E)$ is the rate coefficient for dissociation; $b_n(E,T)$ is the Boltzmann distribution for bimolecular reactant channel n. In order to discretize the master equation, the energy E can be discretized into N_g energy grains, which converts the linear integro-differential equation into a system of first-order ordinary differential equations. This discretization results in a convenient matrix equation:

$$
\frac{d}{dt}\mathbf{P} = \mathbf{MP}
\tag{3.11}
$$

In order to compute the phenomological rate coefficients $k(T, P)$ using equation (3.11), the population vector $\mathbf{p}_i$ can be expressed as a linear combination of the total populations of the unimolecular isomers and bimolecular reactants, $x_j(t)$ and $y_{mA}(t)y_{mB}$, respectively:

$$\mathbf{p}_i = \sum_{j=1}^{N_i} x_j(t)\mathbf{u}_{ij} + \sum_{m=1}^{N_r} y_{mA}(t)y_{mB}\mathbf{v}_{im} \tag{3.12}$$

where $\mathbf{u}_{ij}$ and $\mathbf{v}_{im}$ represent the population distribution of energy states of unimolecular isomer i that tracks the population of unimolecular isomer j and bimolecular reactant channel m, respectively. Here, the reactant processes are assumed to be pseudo-first order (i.e. $y_{mA} \ll y_{mB}$). Further details of this approximation can once again be seen in Allen et al [52].

For this work, the Modified Strong Collision (MCS) method, as described by Change et al [53], is used. This model allows for the decoupling of energy grains by treating the collisional stabilization of a reactive isomer as a single step process, while ignoring effects from collisional energy redistribution processes. A collision efficient factor $\beta_i(T)$ is used to modify the collision frequency $\omega_i(T, P)$ as an attempt to correct for these effects. These approximations produce an energy-grained master equation of the form:

$$\frac{d}{dt}\mathbf{p}(E, t) = \mathbf{L}(E)\mathbf{p}(E, t) + \sum_{i=1}^{N_i} x_i(t)\mathbf{z}_i(E) + \sum_{n=1}^{N_r} y_{nA}(t)y_{nB}\mathbf{w}_n(E) \tag{3.13}$$

where $\mathbf{L}(E)$ takes the form

$$\mathbf{L}(E) = \begin{bmatrix} m_1(E) & k_{12}(E) & \cdots \\ k_{21}(E) & m_2(E) & \cdots \\ \vdots & \vdots & \ddots \end{bmatrix} \tag{3.14}$$

$\mathbf{z}_i(E)$ takes the form

$$\mathbf{z}_i(E) = \begin{bmatrix} \omega_i(T,P)\beta_i(T)b_i(E;T)\delta_{i1} \\ \omega_i(T,P)\beta_i(T)b_i(E;T)\delta_{i2} \\ \vdots \end{bmatrix} \tag{3.15}$$

and $\mathbf{w}_n(E)$ takes the form

$$\mathbf{w}_n(E) = \begin{bmatrix} f_{1n}(E)b_n(E;T) \\ f_{2n}(E)b_n(E;T) \\ \vdots \end{bmatrix} \tag{3.16}$$

and the quantity $m_i(E)$, the total rate of loss of isomer i, is expressed as

$$m_i(E) = -\omega_i(T,P)\beta_i(T) - \sum_{j\neq i}^{N_i} k_{ji}(E) - \sum_{n=1}^{N_r+N_p} g_{ni}(E) \tag{3.17}$$

From here, a pseudo-steady state approximation is made to solve the system of equations represented by equation (3.13). Upon solving these equations, the resulting populations can be used to compute the desired $k(T,P)$ values:

$$k_{ij}(T,P) = \omega_i(T,P)\beta_i(T) \sum_{r=r_{0,i}}^{N_g} p_i^{(j)}(E_r) \tag{3.18}$$

$$k_{nj}(T,P) = \sum_{i=1}^{N_i} \sum_{r=r_{0,i}}^{N_g} g_{ni}(E_r)p_i^{(j)}(E_r) \tag{3.19}$$

$$k_{im}(T,P) = \omega_i(T,P)\beta_i(T) \sum_{r=r_{0,i}}^{N_g} p_i^{(m)}(E_r) \tag{3.20}$$

$$k_{nm}(T,P) = \sum_{j=1}^{N_i} \sum_{r=r_{0,i}}^{N_g} g_{nj}(E_r)p_j^{(m)}(E_r) \tag{3.21}$$

Here, the indices i and j correspond to unimolecular isomers, m to bimolecular reactants, n to bimolecular reactants and products, and r to the energy grain being examined. Matching of indices clearly indicates which reactions are being studied. Depending on the chemical network being studied, some reaction paths may return a

rate of 0, for example if no isomerization pathway exists between two isomers i and j.

Finally, the population distribution vector components for the MSC method are

$$u_{ij}(E_r) = \begin{cases} b_i(E_r)\delta_{ij} & E_r < E_{j,crit} \\ p_i^{(j)}(E_r) & E_r \geq E_{j,crit} \end{cases} \tag{3.22}$$

$$v_{im}(E_r) = \begin{cases} 0 & E_r < E_{m,crit} \\ p_i^{(m)}(E_r) & E_r \geq E_{m,crit} \end{cases} \tag{3.23}$$

The critical energy E_{crit} is determined from the lowest energy grain value where the microcanonical rate coefficient $k(E)$ is non-zero. This energy divides the low-energy population that is assumed as Boltzmann distributed from the high-energy reactive population.

How other things, such as the density of states, are estimated for the procedure outlined above, one should refer to Allen et al [52] as mentioned previously. The only information required for the estimation of pressure-dependent rates using this procedure are the high-pressure rate coefficients and the thermodynamic information for the reactions being studied.

3.3.1 Calculation of Low-Pressure Rate Constant $k_0(T)$

The Lindemann mechanism first postulated by Lindemann [54] pertains to the pressure-dependent reactions of unimolecular compounds for the general reactions

$$A + B \underset{k_{-1}}{\overset{k_1}{\rightleftharpoons}} AB^* \tag{3.24}$$

$$AB^* + M \overset{k_2}{\rightarrow} AB + M \tag{3.25}$$
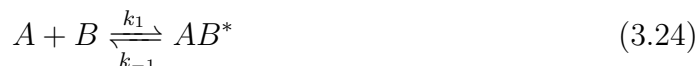
where the overall rate of formation of the excited complex AB^* is

$$\frac{d[AB^*]}{dt} = k_1[A][B] - k_{-1}[AB^*] - k_2[AB^*][M] \tag{3.26}$$

Using the steady-state approximation such that $\frac{d[AB^*]}{dt} = 0$ and solving for $[AB^*]$

$$[AB^*] = \frac{k_1[A][B]}{k_{-1} + k_2[M]} \tag{3.27}$$

The rate of formation of the deactivated AB is then

$$\frac{d[AB]}{dt} = k_2[AB^*][M] = \frac{k_1 k_2[A][B][M]}{k_{-1} + k_2[M]} = k_{eff}[A][B] \tag{3.28}$$

In the low-pressure limit, where $[M] \to 0$, the effective rate coefficient k_{eff} is

$$\lim_{[M] \to 0} k_{eff} = \frac{k_1 k_2}{k_{-1}}[M] \equiv k_0[M] \tag{3.29}$$

where k_0 is the low-pressure limit rate coefficient. The same linear dependence on $[M]$ is obtained in the limiting result when performing the low-pressure limit analysis for the general reaction

$$AB + M \longrightarrow A + B + M \tag{3.30}$$

which proceeds in the opposite direction from before.

With the master equation analysis producing phenomenological rate coefficients $k(T, P)$, one can extract the appropriate $k_0(T)$. Under the assumption of an ideal gas, the concentration $[M]$ is expressed as

$$[M] = \frac{P}{\bar{R}T} \tag{3.31}$$

where P is the pressure, $\bar{R}$ is the ideal gas constant, and T is the temperature. Upon substitution into the phenomenological rate coefficient, one gets

$$k_0(T) = k(T, P)\frac{\bar{R}T}{P} \tag{3.32}$$

With the pressure dependent analysis carried out via the energy grained master equa-

tion, and with $k(T, P)$ showing a linear dependence on the pressure in accordance with the limit in equation (3.29), the low-pressure rate coefficient $k_0(T)$ can be solved for and curve-fit to a modified-Arrhenius format, thus providing a correct estimate to the low-pressure rate coefficient.

3.4 Nonadiabatic Statistical Theory (NAST) and Minimum Energy Crossing Points (MECP's)

Transition state theory holds for reactions that occur on the same PES, specifically the PES where the reactants, transition state, and products have the same electron spin multiplicity, and are thus spin-adiabatic reactions. However, spin-nonadiabatic reactions, such as

$$SO_2F_2 \ (m = 1) \longrightarrow SO_2F_2 \ (m = 3) \tag{3.33}$$
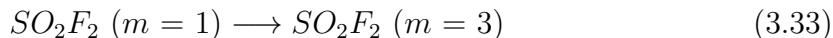
where m is the spin multiplicity, need extra care as the reaction occurs over multiple PES's. This type of reaction requires a non-adiabatic transition state theory (NA-TST), which accounts for the transition across the seam between the two PES's.

An overview of the NAST code [29, 30, 55] will be given in this section; however, for the code, full description of the code, and the theory behind the code, the reader is referred to the user manual, which may be found at: https://github.com/svarganov/NAST.

There are three foundational concepts utilized in the calculation of the MECP rate coefficients: the microcanonical rate coefficient, the microcanonical interstate crossing (ISC) probabilities, and the canonical rate coefficient. The microcanonical rate coefficient may be expressed as

$$k(E) = \sigma \frac{N_X(E)}{h\rho_R(E)} \tag{3.34}$$

where σ is the reaction path degeneracy, defined as

$$\sigma = \frac{\sigma_R}{\sigma_X}\gamma_X \tag{3.35}$$

with σ_R and σ_X being the symmetry numbers of the reactant and MECP, respectively, and γ_X being the optical isomers of the MECP. $N_X(E)$ is the effective number of states at the MECP

$$N_X(E) = \int_0^E \rho_X(E - \epsilon')P(\epsilon')d\epsilon' \tag{3.36}$$

where ρ_R and ρ_X are the density of states for the reactants and MECP, respectively, and $P(\epsilon')$ is the interstate crossing transition probability. Lastly, h is Planck's constant. The density of states for the rotational and vibrational modes are obtained via the rigid rotor and simple harmonic oscillator approximations. The rotational density of states is calculated by using the classical asymmetric top model:

$$\rho_{rot}(E_{rot}) = \frac{4\sqrt{2E_{rot}}}{\hbar^3}\sqrt{I_A I_B I_C} \tag{3.37}$$

and the rovibrational density of states are calculated via the convolution of the rotational and vibrational density of states:

$$\rho(E) = \int_0^E \rho_{vib}(E - E_{rot})\rho_{rot}(E_{rot})dE_{rot} \tag{3.38}$$

The only remaining expression to be expression to be evaluated is the probability of transition, $P(\epsilon')$, in equation (3.36). There are several models implemented in NAST, two of which are the Landau-Zener (LZ) model and the Weak Coupling (WC) model. These probability models are explained in the NAST user manual; however, some important quantities are required for the successful computation of the probabilities, and they are related to the MECP geometry, thermodynamics, and PES information.

The first key quantity that must be known is the electron spin-orbit coupling constant, denoted as H_{SO}. In simple terms, this constant quantifies the coupling effects of electron spin angular momentum and orbital angular momentum on the energy levels

between the electronic spin states of the MECP. In this work, H_{SO} is computed via the Breit-Pauli Hamiltonian [56] within the GAMESS quantum chemistry package. This work also focuses on a singlet-triplet crossing reaction; however, for higher spin state crossings, some sublties arise in the approximation of an effective H_{SO}. These cases and how to handle them are discussed in the NAST user manual.

The next key quantities are the gradients of the PES's, $\vec{g}_1$ and $\vec{g}_2$, that are parallel to the reaction coordinate at the MECP location. The gradients are used to compute the norm of the gradient, defined as $\|\Delta\vec{g}\| = \|\vec{g}_1 - \vec{g}_2\|$, and the mean gradient, $\bar{g} = (|\vec{g}_1||\vec{g}_2|)^{1/2}$. These quantities are calculated via the effective Hessian tool, *effhess*, in the NAST software package, the details of which can also be found in the user manual.

The next key quantity is the reduced mass of the MECP motion along the reaction coordinate, $\mu_\perp$. This quantity is also computed via the *effhess* code in NAST.

The last key quantities pertain to the geometric and thermodynamic information of the MECP structure. The MECP energy barrier with respect to the reactant, E_X, is required and is found via the output from GAMESS \$MEX routine. The vibrational frequencies and principal moments of inertia for the MECP are computed via the *effhess* routine in NAST.

With all of the above information, the microcanonical rate coefficient can be computed. In order to compute the canonical rate coefficient, the microcanonical rate coefficient is simply averaged over the Boltzmann distribution pertaining to the internal energy of the MECP:

$$k_X(T) = \frac{\sigma}{hQ_R(T)} \int_0^\infty N_X(E)e^{-E/k_bT}dE \qquad (3.39)$$

where $Q_R(T)$ is the partition function of the reactant defined by

$$Q_R(T) = \int_0^\infty \rho_R(E)e^{-E/k_bT}dE \qquad (3.40)$$

T is the temperature, and k_b is the Boltzmann constant. An important aside to note is that if the spin multiplicity between states is unchanging, the NA-TST formulation

reduces down to the CTST formulation for single PES reactions. From here, one can curve-fit a function to the outputted rates, $k_X(T)$, as a function of temperature for use in a chemical kinetics or CFD code.

The procedure for performing these calculations using GAMESS and NAST is detailed in chapter 4.2 and an explicit example of a reaction involving these computations is shown and discussed in chapter 5.

3.5 Reactants, Products, and Transition State Electronic Structure Calculations

3.5.1 Overview of Electronic Structure Calculations: Hartree-Fock Approximation

The electronic structure calculations in this work are performed via the Gaussian 16 software package [26]. Here, a brief overview of what is to be calculated by Gaussian is reviewed.

In order to calculate a general geometric configurations of an atom or molecule, the Schrodinger equation must be solved. In this work, the non-relativistic time-independent Schrodinger equation is used:

$$\hat{H}\Psi = E\Psi \tag{3.41}$$

However, the Born-Oppenheimer (BO) approximation is used. The BO approximation allows for the separate treatment of nuclear and electronic motions, such that the wave function can be separated as:

$$\Psi \approx \Psi_N \Psi_{el} \tag{3.42}$$

Given that we are interested in the electronic structure, particularly in the framework of CTST, a further approximation is made to solve a Schrodinger equation specifically for the electronic motion. The resulting equation is expressed simply as:

$$\hat{H}_{el}\Psi_{el} = E_{el}\Psi_{el} \tag{3.43}$$

where E_{el} is the total scalar electronic energy and eigenvalue of the system, and the Hamiltonian, $\hat{H}_{el}$, is expressed as:

$$\hat{H}_{el} = \underbrace{-\frac{1}{2}\sum_{i=1}^{N}\hat{\nabla}_i^2}_{\substack{\text{electron}\\\text{kinetic energy}}} - \underbrace{\sum_{i=1}^{N}\sum_{A=1}^{M}\frac{Z_A}{|\mathbf{r}_i - \mathbf{R}_A|}}_{\substack{\text{electron-nuclei}\\\text{Coulombic attraction}}} + \underbrace{\sum_{i=1}^{N}\sum_{j>i}^{N}\frac{1}{|\mathbf{r}_i - \mathbf{r}_j|}}_{\substack{\text{electron-electron}\\\text{Coulombic repulsion}}} \tag{3.44}$$

Here, three physical processes are modeled. The first is that of the kinetic energy possessed by the electrons, the second the Coulombic attraction of the electrons and nuclei, and lastly the Coulombic repulsion felt between electrons.

As written, the current formulation is that of a many-body problem. Because many-body problems are generally difficult, if not intractible, to solve, a mean-field approximation is made instead. In order to make this approximation, the wave function is approximated by a Slater determinant wave function:

$$\Psi = \frac{1}{\sqrt{n!}}\begin{vmatrix} \chi_1(\mathbf{x}_1) & \chi_2(\mathbf{x}_1) & \cdots & \chi_n(\mathbf{x}_1) \\ \chi_1(\mathbf{x}_2) & \chi_2(\mathbf{x}_2) & \cdots & \chi_n(\mathbf{x}_2) \\ \vdots & \vdots & \ddots & \vdots \\ \chi_1(\mathbf{x}_n) & \chi_2(\mathbf{x}_n) & \cdots & \chi_n(\mathbf{x}_n) \end{vmatrix} \tag{3.45}$$

where the spin orbitals for the i'th electron, χ_i, are made up of the molecular orbitals, ψ_i, and one spin function, either α or β:

$$\chi_i(\mathbf{x}_n) = \psi_i(\mathbf{r}_n)\,|\alpha\rangle \tag{3.46}$$

$$\chi_i(\mathbf{x}_n) = \psi_i(\mathbf{r}_n)\,|\beta\rangle \tag{3.47}$$

The goal of these calculations is to find the lowest eigenvalue, E_{el}, and its eigenfunction in order to approximate the ground state of the system. In order to do so the wave functions are variationally optimized until a minimum energy configuration

is found. Due to the variationally optimized solution of a self-consistent field (SCF) calculation, this solution is an upper-bound approximation to the true ground state of the system [57]. While there are several methods available for performing an SCF calculation, the Hartree-Fock method is used in this work (and its extensions). This SCF method now solves the following equation:

$$\hat{f}(i)\chi(\mathbf{x}_i) = \epsilon\chi(\mathbf{x}_i) \tag{3.48}$$

where $\hat{f}(i)$ is the Fock operator for the i'th electron:

$$\hat{f}(i) = \hat{h}(i) + v_{\text{eff}}(i) \tag{3.49}$$

with the one-electron core Hamiltonian, $\hat{h}(i)$, for the i'th electron expressed as

$$\hat{h}(i) = -\frac{1}{2}\nabla_i^2 - \sum_A \frac{Z_A}{r_{iA}} \tag{3.50}$$

where the kinetic energy and electron-nuclei interactions are retained within this operator. The two-electron operator, $v_{eff}(i)$, which contains the electron-electron Coulombic interaction term, $\hat{J}(i)$, and an electron-electron exchange term, $\hat{K}(i)$, tracking the electron energy exchange from the antisymmetrized properties of the Slater determinant:

$$v_{eff}(i) = \sum_j \hat{J}(j) - \hat{K}(j) \tag{3.51}$$

An approximation is also made to the molecular orbitals by using a linear combination of atomic orbitals (LCAO) approach. The atomic orbitals, ϕ_μ, are also basis functions for this linear combination, and are weighted by a coefficient, $c_{i\mu}$. The resulting approximation to the molecular orbital function is:

$$\psi_i = \sum_\nu c_{\nu i}\phi_\nu \tag{3.52}$$

Now, multiplying equation (3.48) by the complex conjugate of the spin orbital wave function equation, $\chi_i^*(\mathbf{x}_i)$, and integrating yields the Roothaan-Hall matrix

equation [58, 59]:

$$\mathbf{FC} = \epsilon\mathbf{SC} \tag{3.53}$$

where $\mathbf{C}$ is the LCAO coefficient matrix, ϵ is the diagonal matrix of the orbital energies, $\mathbf{F}$ is the Fock matrix, and $\mathbf{S}$ is the atomic orbital overlap matrix. Explicitly, the latter two matrices are expressed as:

$$\mathbf{F}_{\mu\nu} = \int \chi_\mu^*(\mathbf{x})\hat{f}(\mathbf{x})\chi_\nu(\mathbf{x})d\mathbf{x} \tag{3.54}$$

$$\mathbf{S}_{\mu\nu} = \int \chi_\mu^*(\mathbf{x})\chi_\nu(\mathbf{x})d\mathbf{x} \tag{3.55}$$

This matrix equation is now solved iteratively for the set of coefficients in $\mathbf{C}$ which minimizes the energy of the system. The overlap matrix can also be eliminated by the selection of an orthogonal basis set. Equation (3.53) can be solved for the α or β spin states (restricted), or for both spin states (unrestricted) which results in the Pople-Nesbet matrix equations (equations (3.56) and (3.57)), a coupled eigenvalue problem that solves simultaneously for both the α and β spin states, where the coupling occurs in the Fock matrices:

$$\mathbf{F}^\alpha\mathbf{C}^\alpha = \epsilon^\alpha\mathbf{S}^\alpha\mathbf{C}^\alpha \tag{3.56}$$

$$\mathbf{F}^\beta\mathbf{C}^\beta = \epsilon^\beta\mathbf{S}^\beta\mathbf{C}^\beta \tag{3.57}$$

The unrestricted method allows for the computation of the electronic structure of open-shell molecules. The one complication to the unrestricted method, however, is that it is prone to spin contamination, as the Slater determinant for both equations (3.56) and (3.57) is not an eigenfunction to the spin operator, $\hat{S}^2$. The spin multiplicity of an electronic configuration has an expected value equivalent to $\langle\hat{S}^2\rangle$, which the unrestricted formulation does not recover the expected value. Deviations from this expected value are the result of orbital spin contamination. Large enough

76

deviations from the expected value can be considered erroneous results, thus care should be taken to inspect the spin states after a converged calculation is generated.

In order to now generate an electronic structure, a method for solving the Schrodinger equation, such as Hartree-Fock, and a basis set for the atomic orbitals are needed. The next section provides details on the method and basis sets that are used in this work.

3.5.2 Post-Hartree-Fock Methods: Møller-Plesset Perturbation Theory

Extensions to the Hartree-Fock method exist, and one such extension is Møller-Plesset Perturbation Theory (MPPT) [60]. MPPT is not a variational method, unlike the Hartree-Fock method, thus it does not give an upper-bound solution of the ground-state energy. However, MPPT is generally considered to be a more accurate method with its modeling of electron correlation energies that result from the perturbed solution. As the name suggests, the theory approximates the exact solution as a perturbation from a zeroth order approximation to the exact solution (in this case, the solution of Hartree-Fock). The exact Hamiltonian of the system may be expressed as:

$$\hat{H} = \hat{H}_0 + \hat{V} \tag{3.58}$$

where $\hat{H}_0$ is the Hartree-Fock Hamiltonian, taken as the Fock operator, $\hat{f}$, as described previously. The resulting perturbation, $\hat{V}$, is assumed small from $\hat{H}_0$. Expanding the eigenvalues and eigenfunctions in the following way,

$$\Psi_i = \Psi_i^0 + \Psi_i^{(1)} + \Psi_i^{(2)} + \dots \tag{3.59}$$

$$E_i = E_i^0 + E_i^{(1)} + E_i^{(2)} + \dots \tag{3.60}$$

allows for a collecting of like powers upon multiplying equations (3.59) and (3.60)

into the Schrodinger equation (3.41). Omitting the mathematical details, which can be found in Moller and Plesset [60], the Hartree-Fock energy, E_0, is shown to be recovered from the first-order correction:

$$E_0 = E^0 + E^{(1)} \tag{3.61}$$

and the higher magnitude terms $(E_i^{(2)}, E_i^{(3)}, \ldots)$ from equation (3.60) correspond to the higher order corrections, which are of the electron correlation energy, E_{corr}. The exact eigenvalue can be then be written as

$$E_{el} = E_0 + E_{corr} \approx E_0 + E^{(2)} + E^{(3)} + \ldots + E^{(n)} \tag{3.62}$$

The higher order MPn method used (where n is an integer corresponding to the maximum power of the expansion), the more correction terms are applied to the correlation energy; however, this larger correction comes with an increased computational time that scales with the number of basis functions used in the selected basis set [61]. The resources afforded for this work allow for reasonable computation times using the MP2 method with the selected basis sets, which are discussed in the next section. If more accuracy is needed, coupled cluster calculations should be used as they have inherently better treatment of other electron effects and scale better than even higher-order MPn methods of comparable accuracy as discussed by Cremer [61].

3.5.3   Levels of Theory

In order to properly notate the methodology used for the electronic structure calculations, a quick outline of "level of theory" is presented, which parallels the notation found in the literature.

The notation is literature is *method/basis//method/basis*, where "basis" refers to the basis set being used in the LCAO approximation of equation (3.52). The first *method/basis* group refers to the single point energy calculation level of theory. The second *method/basis* group is the level of theory of the calculation used for the geometry of the compound. If there is only one group listed, it is assumed that the

energy calculation and geometry are both calculated using that method and basis. If the groups are *method//method/basis*, the energy calculation utilizes the same basis set as the geometry, while instead using the different method listed.

Keeping in mind the potential for highly oxidized sulfur states in conjunction with highly electronegative compounds (oxygen and fluorine), the levels of theory selected for this work are *MP2/cc-pvtz* and *MP2/6-311+G(3df)*. These basis sets are all commonly found as default options in modern electronic structure codes and are implemented accordingly for the N, O, F, and S atoms, thus will not be listed here.

Chapter 4

Computational Fluid Dynamics, Electronic Structure, and Reaction Kinetics Tools

4.1   Solution Adaptive Numerical Simulator (SANS)

The Solution Adaptive Numerical Simulator (SANS) code [62] is currently being developed in Professor David Darmofal's group in the Aeronautics and Astronautics department at MIT. Originally instantiated as *Project X* [63], the SANS code applies higher-order finite element techniques with output-based adaptive mesh refinement capability to systems of partial differential equations, which in the case of this work are the governing equations for a TCNE flow described in chapter 2.

Output-Based Grid Adaptation

One form of solution-based grid adaptation is output-based grid adaptation. This is where the grid is adapted to minimize the estimated error in a scalar output from the solution e.g. lift, drag, heat flux, total enthalpy. The general process used for output-based grid adaptation in SANS is shown in Fig. 4-1. Yano and Darmofal [64] introduced the MOESS algorithm for the discontinuous Galerkin (DG) method. This

method uses a local sampling process to generate surrogate models for the dependence of the output errors on the grid. These surrogate models are then optimized to obtain a new grid with minimized output error. Recently Carson et al. [65] extended the MOESS algorithm to the continuous Galerkin (CG) method referred to as C-MOESS.
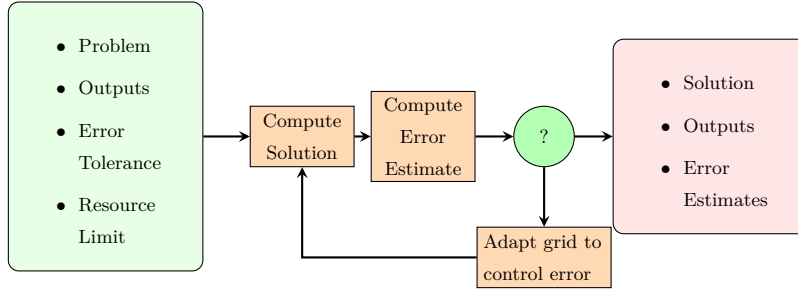
Figure 4-1: Output-based grid adaptive procedure

The user first defines the problem: for example, that of a 2D TCNE flow about a hypersonic body. The user selects for the TCNE governing equations implemented within SANS, provides the desired boundary conditions, geometry, output of interest, the desired error tolerance (in this work, 10 order of magnitude reduction in residual outputs), and the desired cost constraint the optimization procedure operates within (in this work, a set degrees-of-freedom count).

Once the problem definition has been input into SANS, a mesh is automatically generated (e.g. AVRO, Epic) for the input geometry, a solution is computed along with its error estimate, and then the cutoff criteria checked. If not met, the process proceeds to adapt the mesh to the local error estimates computed via MOESS. The optimized mesh metric supplied by MOESS is then used to generate a new mesh, and the iteration continues until the desired cutoff is met. For this work, the cutoff criterion is defined by the number of mesh adaptations that supplies asymptotically converging values of the output; generally, anywhere between 30-50 adaptations has been found to be sufficient. After the loop finishes, the final solution, outputs, and error estimates are given.

An important note to mention: because the target degree-of-freedom (DoF) count tends to be low (order 1,000-10,000) and the numerical algorithms highly parallelized,

iterating to 50 or more adaptation loops comes with minimal real-world run-time penalty, depending on the discretization scheme used. One such scheme, which this work relies on, is the Variational Multiscale with Discontinuous Subscales (VMSD) discretization scheme developed by Huang [66]. Using this scheme, coupled with the homotopy solution procedure developed and implemented for use in SANS by Couchman [67], most cases of interest for moderate chemical species count ($n_s < 5$) can be ran on a multi-core laptop in a matter of hours.

General Definition of Partial Differential Equations in SANS

Let us consider a general system of m nonlinear advection-reaction equations on a domain, $\Omega \subset \mathbb{R}^d$, subject to Dirichlet boundary conditions, u_B on $\partial\Omega$:

$$\mathcal{L}(u) \equiv \nabla \cdot \left[\vec{F}(u) - \vec{G}(u, \nabla u)\right] + S(u, \nabla u) - f(\vec{x}) = 0. \qquad (4.1)$$

where $u : \mathbb{R}^{d+1} \to \mathbb{R}^m$ are conservation variables, $\vec{F}(u)$ are the advective fluxes, $\vec{G}(u, \nabla u)$ are the diffusive fluxes, $S(u, \nabla u)$ represents the source terms, and $f(\vec{x})$ is the forcing function. The advective fluxes are such that for a system of m equations in d spatial dimensions, $\vec{F} : \mathbb{R}^m \to \mathbb{R}^{m \times d}$, and the eigenvalues of

$$\frac{\partial}{\partial u}\left(\vec{F} \cdot \vec{n}\right) \qquad (4.2)$$

are real for all directions $\vec{n}$. The source term is such that $S : \mathbb{R}^m \times \mathbb{R}^{m \times d} \to \mathbb{R}^m$, and the forcing function is such that $\vec{f} : \mathbb{R}^d \to \mathbb{R}^m$ independent of the solution state. We will distinguish between inner products involving *state vectors* (e.g. $u, v \in \mathbb{R}^m$) and *spatial vectors* (e.g. $\vec{x}, \vec{y} \in \mathbb{R}^d$) as follows:

- Let u and v be two state vectors i.e. $u, v \in \mathbb{R}^m$, then their inner product is denoted as $u^T v$ and is a *real number*.

- Let $\vec{x}$ and $\vec{y}$ be two spatial vectors i.e. $\vec{x}, \vec{y} \in \mathbb{R}^d$, then their inner product is denoted as $\vec{x} \cdot \vec{y}$ and is a *real number*.

Spatial vectors will be denoted with an overarrow: $\vec{(\cdot)}$.

By multiplication of Eq. (4.1) by a test function $w \in \mathcal{W}$, and application of integration by parts, we obtain the weak form residual statement,

$$u \in \mathcal{W} \, : \, \mathcal{R}\left(u, w\right) = 0, \quad \forall w \in \mathcal{W}. \tag{4.3}$$

We also consider a general *scalar* output functional, $\mathcal{J} \, : \, \mathcal{W} \to \mathbb{R}$,

$$\mathcal{J}\left(u\right) = \int_{\Omega} g_{\Omega}\left(u\right) \, d\Omega + \int_{\partial\Omega} g_{\partial\Omega}\left(u\right) \, ds. \tag{4.4}$$

It is this output functional that takes the solution to our PDE and returns our quantity of interest, for example the total enthalpy:

$$g_{\Omega}\left(u\right) = \alpha \left(h + U^2/2\right) + \beta \tag{4.5}$$

where α and β are user-defined constants used for the normalization and offset of the total enthalpy quantity, respectively, as desired. We seek to minimize the effect of discretization error with respect to such a scalar quantity, as well as other physically informed scalar quantities.

We can related perturbations $u \to u + \delta u$ to perturbations in $\mathcal{J}$ via the adjoint,

$$\phi \in \mathcal{W} \, : \, \bar{\mathcal{R}}'\left[u, u + \delta u\right]\left(w, \psi\right) - \bar{\mathcal{J}}'\left[u, u + \delta u\right]\left(w\right) = 0, \quad \forall w \in \mathcal{W}, \tag{4.6}$$

where we use the mean value linearizations of the residual and output functional,

$$\bar{\mathcal{R}}'\left[u, u + \delta u\right]\left(w, \psi\right) \equiv \int_0^1 \mathcal{R}'\left[u + s\delta u\right]\left(w, \psi\right) \, ds, \tag{4.7}$$

$$\bar{\mathcal{J}}'\left[u, u + \delta u\right]\left(w\right) \equiv \int_0^1 \mathcal{J}'\left[u + s\delta u\right]\left(w\right) \, ds, \tag{4.8}$$

and $\mathcal{R}'\left[z\right]\left(\cdot, \cdot\right)$ and $\mathcal{J}'\left[z\right]\left(\cdot\right)$ are the Fréchet derivatives of the residual and output functional with respect to the first argument at z.

4.1.1 TCNE Implementation

The TCNE module in SANS has been implemented following the form of equation (4.1). Using the 2D TCNE equations, which are the highest dimensional case used in this work, the state vector, here denoted as the traditional Q, is the vector of primitive variables and takes the form

$$
Q = \begin{bmatrix} \rho_1 \\ \vdots \\ \rho_{n_s} \\ u \\ v \\ T_{tr} \\ T_V \end{bmatrix},
\tag{4.9}
$$

the inviscid fluxes in the x and y directions, F_x and F_y, take the form of

$$
F_x = \begin{bmatrix} \rho_1 u \\ \vdots \\ \rho_{n_s} u \\ \rho u^2 + p \\ \rho uv \\ (E+p)u \\ E_V u \end{bmatrix}
\text{ and } F_y = \begin{bmatrix} \rho_1 v \\ \vdots \\ \rho_{n_s} v \\ \rho uv \\ \rho v^2 + p \\ (E+p)v \\ E_V v \end{bmatrix},
\tag{4.10}
$$

and the diffusive fluxes in the x and y directions, G_x and G_y, are

$$
G_x = \begin{bmatrix} \rho D_1 \nabla y_1 \\ \vdots \\ \rho D_{n_s} \nabla y_{n_s} \\ \tau_{xx} \\ \tau_{xy} \\ \tau_{xx} u + \tau_{xy} v - (q_{tr,x} + q_{V,x}) + \rho \sum h_s D_s \nabla y_s \\ -q_{V,x} + \rho \sum h_{V,s} D_s \nabla y_s \end{bmatrix} \tag{4.11}
$$

and

$$
G_y = \begin{bmatrix} \rho D_1 \nabla y_1 \\ \vdots \\ \rho D_{n_s} \nabla y_{n_s} \\ \tau_{yx} \\ \tau_{yy} \\ \tau_{yx} u + \tau_{yy} v - (q_{tr,y} + q_{V,y}) + \rho \sum h_s D_s \nabla y_s \\ -q_{V,y} + \rho \sum h_{V,s} D_s \nabla y_s \end{bmatrix} . \tag{4.12}
$$

The viscous stress and heat transfer terms are in their abbreviated forms here, but are shown in their expanded forms previously in chapter 2. The source terms, which are kept in a general form here for the sake of brevity, but are also detailed in chapter 2, are

$$
S = \begin{bmatrix} \dot{w}_1 \\ \vdots \\ \dot{w}_{n_s} \\ 0 \\ 0 \\ 0 \\ -p_e \nabla \cdot \vec{u} + S_{VT} + S_{ET} + S_{el-ion} + S_{prod} \end{bmatrix} , \tag{4.13}
$$

For the TCNE implementation, there are no forcing terms, thus $f(\vec{x}) = \vec{0}$. All of the

calculations that occur for the vector component construction of these vectors are implemented according to the models described in chapter 2.

Further Reading on SANS

SANS contains a suite of exemplary features that allow for the fast and rapid implementation of partial differential equation models [62], of which the explanations do not all fit within the scope of this thesis. For detailed discussions, please refer to the literature for MOESS [64, 65], the various discretization schemes [66], automatic differentiation [68], shock capturing [67], artificial viscosity and stabilization [67], and the homotopy continuation method [67], all of which allow for this code to not only run smoothly, but advance the numerical simulation capabilities for hypersonic TCNE flows as a whole.

4.1.2 Validation Cases

1D Multi-Component Euler TCNE Oxygen Shocktube

A TCNE flow evolving past a shockwave which consists only of oxygen species is considered. In this particular case study, the flow is modeled as a multi-component Euler flow, namely effects from diffusion, viscosity, and thermal conductivity are ignored. This exclusion provides a convenient test bed for the verification and validation of the advective fluxes and source terms within the TCNE module. Further explanation of this modeling can be found in Sabo et al [69].

The flow is computed in the reference frame of the shock, and the domain inflow location is set immediately post-shock. Select cases from Shoev and Bondar [70] are used in this example problem. The inlet conditions are found using Rankine-Hugoniot relations assuming frozen chemistry past a 1D normal shock for the pure molecular oxygen environment. The outlet boundary condition is set to the outlet pressure found from Rankine-Hugoniot relations for equilibrium conditions. These parameters are listed in table 4.1. The chemical reactions and their modified-Arrhenius parameters for the forward rates are listed in table 4.2. This work compares the differences in

discretization between the Landau-Teller VT relaxation model and the model derived by Kustova and Oblapenko [32]. The domain length L is set to 0.2m. The chemical reactions for the oxygen species are also taken from Shoev and Bondar and are listed in table 4.2.

u_∞ [m/s]	p_∞ [torr]	T_∞ [K]	p_2 [torr]
3070	2	295	223.18
3400	1	295	138.6

Table 4.1: The upstream freestream conditions and the outlet pressure conditions for the oxygen shocktube problem.

No.	Reaction	A	β	E_a [K]
1	$O_2 + O_2 \longleftrightarrow O + O + O_2$	3.8e27	-3.1	59,400
2	$O_2 + O \longleftrightarrow O + O + O$	2.7e18	-0.53	59,400

Table 4.2: Chemical reactions and modified-Arrhenius parameters for the oxygen shocktube problem.

The methodology for computing these oxygen shocktube flows is as follows:

1. The MOESS algorithm is used to obtain a grid, solution, and error estimate corresponding to,

$$\mathcal{J}(u) = \int_{\partial\Omega} \mathcal{F} d\partial\Omega. \tag{4.14}$$

or

$$\mathcal{J}(u) = \int_{\Omega} \mathcal{F} d\Omega. \tag{4.15}$$

where $\mathcal{F}$ is an integrable scalar quantity over either a surface or a volume, as shown above, respectively.

2. An estimate of the discretization error for the transrotational and vibrational temperatures over the shocktube length is desired. For this estimate, we use the grid and solution obtained in the previous step and calculate the DWR error

88

estimate to the following outputs,

$$\mathcal{J}_{T_{tr}}(u; x_i) = \int_\Omega T_{tr} \frac{1}{h\sqrt{2\pi}} \exp\left\{\left(-\left(\frac{x-x_i}{h}\right)^2\right)\right\} d\Omega, \qquad (4.16)$$

$$\mathcal{J}_{T_v}(u; x_i) = \int_\Omega T_v \frac{1}{h\sqrt{2\pi}} \exp\left\{\left(-\left(\frac{x-x_i}{h}\right)^2\right)\right\} d\Omega, \qquad (4.17)$$

where x_i are the locations of interest to obtain discretization error estimates, and $h = 3 \times 10^{-3}$. Note that a Gaussian weighted integral is used, rather than a pointwise value. This integral formulation is to ensure that the resulting adjoint problem is well-posed.

3. A suitable output functional is picked. Generally, an output functional that measures a physical quantity of interest is desired. For this example problem, the thermodynamic non-equilibrium over the shocktube is chosen.

4. Repeat steps (1) and (2) for the desired output functionals and desired physical models.

Figures 4-2 and 4-3 display the results from table 4.1 in listed order. MOESS adapts to minimize the discretization error in

$$\mathcal{J}(u) = \int_\Omega \left(\frac{T_{tr} - T_v}{T_{tr}}\right)^2 d\Omega, \qquad (4.18)$$

which measure of the degree of thermodynamic non-equilibrium over the length of the shocktube. The grid is expected to be refined in strong regions of local thermodynamic non-equilibrium (LTE), as measured by the temperature difference in equation (4.18), and has in fact been observed. These cases have been ran at polynomial order 1 with a target DoF count of 1024 and produce grid-converged results. The results at the outlet of the domain reach both LTE and chemical equilibrium and agree favorably with NASA's CEA code for equilibrium flow past an incident shock with the same inlet conditions and composition. The non-equilibrium evolution of the temperature profiles agree favorably with the results of Shoev and Bondar [70] for both VT relaxation models.
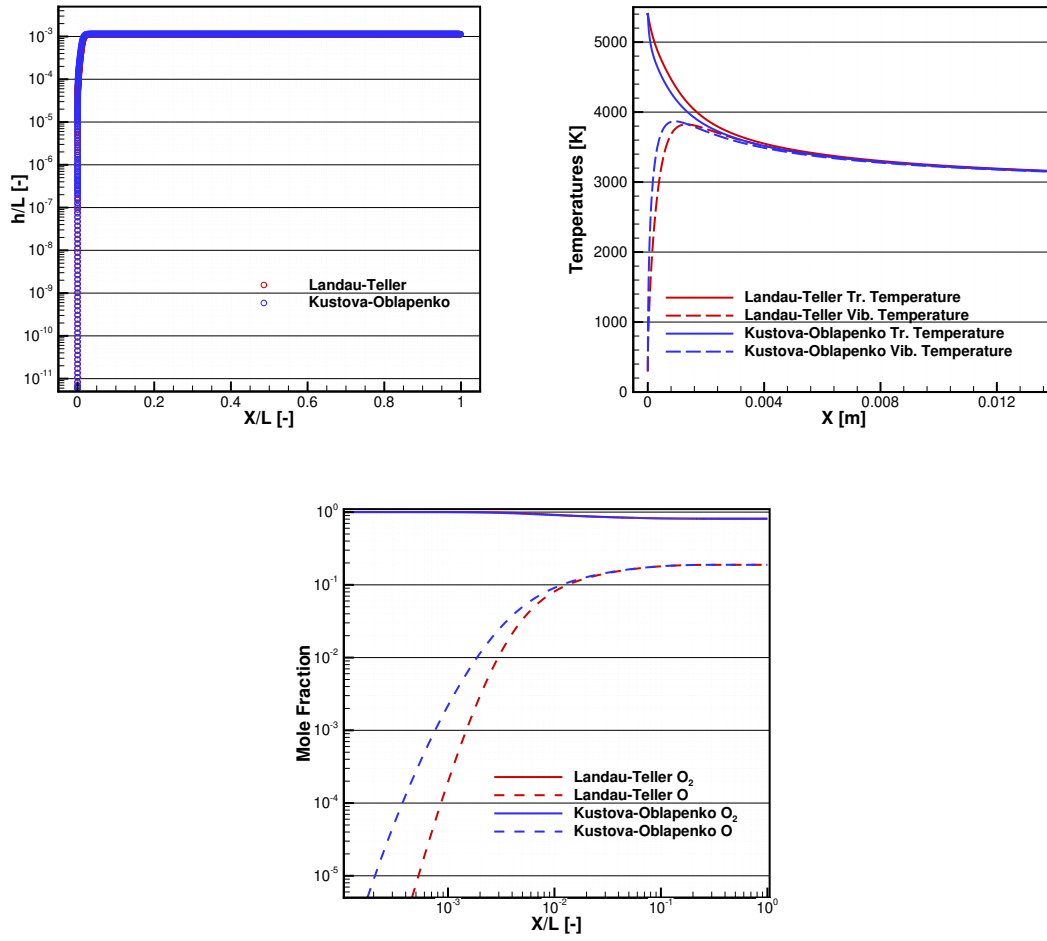
Figure 4-2: Comparison of Landau-Teller and Kustova-Oblapenko models on final grid for the oxygen shocktube case under conditions 1
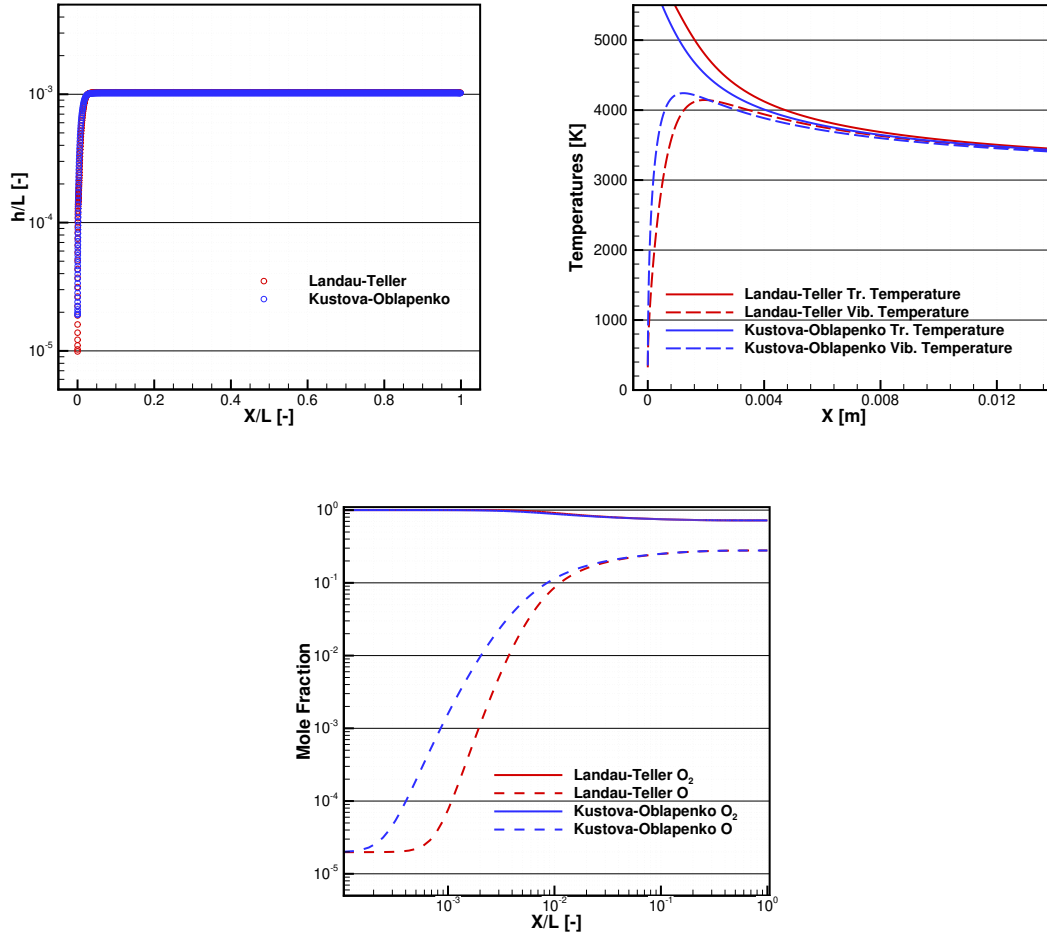
Figure 4-3: Comparison of Landau-Teller and Kustova-Oblapenko models on final grid for the oxygen shocktube case under conditions 2

Figure 4-4 compares the the Landau-Teller and Kustova-Oblapenko models for vibrational-translational relaxation, including estimations of the effect of discretization error on the translational and vibrational temperatures for each model on their respective grids. It is seen that for the majority of post-shock profile, the estimate of the discretization error is less than the difference in the profiles for the two models. However, for $x \lessapprox 2 \times 10^{-3}$, it is seen that the difference between the vibrational temperature predicted by the two models is less than the estimation of the discretization error.
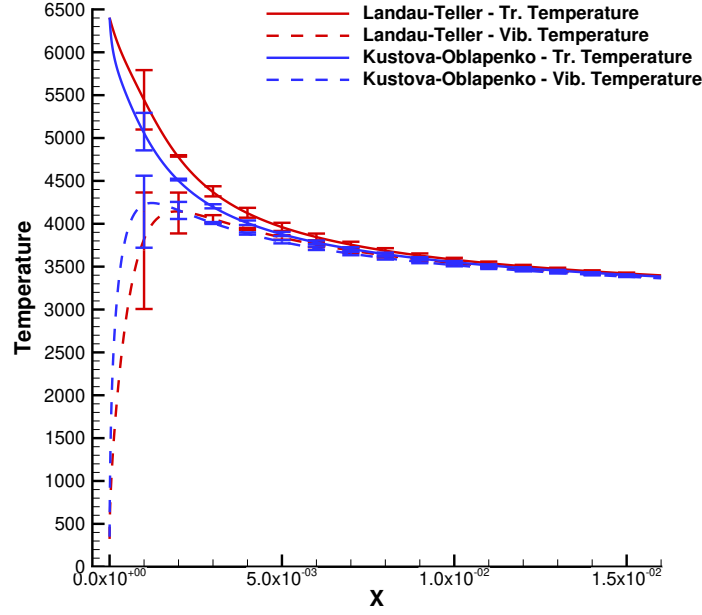
Figure 4-4: Comparison of Landau-Teller and Kustova-Oblapenko models on final grid for the oxygen shocktube case under conditions 2 including error estimates

2D Double-Ramp Multi-Component Euler TCNE Flow

The supersonic double ramp from Carnes et al. [71] is considered. This case consists of a 25° / 37° wedge in an approximated Mach 3.6 flow. A shock forms at the front of each of the ramps, with the shocks intersecting approximately 60% along the domain. The inflow conditions are given in table 4.3. Unlike Carnes et al. , we use a nitrogen freestream (with a two species: N_2 and N), and a two temperature model. The stagnation temperature is sufficiently low that we do not expect dissociation of the N_2.

Property	Value
ρ_{N_2} [kg m^{-3}]	9.964×10^{-4}
ρ_N [kg m^{-3}]	0.0
Velocity [m s^{-1}]	1861.03531021
T_{tr} [K]	652
T_{vib} [K]	652

Table 4.3: Inflow properties for the Inviscid Mach 20 Cylinder

The MOESS algorithm is applied to this case, adapting to the average total enthalpy over the entire computational domain, targeting 1000 DOFs in the final grid. The final grid for the case is given in figure 4-5. The final grid is also shown for the same inflow conditions and output functional, but using a perfect gas model instead. Note that the case using TCNE modeling includes additional resolution in the slip line behind the shock-shock intersection point.
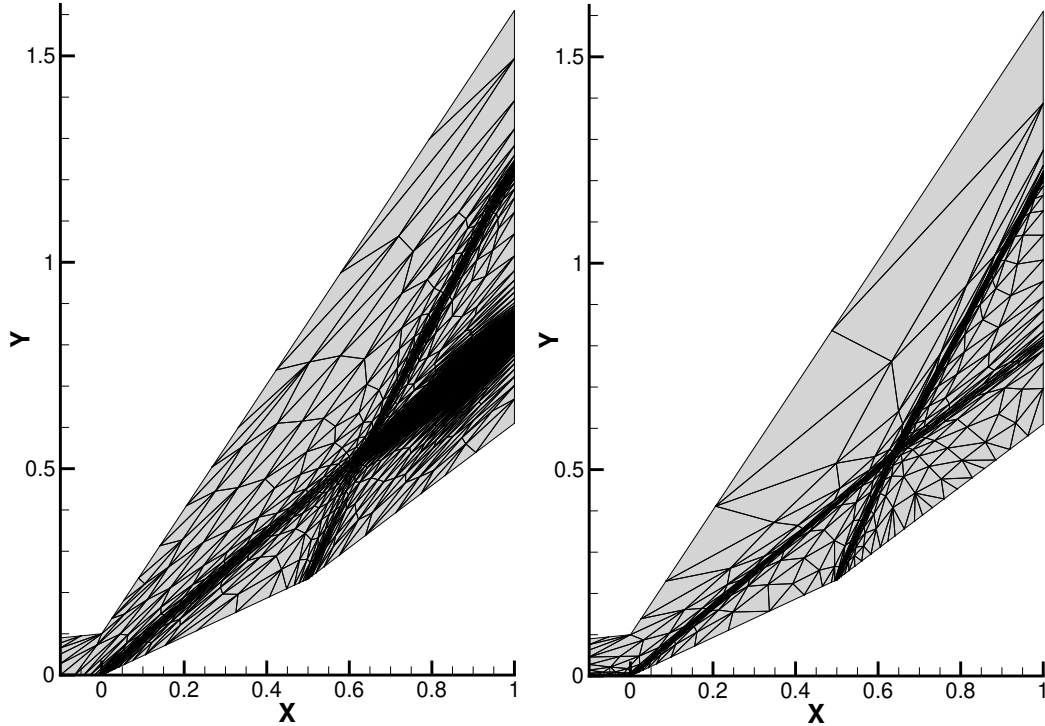
Figure 4-5: Final grid for the double wedge case: thermo-chemical non-equilibrium (left) perfect gas (right)

The translational and vibrational temperature fields (on the final grid) are given in figure 4-6. It is interesting to note that there is significant thermal non-equilibrium behind the shock. This is due to the very low pressure ($\approx 125\ Pa$ in the freestream). This low pressure results in very large vibrational-translation relaxation timescales, shown in figure 4-7. The vibrational relaxation times are known to be poorly approximated for N_2-N collisions by the Millikan-White formula and can be an order of magnitude lower at larger temperatures when examined via quasi-classical trajectory (QCT) methods, as reported by Oblapenko [72]. Oblapenko also states that "..., since the Millikan-White formula may not be necessarily valid for the N_2+N system, [it] should not be considered a benchmark for the QCT-based results." Clearly, the degree of LTE computed in this test case should not be taken as accurate when compared with physical reality; however, the Millikan-White vibrational relaxation time model is producing the expected results.
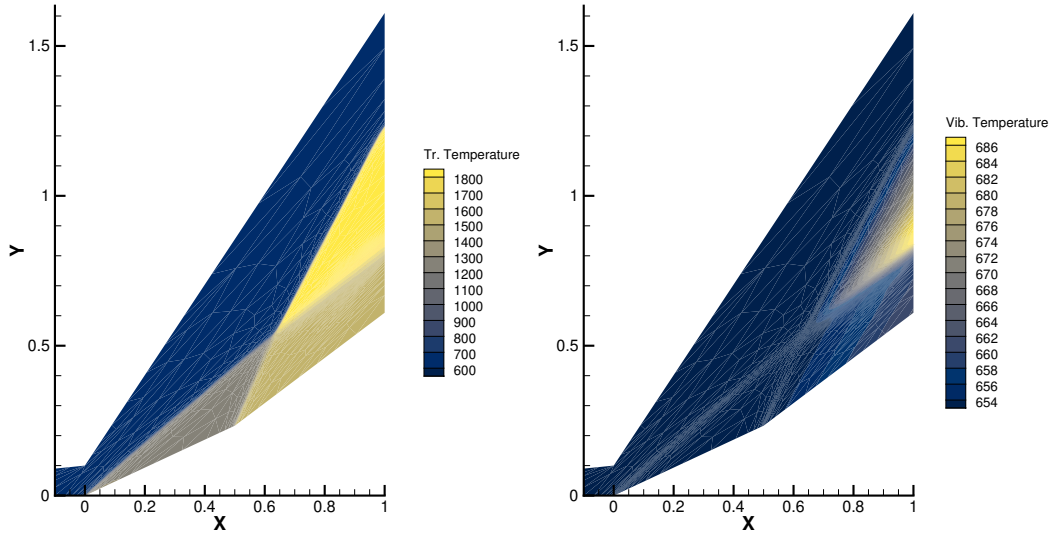
Figure 4-6: Temperature field on the final grid in the double wedge case: translational (left) vibrational (right)
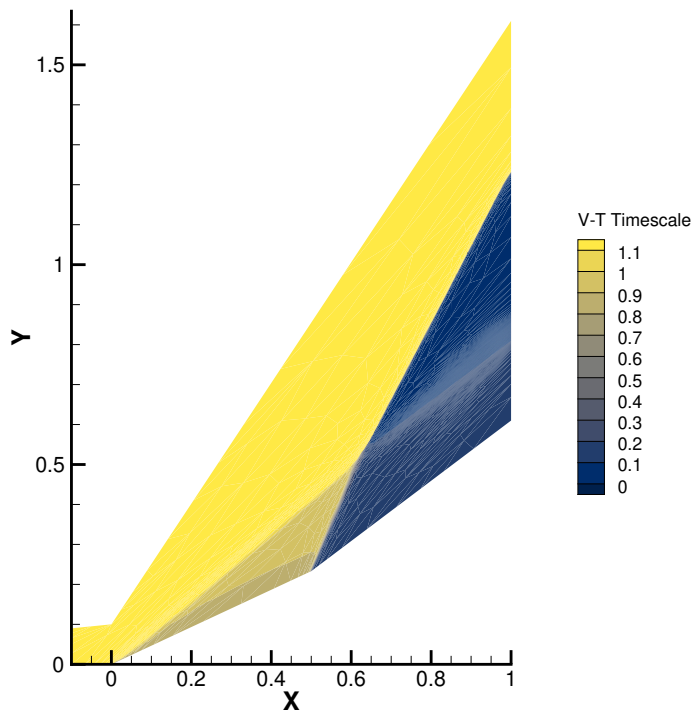
Figure 4-7: Vibrational-translation relaxation timescale on the final grid in the double wedge case

4.2 Electronic Structure Optimization Softwares: Gaussian and GAMESS

This work utilizes two electronic structure softwares for molecular geoemtry optimization and energy calculations. For reactions involving a transition state, Gaussian, Inc.'s Gaussian 2016 [26] software has been used for all necessary quantum chemistry computations. For reactions involving spin-diabatic states that require the traversing of a minimum energy crossing point (MECP), GAMESS [27] has been used for all necessary quantum chemistry computations.

Much of the documentation for these codes can be found online; however, the general calculation procedure and inputs will be given in the following sections. If slight modifications to the general process occur, they will be noted with a brief explanation. The intent is to not only document how these calculations were performed,

but to give a starting point for future exploration of the chemical reactions presented here, as more detailed study is required for the continual improvement of the kinetic modeling.

4.2.1 Gaussian for CTST Reactions

The geometry optimization input files for both reactant/product geometry minimization and transition state minimization are outlined in this section for the CTST reactions in this work. A brief description of and reasoning for the inputs are presented. The input file code can be used to verify calculations, or improve upon them for future works.

For the reactant and product species geometry optimization (minimization), the general template is listed below. The `calcall` option is used to generate the force constants at every step in the calculation. The tolerance for the minimization procedure was set to `verytight`, and the `maxcycles` were set to 300 to allow for iteration overhead. The initial `guess` for the molecular orbitals used the `mix` command and used the `huckel` orbitals option, which generates the computed huckel orbitals for the first iteration only - all subsequent iterations used the previous iteration as the initial guess, which was found to improve reliability in optimization convergence. Here, `LoT` corresponds to the level of theory used, which for this work is either `MP2/cc-pvtz` or `MP2/6-311+G(3df)`. The `scf` calculation utilizes the `xqc` algorithm set at a `tight` tolerance. The remaining options and overlays are relatively standard procedure; more information on them can be found on Gaussian's website.

The `name` of the species is purely cosmetic for the calculations done in this work. The charge `c` and multiplicity `s` are set based on the compound being studied. The input geometry for this work is listed in Z-matrix format immediately after the charge and multiplicity input line, denoted by `<Z-matrix>`.

Listing 4.1: Gaussian input file format for geometry minimization optimizations.

```
%chk=check.chk
%mem=8192mb
%NProcShared=8

#P OPT(Calcall, verytight, maxcycles=300) guess=(mix,huckel) LoT
    ↪ scf=(tight, xqc) integral=(grid=ultrafine, Acc2E=12) iop
    ↪ (2/9=2000,1/152=300,9/6=300,5/7=0)

name

c s
<Z-matrix>
```

The template for the transition state (saddle point) optimization input file used in this work is listed below. The `noeigentest` option is utilized to tell the optimization algorithm to keep going in the event of multiple imaginary eigenvalues being detected, as they often will disappear upon further iteration. The force constants were calculated at every step via the `calcall` command, the convergence tolerance set to `tight`, the `maxstep` per iteration set to 5, and the `maxcycles` set to 500 for adequate iteration headroom. The `guess` option utilizes the `huckel` for the generation of the initial guess orbitals, while the computed orbitals at each optimization step are used for the initial guess of the proceeding steps. Here, as with before, `LoT` corresponds to the level of theory used, which for this work is either `MP2/cc-pvtz` or `MP2/6-311+G(3df)`. The `scf` calculation utilizes the `xqc` algorithm and has its `maxcycle` set to 150 to allow for adequate iteration headroom.

If no transition states were initially found, chemical intuition was used to tweak the initial guesses several times. The use of Gaussian's `qst2` and `qst3` algorithms were also trialed if the initial guess tweaks were proving to be unsuccessful; however, for those cases, neither the `qst2` or `qst3` algorithms were able to generate successful transition states.

97

Listing 4.2: Gaussian input file format for TST optimizations.

```
%chk=check.chk
%mem=8192mb
%NProcShared=8

#P opt=(ts, noeigentest, calcall, tight, maxstep=5, maxcycles=500)
    ↪  guess=(mix,huckel) LoT scf=(tight, xqc, maxcycle=150)
    ↪ integral=(grid=ultrafine, Acc2E=12) iop
    ↪ (1/8=2,2/9=2000,1/152=500,9/6=500,5/7=0)

name

c s
<Z-matrix>
```

4.2.2 GAMESS for Reactions Involving Minimum Energy Crossing Points (MECP's)

The reaction studied in this work corresponds to the singlet-triplet system

$$SO_2F_2 \xrightarrow{singlet-triplet} SO_2F_2 \tag{4.19}$$
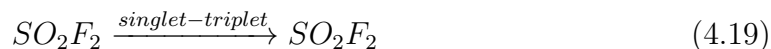
thus the input files below contain the actual geometric inputs used for the calculations done in this work. However, these listings are intended to be used as templates for other calculations of similar types. Familiarizing oneself with the GAMESS input files is important for running successful calculations, as it offers fine control over the input parameters. These computations are set up for the *MP2/6-311+G(3df)* level of theory. Certain input data has been omitted in order to keep the listings as brief as possible, while still being as instructive as possible.

Listing 4.3 shows the optimization input file for the SO_2F_2 product molecule in its triplet state. Similar to the Gaussian optimization, it also uses mixed Huckel orbitals for its initial guess. The geometry here (and for later calculations) are given in Cartesian coordinates. In order to optimize for the singlet geometry, simply change the `mult=3` argument to `mult=1`.

Listing 4.3: GAMESS input file format for reactant/product optimizations.

```
 $contrl scftyp=uhf mplevl=2 runtyp=optimize
 icharg=0 mult=3 ispher=-1 maxit=200 $end
 $system mwords=2000 $end
 $statpt hssend=.t. nstep=400 $end
 $SCF dirscf=.t. SOSCF=.F. DIIS=.T. $end
 $basis gbasis=N311 ngauss=6 ndfunc=3
 nffunc=1 diffsp=.true. $END
 $guess guess=huckel mix=.t. $end
 $DATA
 SO2F2
C1
S 16 0.00000000 0.00000000 0.00000000
O 8 0.00000000 -1.26835700 0.64996100
O 8 0.00000000 1.26787100 0.64929900
F 9 1.17223800 0.00020500 -1.07619000
F 9 -1.17223800 0.00020500 -1.07619000
 $END
```

Listing 4.4 displays the input for the Hessian calculation for the same SO_2F_2 product molecule. The molecular orbital data is read in through the input file, and is generated via the previous optimization calculation. This Hessian calculation is performed in order to both calculate the vibrational frequencies and verify that the polyatomic molecule has $3N-6$ vibrational degrees of freedom, where N is the number of atoms.

Listing 4.4: GAMESS input file format for reactant/product Hessian calculations for thermodynamic properties.

```
$contrl scftyp=uhf mplevl=2 runtyp=hessian
icharg=0 mult=3 ispher=-1 maxit=200 $end
$system mwords=2000 $end
$SCF dirscf=.t. SOSCF=.F. DIIS=.T. damp=.t. $end
$statpt hssend=.t. nstep=400 $end
$basis gbasis=N311 ngauss=6 ndfunc=3
nffunc=1 diffsp=.true. $end
$guess guess=moread norb=233 $end
$DATA
SO2F2
C1
 S 16.0 0.0690896008 0.6642389969 0.1402334998
 O 8.0 -0.0471290924 -2.6621639881 0.6478810619
 O 8.0 0.1016412969 2.0435205836 -0.2124347104
 F 9.0 1.0865515046 -0.0826351623 -0.8421083268
 F 9.0 -1.2101533098 0.0369635700 -0.5866915245
 $END

 --- OPTIMIZED UHF MO-S --- GENERATED AT 21:50:42 01-FEB-2022
E= -747.2765866003, E(NUC)= 243.8806032204
 $VEC
 1 1-4.11279627E-01-6.54756313E-01-1.27735296E-02 2.83662108E
    ↪ -03-1.73072167E-03
 1 2 2.73094870E-07 3.34552677E-05-3.77625429E-05 3.18547064E-04
    ↪ 2.10188501E-05
 .
 .
 .
 33 46-4.82550045E-03-8.40678914E-03-9.76058182E-03-7.02615240E
    ↪ -03-3.32792816E-03
 33 47-8.26337572E-03-3.67878343E-03-4.83173137E-03
 $END
```

Listing 4.5 displays the input for the projected Hessian calculation for the same SO_2F_2 product molecule. This calculations projects the translational and rotational degrees of freedom out of the Hessian. If the geometry is at a stationary point, there are six zero frequency values shown with no imaginary frequencies for the vibrations.

Listing 4.5: GAMESS input file format for reactant/product Hessian projection calculations (useful for strict verification check of stationary point geometry).

```
$force rdhess=.t. projct=.t. $end
$contrl scftyp=uhf mplevl=2 runtyp=hessian
icharg=0 mult=3 ispher=-1 maxit=200 $end
$system mwords=2000 $end
$SCF dirscf=.t. SOSCF=.F. DIIS=.T. damp=.t. $end
$statpt hssend=.t. nstep=400 $end
$basis gbasis=N311 ngauss=6 ndfunc=3
nffunc=1 diffsp=.true. $end
$DATA
SO2F2
C1
 S 16.0 0.0690896008 0.6642389969 0.1402334998
 O 8.0 -0.0471290924 -2.6621639881 0.6478810619
 O 8.0 0.1016412969 2.0435205836 -0.2124347104
 F 9.0 1.0865515046 -0.0826351623 -0.8421083268
 F 9.0 -1.2101533098 0.0369635700 -0.5866915245
 $END

 $HESS
ENERGY IS -747.2765866870 E(NUC) IS 243.8806032213
 1 1 2.88624305E-01 1.61746331E-02 9.00181816E-03-3.14370155E
     ↪ -04-2.82871338E-04
 1 2-2.55270453E-05-4.98785587E-02-1.38704980E-02 5.92110156E
     ↪ -04-9.69806080E-02
 .
 .
 .
 15 2-1.18179372E-04 1.07476863E-02-1.31978622E-03 2.22159235E-02
     ↪ 1.44607667E-02
 15 3 6.20256323E-03 2.25766741E-02 7.39117813E-02 3.72383542E-02
     ↪ 7.46123098E-02
 $END
```

Listing 4.6 displays the input for the MECP geometry optimization for the SO_2F_2 singlet-triplet seam. GAMESS \$MEX group is utilized in the input file to facilitate the computation of the MECP geometry. For this calculation, both sets of molecular orbitals from the singlet and triplet geometry optimization calculations are used to help facilitate the calculation (denoted as `$VEC1` and `$VEC2`, respectively). The initial guess geometry for this case has been taken to be the optimized singlet SO_2F_2, but may be taken as the triplet if desired, or anything close to the MECP geometry if information about it is already known.

Listing 4.6: GAMESS input file format for MECP optimizations using \$MEX group.

```
$contrl runtyp=mex icharg=0
maxit=200 ispher=-1 mplevl=2 $end
$mex scf1=uhf scf2=uhf mult1=1 mult2=3
nstep=1000 nmos1=233 nmos2=233 nrdmos=3 $end
$scf dirscf=.t. SOSCF=.F. DIIS=.T. shift=.t. damp=.t. $end
$system mwords=2000 $end
$basis gbasis=N311 ngauss=6 ndfunc=3
nffunc=1 diffsp=.true. $end
$DATA
SO2F2
C1
 S 16.0 0.0000000008 0.0000033019 -0.0136720732
 O 8.0 -0.0000000012 -1.2507052172 0.6338272292
 O 8.0 -0.0000000001 1.2507048271 0.6338316602
 F 9.0 1.1430658995 -0.0000394553 -1.0535534087
 F 9.0 -1.1430658989 -0.0000394565 -1.0535534074
 $END

--- OPTIMIZED UHF MO-S --- GENERATED AT 22:16:41 01-FEB-2022
E= -747.4480523064, E(NUC)= 290.8339484032
 $VEC1
 1 1 4.11283415E-01 6.54755081E-01 1.27442208E-02-2.82174097E-03
    ↪ 1.84413611E-03
 1 2 1.49738916E-04 0.00000000E+00 3.02453149E-09-1.37342761E-04
    ↪ 0.00000000E+00
 .
 .
 .
 33 46 7.31034576E-03 4.12660994E-07 8.28253504E-03 1.21549249E-03
    ↪   9.48128015E-04
```

```
33 47 8.19851642E-03 2.69320818E-07 3.24614389E-07
 $END


--- OPTIMIZED UHF MO-S --- GENERATED AT 21:50:42 01-FEB-2022
E= -747.2765866003, E(NUC)= 243.8806032204
 $VEC2
 1 1-4.11279627E-01-6.54756313E-01-1.27735296E-02 2.83662108E
    ↪ -03-1.73072167E-03
 1 2 2.73094870E-07 3.34552677E-05-3.77625429E-05 3.18547064E-04
    ↪ 2.10188501E-05
 .
 .
 .
33 46-4.82550045E-03-8.40678914E-03-9.76058182E-03-7.02615240E
    ↪ -03-3.32792816E-03
33 47-8.26337572E-03-3.67878343E-03-4.83173137E-03
 $END
```

Listing 4.7 displays the input for the MECP Hessian calculation for the SO_2F_2 singlet-triplet seam. The data from both the singlet and triplet Hessian calculations are to be used in the NAST *effhess* tool, which is explained in section 4.4.1. These data are automatically output by GAMESS in the associated `*.dat` files. The *effhess* calculation will compute the effective Hessian at the MECP, and a total of seven 0 frequencies are expected; otherwise, the MECP calculation is only within the vicinity of the true MECP and the search should be recomputed.

Listing 4.7: GAMESS input file format for MECP singlet-triplet Hessian calculations.

```
$contrl scftyp=uhf mplevl=2 runtyp=hessian
icharg=0 mult=3 ispher=-1 maxit=200 $end
$system mwords=2000 $end
$scf dirscf=.t. SOSCF=.F. DIIS=.T. shift=.t. damp=.t. $end
$statpt hssend=.t. nstep=400 $end
$basis gbasis=N311 ngauss=6 ndfunc=3
nffunc=1 diffsp=.true. $end
$guess guess=moread norb=233 $end
$DATA
SO2F2
C1
 S 16.0 0.2236491721 0.1065933096 -0.1522642640
 O 8.0 0.7051404450 -1.2143762680 0.8395308017
 O 8.0 -0.6420560198 0.5980384717 0.8709456546
 F 9.0 0.2259008590 1.3276612075 -1.2331762462
 F 9.0 -0.5126344821 -0.8179926930 -1.1781560376
 $END

 --- OPEN SHELL ORBITALS --- GENERATED AT 01:06:59 02-FEB-2022
 SO2F2
E(UHF)= -746.1095777393, E(NUC)= 274.7646477275, 6 ITERS
 $VEC
 1 1 4.11288188E-01 6.54749608E-01 1.27515975E-02-2.81735333E-03
    ↪ 1.77282006E-03
 1 2 1.29085520E-04-1.93079544E-04-2.35663330E-05-7.79854608E
    ↪ -05-1.36078530E-04
 .
 .
 .
 33 46 1.01366977E-02 4.93325631E-03 5.62412828E-03 5.14842606E-03
    ↪ 7.51223612E-03
 33 47 6.05373948E-03 7.57198004E-03 4.63653901E-03
```

```
$END
```

In order to calculate the spin-orbit coupling, a complete active space self-consistent field (CASSCF) calculation needs to be performed in order to obtain the state-averaged wavefunctions over the singlet and triplet states. The CASSCF input is displayed in listing 4.8.

Listing 4.8: GAMESS input file format for MECP state-averaged CASSCF/MC-QDPT calculations.

```
$contrl runtyp=energy icharg=0 scftyp=mcscf ispher=-1 mplevl=2
    ↪ $end
$system mwords=2000 memddi=5000 $end
$guess guess=moread norb=233 $end
$det ncore=24 nact=2 nels=2 nstate=2 wstate(1)=1,1 pures=.f. $end
$scf dirscf=.t. soscf=.f. diis=.t. shift=.t. damp=.t. $end
$mcscf fullnr=.t. maxit=100 $end
$trans dirtrf=.t. $end
$basis gbasis=N311 ngauss=6 ndfunc=3
nffunc=1 diffsp=.true. $END
$DATA
SO2F2
C1
 S 16.0 0.2236311484 0.1065339496 -0.1523123307
 O 8.0 0.7051037680 -1.2143299533 0.8395692450
 O 8.0 -0.6420314663 0.5979835931 0.8709248858
 F 9.0 0.2261332055 1.3276931912 -1.2331278477
 F 9.0 -0.5128366816 -0.8179567527 -1.1781740438
 $END

--------------- MEX SEARCH NSERCH= 97 ---SECOND STATE
    ↪ ---------------
--- OPEN SHELL ORBITALS --- GENERATED AT 01:06:59 02-FEB-2022
 SO2F2
E(UHF)= -746.1095777393, E(NUC)= 274.7646477275, 6 ITERS
 $VEC
 1 1 4.11288188E-01 6.54749608E-01 1.27515975E-02-2.81735333E-03
    ↪ 1.77282006E-03
 1 2 1.29085520E-04-1.93079544E-04-2.35663330E-05-7.79854608E
    ↪ -05-1.36078530E-04
 .
 .
 .
 33 46 1.01366977E-02 4.93325631E-03 5.62412828E-03 5.14842606E-03
    ↪ 7.51223612E-03
```

```
33 47 6.05373948E-03 7.57198004E-03 4.63653901E-03
 $END
```

Once the orbitals are obtained from the CASSCF calculation, they are used as the input guess for the spin-orbit coupling calculation. The input for the SOC calculation is displayed in listing 4.9. Here, a multi-configurational quasi-degenerate pertubration theory (MCQDPT) calculation is performed to compute the SOC given the use of the *MP2/6-311+G(3df)* level of theory for all previous computations, which allows for some increased accuracy in the calculation.

Listing 4.9: GAMESS input file format for MECP spin-orbit coupling (SOC) calculations.

```
$system mwords=2000 $end
$contrl runtyp=transitn icharg=0 scftyp=none
ispher=-1 mplevl=2 $END
$mrmp mrpt=mcqdpt rdvecs=.t. $end
$mcqd1 istsym=1 nstate=1 mult=1 iforb=1
 nmofzc=0 nmodoc=24 nmoact=2 $end
$mcqd2 istsym=1 nstate=1 mult=3 iforb=1
 nmofzc=0 nmodoc=24 nmoact=2 $end
$transt operat=hso2 numci=2 numvec=-2
 iroots(1)=1,1 nfzc=24 nocc=26 $END
$basis gbasis=N311 ngauss=6 ndfunc=3
nffunc=1 diffsp=.true. $END
$guess guess=moread norb=233 $end
$DATA
SO2F2
C1
 S 16.0 0.2236311484 0.1065339496 -0.1523123307
 O 8.0 0.7051037680 -1.2143299533 0.8395692450
 O 8.0 -0.6420314663 0.5979835931 0.8709248858
 F 9.0 0.2261332055 1.3276931912 -1.2331278477
 F 9.0 -0.5128366816 -0.8179567527 -1.1781740438
 $END

 --- OPTIMIZED MCSCF MO-S --- GENERATED AT 12:30:21 03-FEB-2022
 SO2F2
E(MCSCF)= -746.0858387149, E(NUC)= 274.7642774552
 $VEC1
 1 1 4.11283640E-01 6.54758270E-01 1.27344784E-02-2.80891172E-03
    ↪ 1.79520882E-03
 1 2 1.64447552E-04-1.17633163E-04-3.49605874E-05-8.69567845E
    ↪ -05-7.60800170E-05
 .
```

```
      .
      .
33 46 1.01377773E-02 4.93505650E-03 5.62676997E-03 5.14952469E-03
    ↪ 7.51224840E-03
33 47 6.05553672E-03 7.57195558E-03 4.63794877E-03
 $END
```

With this calculation procedure outlined, a successful MECP geometry and its associated quantities may be computed and used for the computation of a spin-diabatic rate coefficient across the seam of two potential energy surfaces via the NAST package [29, 30, 55]. The procedure and inputs for the NAST computations are outlined in sections 3.4 and 4.4.1.

4.3 Automated Reaction Kinetics and Network Exploration (Arkane) Code

The Arkane code is a part of the Reaction Mechanism Generator (RMG) software package [28] developed by Professor William H. Green's group in MIT's Department of Chemical Engineering. Arkane is a software tool used for computing the thermodynamic properties of chemical species as well as the high-pressure-limit rate coefficients for chemical reactions. The thermodynamic property calculations are computed using the rigid rotor and harmonic oscillator approximations, with the option to correct for hindered internal rotors. The reaction rate coefficients are calculated via CTST with the option to correct for quantum tunneling effects, such as with the Eckart potential model [50]. The input for these calculations are taken from the quantum chemistry calculations as previously discussed in sections 4.2 and 4.2.1.

For unimolecular reaction neworks of arbitrary complexity (e.g. multiple well-skipping events), Arkane also estimates the pressure-dependent phenomenological rate coefficients $k(T, P)$ via the use of a one-dimensional master equation. Several model reduction methods are available to simplify this detailed master equation model into a set of phenomenological rate coefficients. The outline of the basic theory behind these computations has been outlined in section 3.3. These reactions rates may then

be employed in SANS or any other suitably modifiable CFD code.

For a more comprehensive discussion of Arkane and the RMG software package, please see: `https://rmg.mit.edu/`.

4.3.1 Arkane Input for CTST Reactions

The Arkane program input file for the individual, high-pressure limit rate coefficient CTST reactions at the *MP2/cc-pvtz* level of theory is displayed in listing 4.10. Several features are included in the file. Hindered rotor approximations are not used as there are no molecules with rotor geometries in this work. The use of atom energy corrections have been used, but bond additivity corrections have not been used. The quantum chemistry inputs are handled by the `species()` and `transitionState()` objects. The `reaction()` objects take these objects, and are then passed along to the `kinetics()` objects where the rate calculations and curve-fitting procedures are performed.

Listing 4.10: Arkane input file.

```python
#!/usr/bin/env python
# -*- coding: utf-8 -*-

modelChemistry = "MP2/cc-pvtz//MP2/cc-pvtz"

useHinderedRotors = False
useAtomCorrections = True
useBondCorrections = False

# MP2/cc-pvtz species
species('F', 'species/F/F.py',
        structure=SMILES('[F]'))
species('F2', 'species/F2/F2.py',
        structure=SMILES('FF'))
species('FO', 'species/FO/FO.py',
        structure=SMILES('[O]F'))
.
.
.

# MP2/cc-pvtz TSs
```

110

```
transitionState('F+NO_TS', 'TSs/F+NO=NOF/TS.py')
transitionState('NF2+N_TS', 'TSs/NF2+N=NF+NF/TS.py')
transitionState('NF2+O_TS', 'TSs/NF2+O=NF+OF/TS.py')
.
.
.


# MP2/cc-pvtz reactions
reaction(
    label = 'F + NO <=> NOF',
    reactants = ['F', 'NO'],
    products = ['NOF'],
    transitionState = 'F+NO_TS',
)
reaction(
    label = 'NF2 + N <=> NF + NF',
    reactants = ['NF2', 'N'],
    products = ['NF', 'NF'],
    transitionState = 'NF2+N_TS'
)
reaction(
    label = 'NF2 + O <=> NF + FO',
    reactants = ['NF2', 'O'],
    products = ['NF', 'FO'],
    transitionState = 'NF2+O_TS'
)
.
.
.


# kinetic calculations for MP2/cc-pvtz reactions
kinetics(
    label = 'F + NO <=> NOF',
    Tmin = (300,'K'), Tmax = (6000,'K'), Tcount = 60,
    )
kinetics(
    label = 'NF2 + N <=> NF + NF',
    Tmin = (300,'K'), Tmax = (6000,'K'), Tcount = 60,
    )
kinetics(
    label = 'NF2 + O <=> NF + FO',
    Tmin = (300,'K'), Tmax = (6000,'K'), Tcount = 60,
    )
.
.
```

.

The pressure-dependent network input file is displayed in listing 4.11. The input file is similar to the CTST input file, but with the addition of the pressure dependent handlings. The `network()` object is used to define the chemical network being examined, and the `pressureDependence()` object is used to define the settings for the computation.

Listing 4.11: Arkane pressure-dependent network input file.

```python
#!/usr/bin/env python
# -*- coding: utf-8 -*-

modelChemistry = "MP2/cc-pvtz//MP2/cc-pvtz"

useHinderedRotors = False
useAtomCorrections = True
useBondCorrections = False

# MP2/cc-pvtz species
species('N', 'species/N/N.py',
      structure=SMILES('[N]'))
species('N2', 'species/N2/N2.py',
      structure=SMILES('N#N'))
species('NO', 'species/NO/NO.py',
      structure=SMILES('[N]=O'))
species('NSO', 'species/NSO/NSO.py',
      structure=SMILES('N(=O)[S]'))
species('O', 'species/O/O.py',
      structure=SMILES('[O]'))
species('OSN', 'species/OSN/OSN.py',
      structure=SMILES('[S]-O-[N]'))
species('S', 'species/S/S.py',
      structure=SMILES('[S]'))
species('SN', 'species/SN/SN.py',
      structure=SMILES('[N]=S'))
species('SO', 'species/SO/SO.py',
      structure=SMILES('O=S'))

# MP2/cc-pvtz TSs
transitionState('S+NO_TS', 'TSs/S+NO=SNO/TS.py')
transitionState('OSN_TS', 'TSs/S+NO=OSN/TS.py')
transitionState('SN+O_TS', 'TSs/SNO=SN+O/TS.py')
transitionState('SO+N_TS', 'TSs/OSN=SO+N/TS.py')
```

```
# MP2/cc-pvtz reactions
reaction(
        label = 'S␣+␣NO␣<=>␣NSO',
        reactants = ['S', 'NO'],
        products = ['NSO'],
        transitionState = 'S+NO_TS',
    )
reaction(
        label = 'NSO␣<=>␣SN␣+␣O',
        reactants = ['NSO'],
        products = ['SN', 'O'],
        transitionState = 'SN+O_TS',
    )
reaction(
        label = 'S␣+␣NO␣<=>␣OSN',
        reactants = ['S', 'NO'],
        products = ['OSN'],
        transitionState = 'OSN_TS',
    )
reaction(
        label = 'OSN␣<=>␣SO␣+␣N',
        reactants = ['OSN'],
        products = ['SO', 'N'],
        transitionState = 'SO+N_TS',
    )


# kinetic calculations for MP2/cc-pvtz reactions
kinetics(
    label = 'S␣+␣NO␣<=>␣NSO',
    Tmin = (300,'K'), Tmax = (6000,'K'), Tcount = 30,
    )
kinetics(
    label = 'NSO␣<=>␣SN␣+␣O',
    Tmin = (300,'K'), Tmax = (6000,'K'), Tcount = 30,
    )
kinetics(
    label = 'S␣+␣NO␣<=>␣OSN',
    Tmin = (300,'K'), Tmax = (6000,'K'), Tcount = 30,
    )
kinetics(
    label = 'OSN␣<=>␣SO␣+␣N',
    Tmin = (300,'K'), Tmax = (6000,'K'), Tcount = 30,
    )

network(
```

```
    label = 'S-NO',
    isomers = [
        'NSO', 'OSN',
    ],
    reactants = [
        ('S', 'NO'),
    ],
    bathGas = {
        'N2': 1.0,
    }
)

pressureDependence(
    label='S-NO',
    Tmin=(500.0,'K'), Tmax=(6000.0,'K'), Tcount=20,
    Pmin=(0.00001,'bar'), Pmax=(1000.0,'bar'), Pcount=9,
    maximumGrainSize = (1.0,'kcal/mol'),
    minimumGrainCount = 250,
    method = 'modified␣strong␣collision',
    interpolationModel = ('pdeparrhenius'),
)
```

4.4   Non-Adiabatic Statistical Theory (NAST) Code

The NAST package [29, 30] allows for the predicting of kinetics for electron spin-
dependent processes, including intersystem crossings, spin-forbidden reactions, and
spin crossovers. Namely, it can describe the kinetics of *nonradiative* electronic state
transitions between states with differing spin multiplicities at the MECP on the cross-
ing seam of coupled PES's. NAST calculates the probabilities and rates of transitions
between electronic excited states, as well as the microcanonical and canonical (en-
ergy and temperature dependent, respectively) rate coefficients that may be used in
kinetic computations. The ability to account for quantum effects such as tunnel-
ing, zero-point vibrational energy, and reaction path inteference are available. The
NAST package can also be used for CTST computations in the limit of spin-adiabatic
reactions.

For a more comprehensive discussion of the theory behind NAST, the code, and

how to install and use NAST, please see: `https://github.com/svarganov/NAST`.

4.4.1   NAST Input for NA-TST Reactions involving MECP's

In order to compute the effective Hessian for the MECP, which is necessary for the probability of transition calculations, the input file for the SO_2F_2 example is shown below in listing 4.12. The file is simple to set up, which only instructs the tool to utilize the GAMESS output files as inputs for the tool to extract the data from and generate the necessary values for the actual rate calculation.

Listing 4.12: NAST *effhess* input file.

```
&programs
GAMESS = .true.
Molpro = .false.
&end

&gamess_input_files
low_spin_dat = 'hess/SO2F2_MECP_S_hess.dat'
high_spin_dat = 'hess/SO2F2_MECP_T_hess.dat'
input_geometry = 'hess/SO2F2_MECP_S_hess.inp'
&end
```

The input data shown below in listing 4.13 for the NAST code corresponds to the singlet-triplet reaction discussed in chapter 5. All values listed below are stored in an input file (*.inp) for use by the NAST code. It consists of the vibrational frequencies and rotational moments of inertia and energy changes for the reactant, MECP, and product. The max iteration counter for integration was set to 40,000 to ensure convergence has been achieved. The temperature range has been varied in increments of 100K from 300K to 6,000K. The MECP vibrational frequencies, rotational moments of inertia, reduced mass, and gradient quantities all come from the *effhess* program tool in the NAST package.

116

Listing 4.13: NAST input file.

```
&keys zpe=1 printmore=.true. rev=.true. &end

&inputdata
freX = 0 228 251 394 452 516 684 824 1312
inertX = 269.49673 419.64579 538.45322
freR = 39 40 66 365 385 518 720 789 1359
inertR = 254.32725 781.12036 890.05938
enX = 0.0196559
enR = 0.0
maxn = 40000
T1 = 300.0
T2 = 6000.0
Tstep = 100.0
&end

&probability
redmass = 20.39542
soc = 40.29
grad = 0.230132
gradmean = 0.092461
&end

&reverse
freP = 378 379 533 535 545 839 871 1289 1533
inertP = 355.98903 359.53668 360.94327
enP = -0.172992
&end
```

4.5   Cantera

This work uses the Cantera [73] open-source suite of chemical kinetics problem solving tools, particularly the 0D ideal gas reactor model. This ideal gas reactor model allows for the study of the time-evolution of the chemical reaction network and allow for the direct observation of chemical timescales, the results of which are shown and discussed in chapter 6. The input code for the ideal gas reactor model is shown in listing 4.14.

Listing 4.14: Cantera ideal gas reactor input file.

```python
"""
Constant-pressure, adiabatic kinetics simulation.

Requires: cantera >= 2.5.0, matplotlib >= 2.0
"""

from subprocess import run
import sys
import os
from pathlib import Path

import numpy as np
import cantera as ct

nreactions = 110

gas = ct.Solution('../AirSF6_NASA9.cti')
gas.TDX = 4000.0, 0.0036565461106277844, \
'N2:0.10203448556069693,' \
'O2:0.0021849727217522347,' \
'N:0.18466394264389,' \
'O:0.10134916396951706,' \
'NO:0.0023068454575029497,' \
'N2+:4.8583498577437394e-06,' \
'O2+:1.4475829024348895e-06,' \
'N+:2.4289171030368237e-05,' \
'O+:2.602836277512261e-05,' \
'NO+:9.089442143218459e-05,' \
'E:0.00014751788791861472,' \
'SF6:0.6071655538707244'
r = ct.IdealGasReactor(gas, name='Reactor')

sim = ct.ReactorNet([r])
sim.verbose = True

for i in range(0,nreactions,1):
    r.add_sensitivity_reaction(i)

# set the tolerances for the solution and for the sensitivity
    ↪ coefficients
sim.rtol = 1.0e-8
sim.atol = 1.0e-15
sim.rtol_sensitivity = 1.0e-7
```

```
sim.atol_sensitivity = 1.0e-7

# limit advance when temperature difference is exceeded
delta_T_max = 5.
r.set_advance_limit('temperature', delta_T_max)

dt_max = 1.e-5
t_end = 200 * dt_max

extrasList = ['t']
for i in range(0,nreactions,1):
    extrasList.append('s' + str(i))

states = ct.SolutionArray(gas, extra=extrasList)

print('{:10s} {:10s} {:10s} {:14s}'.format(
    't [s]', 'T [K]', 'P [Pa]', 'u [J/kg]'))
while sim.time < t_end:
    sim.advance(sim.time + dt_max)
    states.append(r.thermo.state, t=sim.time*1e3, **{extrasList[i
        ↪ +1]: sim.sensitivity('E', i) for i in range(0,nreactions
        ↪ ,1)})
    print('{:10.3e} {:10.3f} {:10.3f} {:14.6f}'.format(
            sim.time, r.T, r.thermo.P, r.thermo.u))
```

Chapter 5

Results and Analysis of *Ab-initio* Reaction Rates for air-SF$_6$ Plasma

5.1 CTST Reactions

The CTST reactions in this work have been carried out at the *MP2/cc-pvtz* or *MP2/6-311+G(3df)* levels of theory. The transition state of each reaction has been confirmed to be a valid transition state by both visualizing the imaginary frequencies associated eigenvectors and resulting nuclear motions and intrinsic reaction coordinate (IRC) calculations. The exploration of these reactions in this work are somewhat cursory in nature, as many hypothesized reactions were trialed and the successful ones analyzed for use in the kinetics modeling. Several of these reactions may still have possible transition states that have not been discovered yet. Also, more accurate methods, such as *CCSD(T)*, should be used to increase the accuracy of the thermodynamics of the reactants, transition states, and products participating in the reaction.

The reaction rate parameters as well as the controlling temperatures can be found in appendix B, table B.5. The associated transition state information, including the relative free energy changes and vibrational frequencies can be found in appendix C, table C.1. An example reaction will be explored, showing the process of inspecting the results.

5.1.1 Example reaction:

$NF_2 + N \longrightarrow NF + NF$

The reaction

$$NF_2 + N \longrightarrow NF + NF \tag{5.1}$$
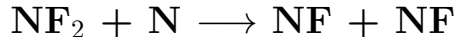
exists on a spin-quintet PES as sketched in figure 5-1, and has been fully calculated at the *MP2/cc-pvtz* level of theory. The change in the Gibbs free energy has been calculated relative to the reactants in the reaction. The resulting deltas are: $\Delta G^{\ddagger} = 253.2$ kJ/mol, and $\Delta G_p = -26.9$ kJ/mol. For these energies, no bond additivity corrections (BAC's) were used, but atom energy corrections (AEC's) have been applied. The imaginary frequency for the transition state is calculated to be 1186i cm^{-1} and the resulting nuclear motions are visualized in figure 5-2.
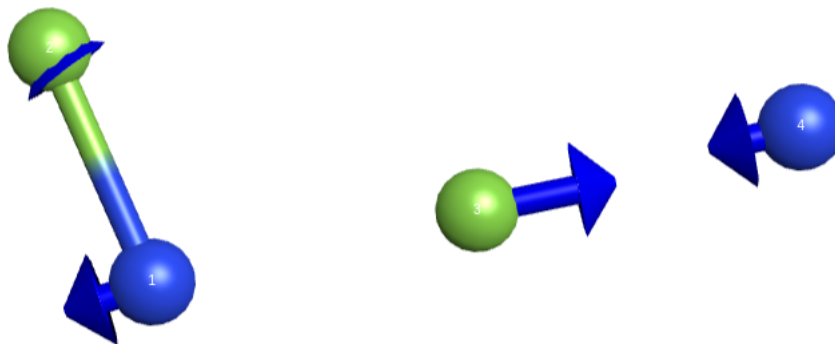
Figure 5-2: Eigenvector visualization of the $NF_2 + N \longrightarrow NF + NF$ reaction transition state. One fluorine of the NF$_2$ molecule dissociates to form a bond with the neighboring free-nitrogen atom (indicated by arrows).

The results of the IRC calculations can be seen in figures 5-3 and 5-4. The reactants and products are recovered from the minimization process using the initial transition state solution found in the transition state optimization calculation, clearly indicating that the transition state is indeed a valid transition state existing at a saddle point on the PES. From here, the calculation of the reaction rate coefficient
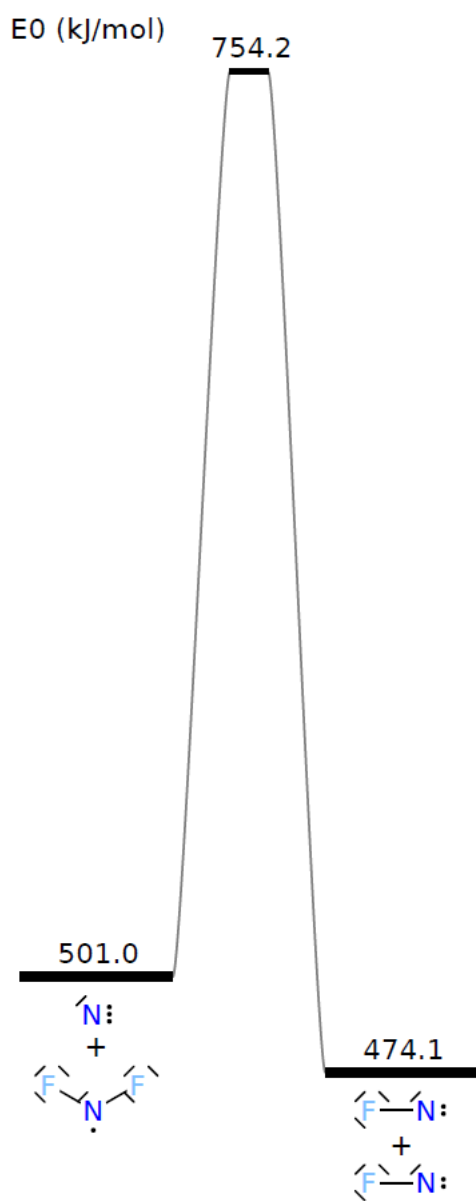
Figure 5-1: Potential energy surface for the $NF_2 + N \longrightarrow NF + NF$ reaction. AEC's are applied; however, BAC's are not applied.

using CTST is performed and the results curve-fit to a modified-Arrhenius rate form.
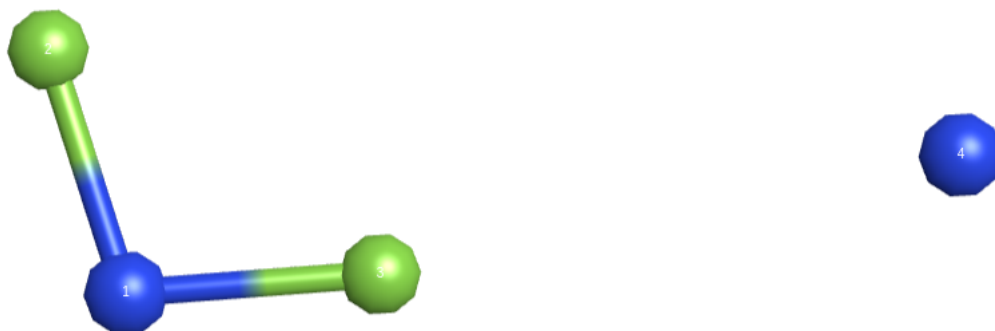
Figure 5-3: IRC calculation visualization of the $NF_2 + N \longrightarrow NF + NF$ reaction. Displayed are the reactants.

Figure 5-4: IRC calculation visualization of the $NF_2 + N \longrightarrow NF + NF$ reaction. Displayed are the products.

Figure 5-5 shows a plot of the results of the calculation. The linearity of the semilog plot of the rate coefficient versus the reciprocal temperature indicates that the curve-fit is accurately captured. The parameters for this fit (as well as the others) can be seen in the appendix, as mentioned previously.
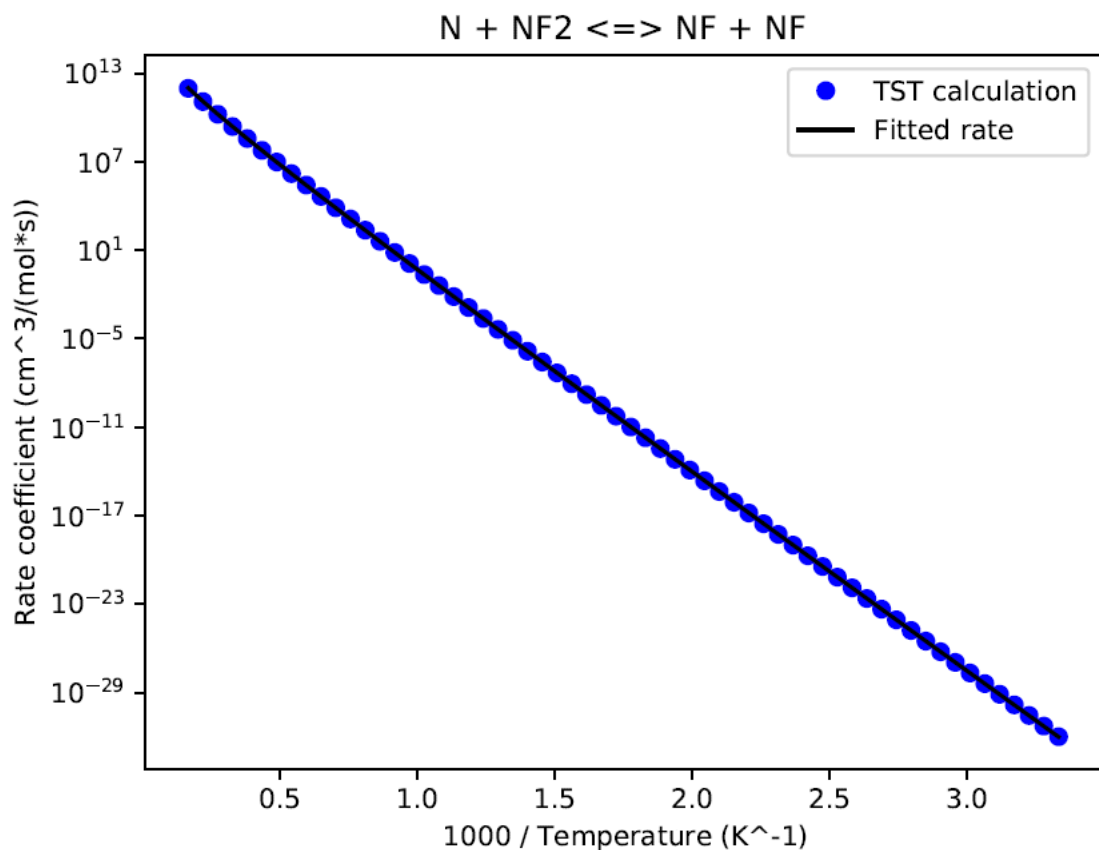
Figure 5-5: Semilog plot of the $NF_2 + N \longrightarrow NF + NF$ reaction rate coefficient as a function of the reciprocal temperature. The linearity indicates a reasonable calculation and modified-Arrhenius curve-fit result for the temperature range of 300K - 6000K. Results are listed in appendix B, table B.5.

5.2 Assessment of Importance of Pressure-Dependent Kinetics

5.2.1 S + NO $\longrightarrow$ OSN $\longrightarrow$ SO + N

As discussed in chapter 3, some chemical reaction rates are dependent on the pressure of the bath gas they take place in. This work examines two single-well multi-step reactions for pressure dependent effects, one of which is presented here for discussion:

$$S + NO \longrightarrow OSN \longrightarrow SO + N \tag{5.2}$$
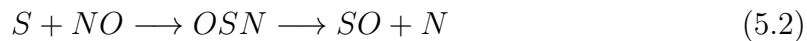
which takes place on a spin-quartet PES.

This single PES allows for the use of TST to estimate the rates of the individual step reactions, and the solution of the energy-grained master equation using the MSC method. The temperature range of 500K-6,000K and the pressure range of 10^{-5} - 10^3 bar have been explored. The results of the analysis are shown in figures 5-6, 5-7, and 5-8.

The results of the first step of the reaction,

$$S + NO \longrightarrow OSN \tag{5.3}$$

is seen in figure 5-6. The reaction clearly takes place in the low-pressure regime where there is a linear scaling with bath gas pressure. However, for lower temperatures at high pressures, we start to see the "knee" region of pressure-dependence forming. Higher temperatures will start to see the same effect at even higher pressures, of which are already well-beyond what an external hypersonic re-entry flow environment would typically see.
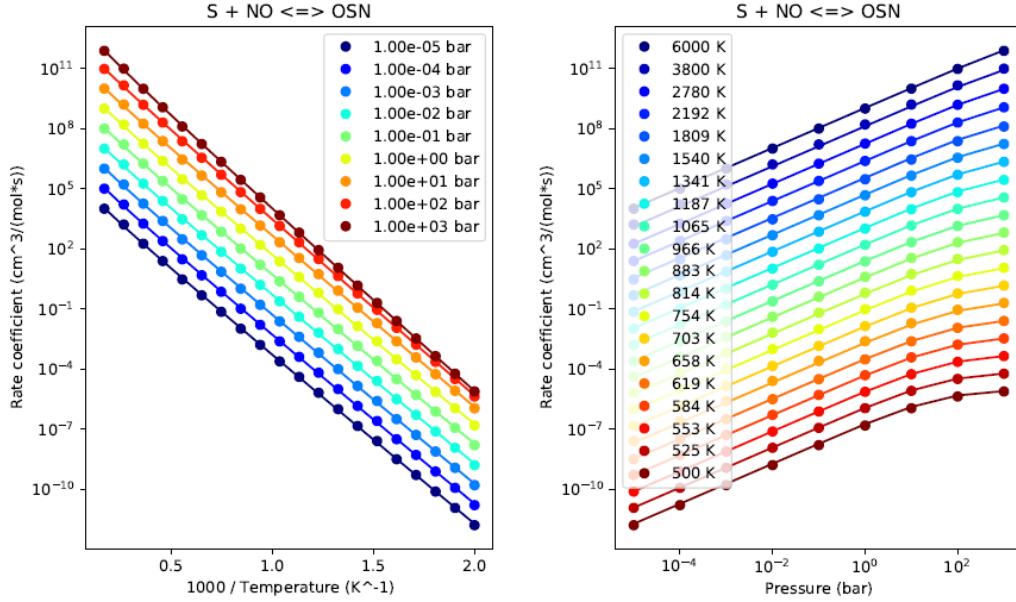
Figure 5-6: Results for reaction 5.3 indicating that its rate coefficient exists in the low-pressure limit. There is a slight "knee" region forming at lower temperatures at pressures of around 1,000 bar.

The results of the second step of the reaction,

$$OSN \longrightarrow SO + N \tag{5.4}$$

is seen in figure 5-7. Similar to reaction (5.3), the reaction exists in the low-pressure limit, although here no "knee" region is observed (not to say that one does not exist at higher pressures). It is clear that for unimolecular reactions with low internal degrees of freedom that are typically observed in hypersonic flow environments take place in the low-pressure limit.
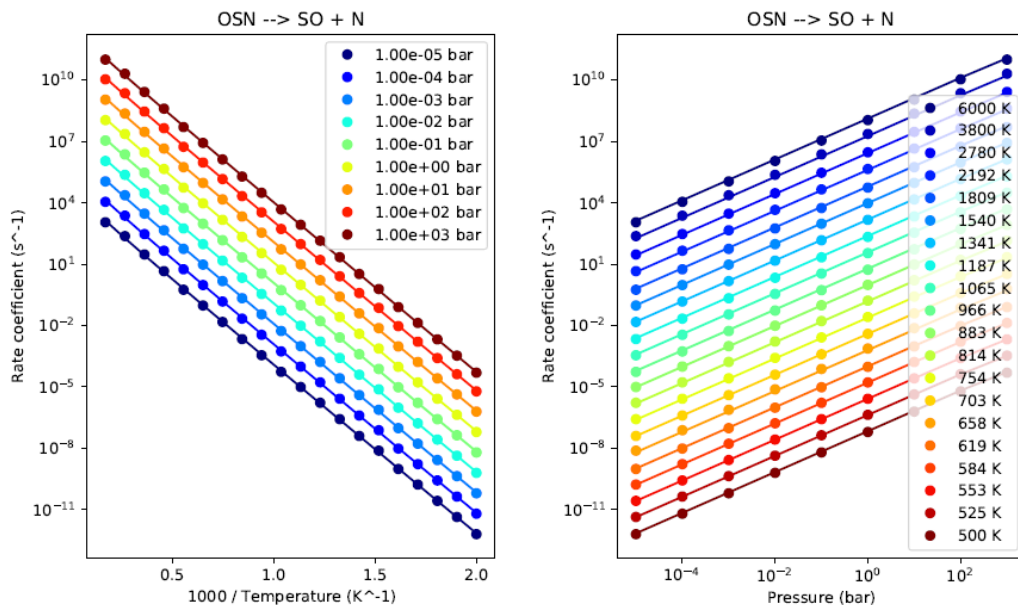
Figure 5-7: Results for reaction 5.4 indicating that its rate coefficient exists in the low-pressure limit. For this reaction, there happens to be no "knee" region forming at any temperature or pressure explored.

However, for the well-skipping portion of the reaction,

$$S + NO \longrightarrow SO + N \tag{5.5}$$

where the reactants skip over the unimolecular reaction intermediate OSN, the resulting reaction is independent of the pressure and is only a function of the temperature, as seen in figure 5-8. Such a result is expected as the collisions from bath gas molecules thermally deactivate the excited OSN^* unimolecular complexes into the energy well. The rate of passage through the transition state (over the energy barrier) of the S and NO reactants does not depend on the pressure. Thus, the resulting energy distribution of the passing population (calculated via its temperature) determines how many activated OSN^* complexes simply skip the OSN energy well and go straight to the SO and N products.
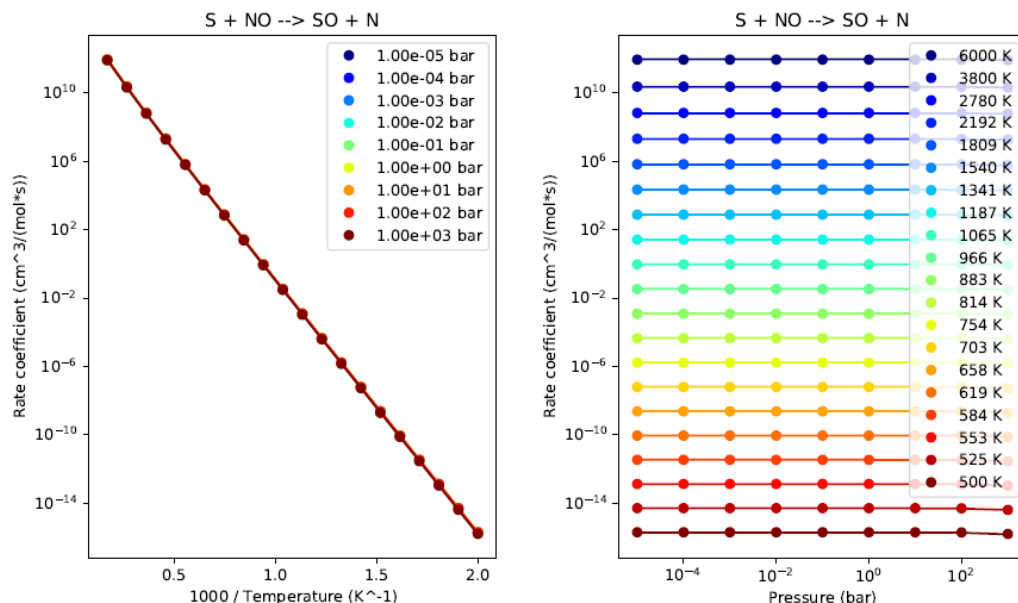
Figure 5-8: Results for the well-skipping reaction 5.5, verifying the suspected pressure-independent nature of the single-well, well-skipping reaction rate coefficient.

These results clearly support the need to inspect reactions for pressure dependencies, particular for those involving unimolecular isomerization, dissociation, or recombination, particularly for such reactions existing on a single PES.

5.3   NAST/MECP Reactions

5.3.1   Reaction of singlet-triplet system:

$$\textbf{SO}_2\textbf{F}_2 \xrightarrow{singlet-triplet} \textbf{SO}_2\textbf{F}_2 \xrightarrow{triplet} \textbf{SOF}_2 + \textbf{O}$$

The reaction

$$SO_2F_2 \xrightarrow{singlet-triplet} SO_2F_2 \xrightarrow{triplet} SOF_2 + O \tag{5.6}$$

is a reaction that occurs across two PES's. In essence, the SO_2F_2 molecule likes to exist in the singlet ground state; however, its dissociation products generally do not. This reaction is studied at the *MP2/6-311+G(3df)* level of theory. A transition

129

state was found for the triplet portion of the reaction

$$SO_2F_2 \xrightarrow{triplet} SOF_2 + O \tag{5.7}$$

while no singlet or quintet transition states were found. However, the spin mismatch poses a problem for transition state theory in going from the reactants to the singlet ground state SO_2F_2 product, as transition state theory is only applicable for reactions taking place on a single PES. In order to appropriately handle this issue, a nonadiabatic transition state theory is used to bridge the gap from triplet SO_2F_2 to singlet SO_2F_2.

Reaction (5.7) is a suitable reaction for CTST, and so the reaction rate for it is found in the usual way. The changes in the Gibbs free energy have also been calculated relative to the reactants in the reaction. The resulting deltas are: $\Delta G^{\ddagger} = 452.1$ kJ/mol, and $\Delta G_p = 431.3$ kJ/mol. As done previously, no bond additivity corrections (BAC's) were used, but atom energy corrections (AEC's) have been applied. The imaginary frequency for the transition state is calculated to be 482.8636i cm^1 and the resulting nuclear motions are visualized in figure 5-9.

The reaction has been confirmed via IRC calculations, and the resulting geometries are visualized from the IRC calculations are shown in figures 5-10 and 5-11.
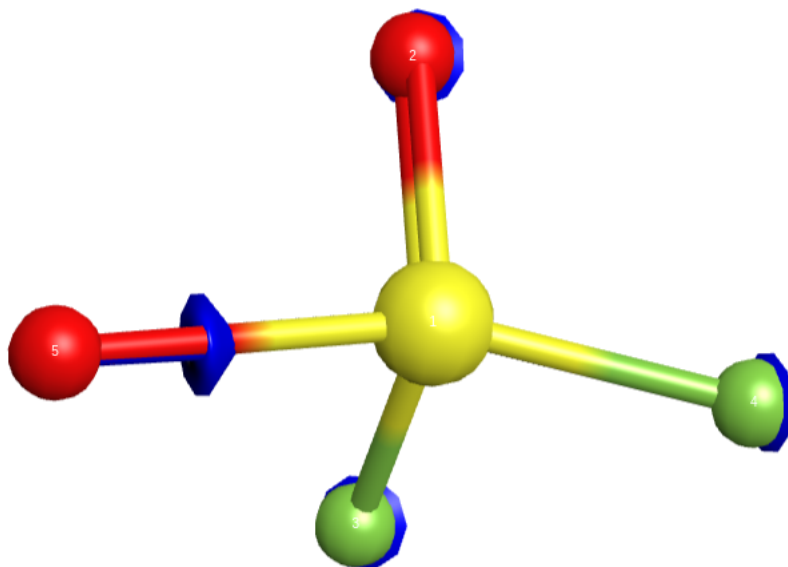
Figure 5-9: Eigenvector visualization of the $SO_2F_2 \xrightarrow{triplet} SOF_2 + O$ triplet transition state. The oxygen atom (#5) clearly shows a vibrational motion (versus a rotational motion) towards the central sulfur atom.
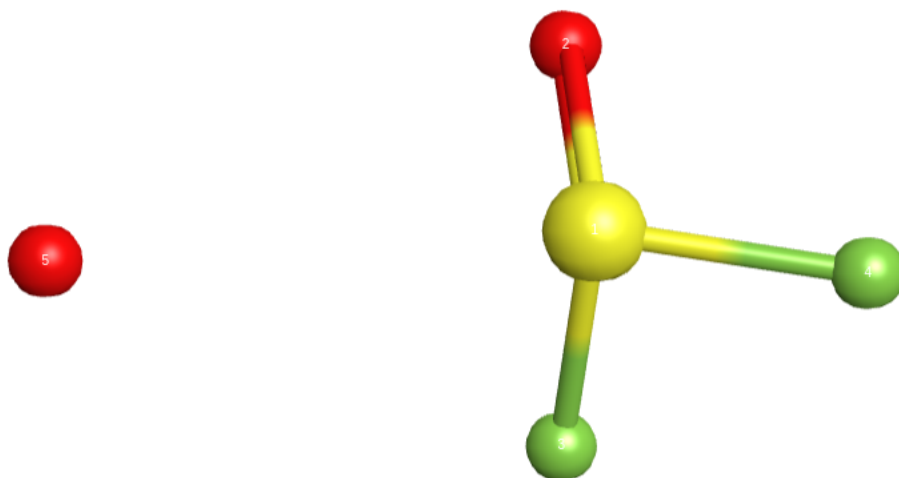
Figure 5-10: IRC calculation visualization of the $SO_2F_2 \xrightarrow{triplet} SOF_2 + O$ reaction. Displayed are the reactants.
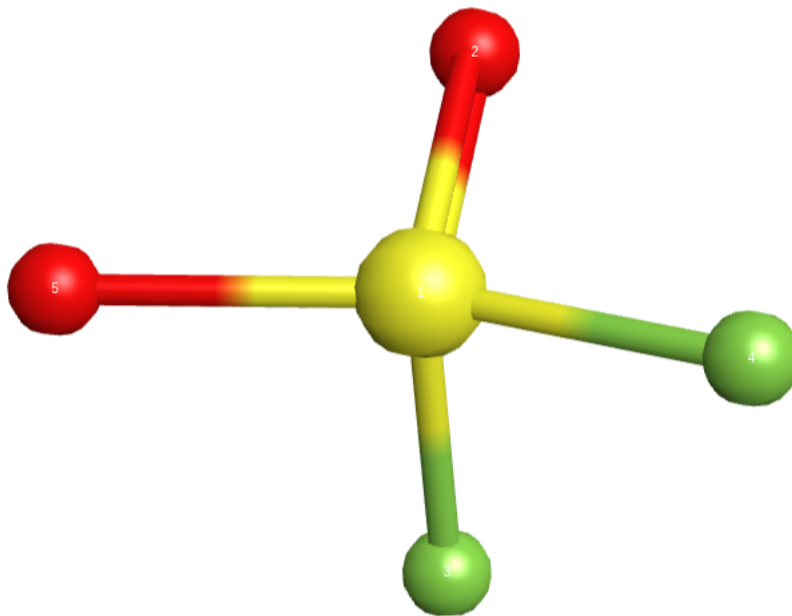
Figure 5-11: IRC calculation visualization of the $SO_2F_2 \xrightarrow{triplet} SOF_2 + O$ reaction. Displayed are the products.

The results from the CTST calculations for the rate coefficient are plotted in figure 5-12. The modified-Arrhenius parameters are valid for the temperature range of 300K - 6,000K and are as follows: $A = 4.979$ e07 s^{-1}, $\beta = 1.48$, and $E_a = 2,264$ K. These results conclude the CTST portion of the overall reaction. What remains is the NA-TST (NAST) portion of the singlet-triplet crossing.
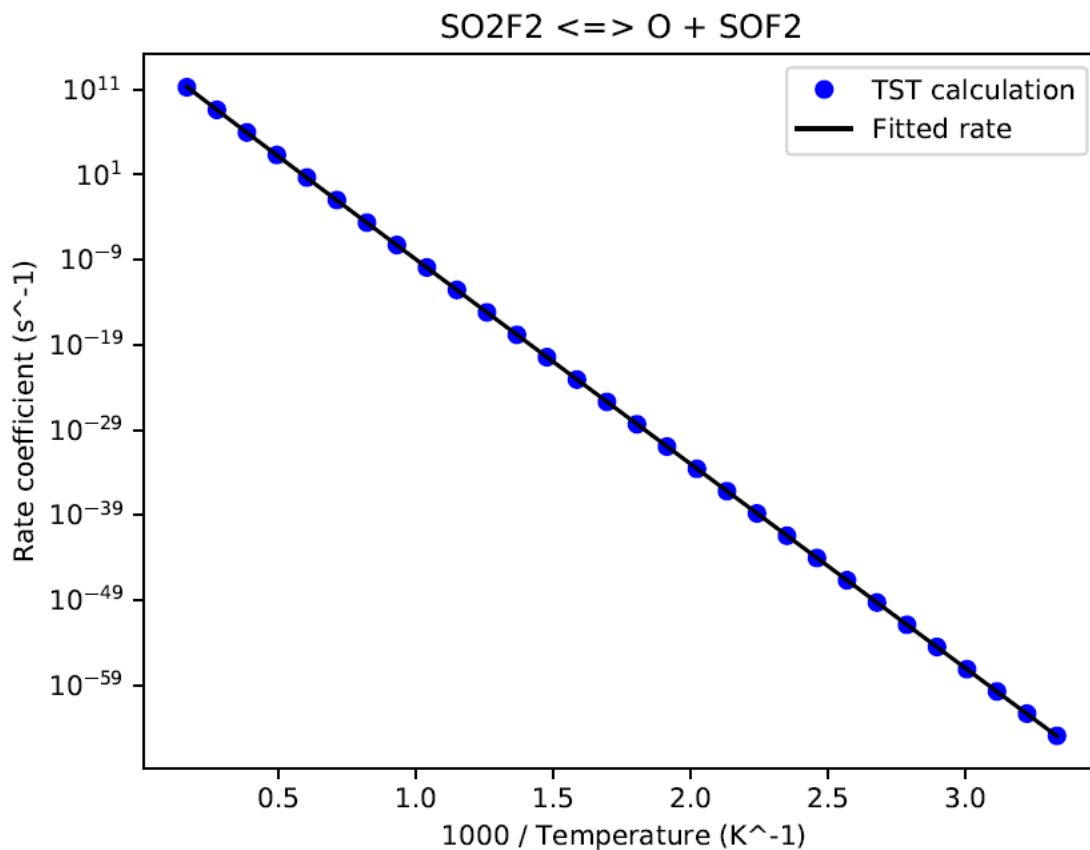
Figure 5-12: Semilog plot of the $SO_2F_2 \xrightarrow{triplet} SOF_2 + O$ reaction rate coefficient as a function of the reciprocal temperature. The rate parameters are valid for the temperature range of 300K - 6,000K are: $A = 4.979\ e07\ s^{-1}$, $\beta = 1.48$, and $E_a = 2,264$ K.

As described in chapter 3, a MECP geometry and its associated quantities are needed for the spin-forbidden triplet-singlet reaction

$$SO_2F_2 \xrightarrow{singlet-triplet} SO_2F_2 \qquad (5.8)$$
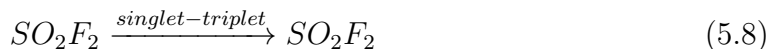
The overview of the inputs and procedure for running the necessary calculations, the descriptions of said calculations, and how to obtain the necessary quantities from the calculations have been described in section 4.2.2. The geometry for the MECP of reaction (5.8) is shown in figure 5-13.
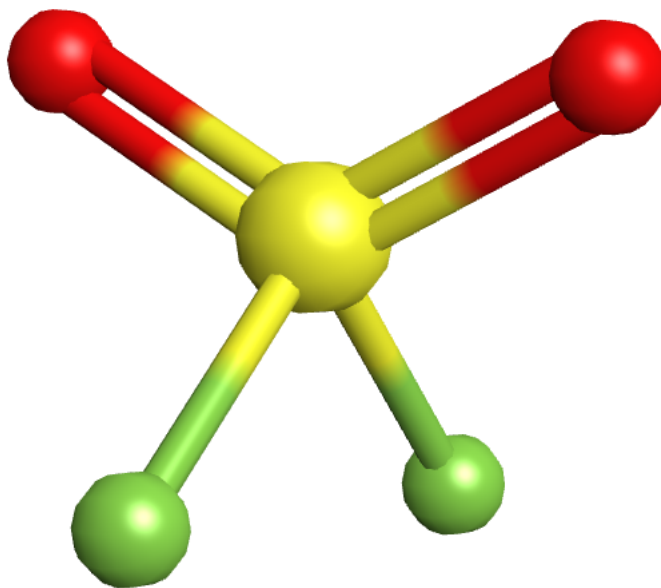
Figure 5-13: Visualization of the minimum energy crossing point geometry.

As before, the change in energies are relative to the reactant, which is the singlet SO_2F_2 in this case, and are $\Delta G_X = 51.607$ kJ/mol and $\Delta G_p = -454.190$ kJ/mol. The spin-orbit coupling is found to be $H_{SO} = 40.29$ cm^{-1}, the norm of the gradient $\|\Delta \vec{g}\| = 0.230132$, the mean of the gradient $\bar{g} = 0.092461$, and the reduced mass $\mu_\perp = 20.39542$. The rate coefficient parameters for the singlet-to-triplet step are $A = 1.036$ e10 s^{-1}, $\beta = 0.463$, and $E_a = 59,229$ K. The fitted rate can be seen plotted against the Landau-Zener probability rate data in figure 5-14 and is valid for a temperature range of 300K - 6,000K.
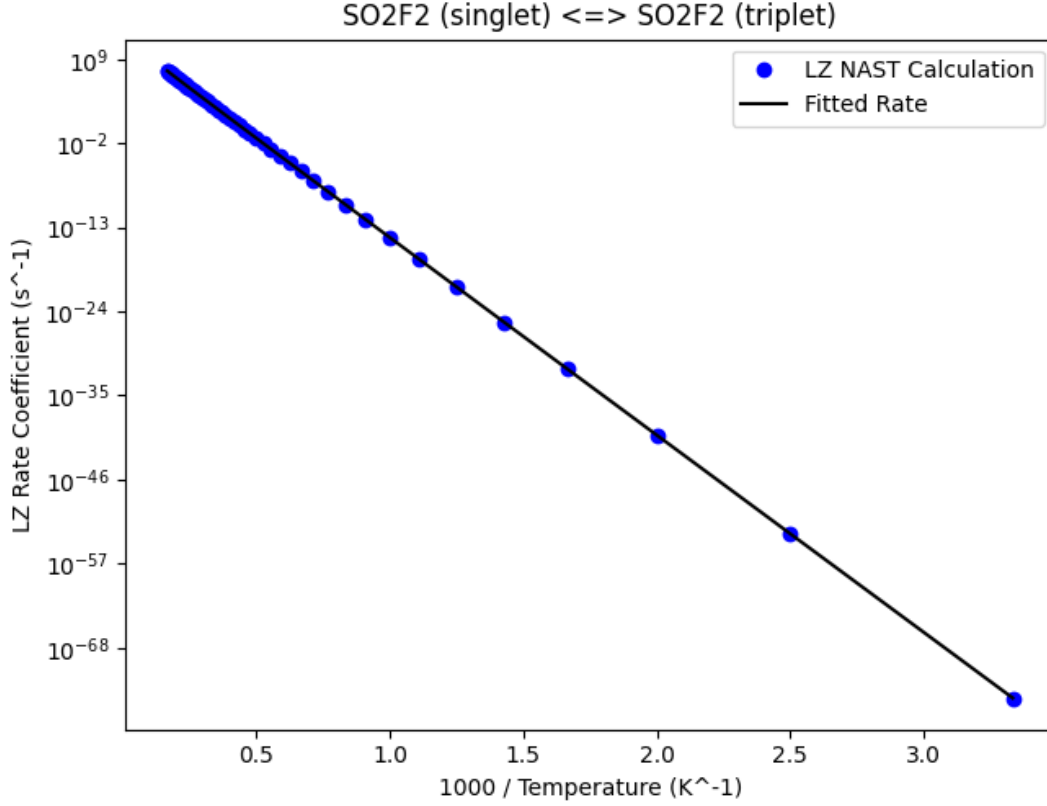
Figure 5-14: Semilog plot of the $SO_2F_2 \xrightarrow{singlet-triplet} SO_2F_2$ reaction rate coefficient as a function of the reciprocal temperature. The rate parameters are valid for the temperature range of 300K - 6,000K are: $A = 1.036 \text{ e}10 \text{ s}^{-1}$, $\beta = 0.463$, and $E_a = 59,229$ K.

In order to reduce this model to a suitable composite rate, an approximation is made regarding the CTST portion of the reaction, since $k_{CTST} \gg k_{NAST}$. It is assumed that the triplet SO_2F_2 is in a quasi-steady-state such that

$$\frac{d[(SO_2F_2)_t]}{dt} = k_{NAST}[(SO_2F_2)_s] - (k_{NAST}^{-1} + k_{CTST})[(SO_2F_2)_t] = 0 \qquad (5.9)$$

where k_{NAST}^{-1} is the reverse rate coefficient defined as $k_{NAST}^{-1} = k_{NAST}/K_{NAST}$, where K_{NAST} is the equilibrium constant for the NAST portion of the reaction. Using

this approximation, the overall rate of production of SOF_2 and O for this reaction becomes

$$\frac{d[SOF_2]}{dt} = \frac{d[O]}{dt} = k_{CTST}[(SO_2F_2)_t] - k_{CTST}^{-1}[SOF_2][O] \qquad (5.10)$$

indicating the effective forward rate for the overall reaction is

$$k_{eff} = \frac{k_{NAST}k_{CTST}}{\frac{k_{NAST}}{K_{NAST}} + k_{CTST}} = \frac{1}{\frac{1}{k_{CTST}K_{NAST}} + \frac{1}{k_{NAST}}} \qquad (5.11)$$

Clearly, if one step is rate determining, further approximations can be made to reduce it to the dominant rate for the overall reaction. However, if the MECP energy is lower than that of the reactant (i.e. barrierless), then the rate coefficient is simply a multiplication of the CTST rate and the probability of transition:

$$k_{eff}(T) = k_{CTST}(T)P_{NAST}(T) \qquad (5.12)$$

where $P_{NAST}(T)$ is the probability as a function of temperature as computed by the NAST program, depending on probability model selection.

This result gives us a fundamental way to calculate rate coefficients for spin-nonadiabatic reactions via ab-initio techniques. An approximate overall reaction rate for the reactions in order to help reduce the necessary number of species that must be simulated for the overall chemical kinetics model has also been presented. While lower-dimensional models (e.g. 0D batch reactors) are tractable for hundreds to thousands of species, higher-dimensional models (e.g. 2D TCNE flow computations) ought to utilize these techniques to improve computational runtimes.

5.4 Barrierless Radical Reactions

Several atom-atom radical reactions were considered in this work. Some of them were found to have valid transition states; however, a few were not and were found to be barrierless. For these reactions, diffusion-limited reactions rates were estimated to provide an upper-bound for their rates.

5.4.1 Diffusion-Limited Reaction Upper-Bound Estimates

For several of the radical reactions, namely

$$F + N \longrightarrow NF \tag{5.13}$$

$$F + O \longrightarrow OF \tag{5.14}$$

$$S + O \longrightarrow SO \tag{5.15}$$

$$S + N \longrightarrow SN \tag{5.16}$$

$$SN + O \xrightarrow{\text{doublet}} NSO \xrightarrow{\text{doublet}} S + NO \tag{5.17}$$
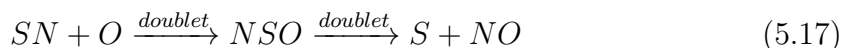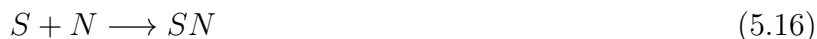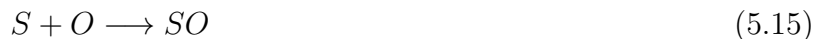
no valid transition states were found, indicating flat PES's along the reaction coordinate, making the TST approximation unsuitable. Thus, these reactions are assumed to be barrierless. It is assumed that once a collision occurs, the reactants will form products. An upper-bound reaction rate may be estimated using the collision frequency derived from kinetic theory arguments instead of TST. However, because the air-SF_6 plasma is a dilute gas mixture, the movement of particle species is instead dominated by diffusion processes. As such, a diffusion-limited rate coefficient is a more reasonable upper-bound approximation.

For uncharged reactants, the diffusion-limited rate coefficient takes on the form of [74]:

$$k_D = 4\pi \left(D_A + D_B \right) \left(r_A + r_B \right) \tag{5.18}$$

when using a simple spherical particle model. This model allows us to relate the diffusion coefficient to the viscosity of the dilute gas mixture via the Einstein-Stokes relation

$$D_s = \frac{k_b T}{6\pi r_s \eta(T)} \tag{5.19}$$

Upon substitution of equation (5.19) into equation (5.18), the diffusion-limited rate

coefficient is expressed as

$$k_D = \frac{2k_bT\left(r_A + r_B\right)^2}{3\eta(T)r_A r_B} \tag{5.20}$$

For the system being studied, namely that of a weakly-ionized reentry plasma, suitable order-of-magnitude estimates for the temperature and viscosity may be chosen. The temperature in the expanding flow region past the shoulder of a capsule experiencing plasma blackout is taken as approximately 1,000 K. A reasonable mixture viscosity estimate, when considering the multi-component results of Palmer and Wright [41] and the viscosity data of Murphy and Arundell [47] and Murphy [48], is 0.001 g cm^{-1} s^{-1} (as replicated in Figure 2-2).

The radii of the compounds associated with reactions (5.13) - (5.17) are listed in table 5.1.

Table 5.1: Radii for diffusion-limited rate coefficients.

Compound	Radius [pm]
N	65
O	60
F	50
S	100
NO	200
SN	230
NSO	250

Utilizing these assumptions, for reaction (5.13), the diffusion-limited rate for this reaction is

$$k_{D,F+O} = 2.25 * 10^{14} \text{ cm}^3 \text{ mol}^{-1} \text{ s}^{-1} \tag{5.21}$$

The resulting reaction rate information for reactions (5.13) - (5.17) can be found in appendix B, table B.5. The determination of the associated reverse reaction rate coefficients is accomplished through the use of the chemical equilibrium constant with its standard functional dependence on temperature.

Well-Skipping for Doublet S + NO $\xrightarrow{doublet}$ SN + O Reaction

The reaction

$$SN + O \longrightarrow NSO \longrightarrow S + NO \tag{5.22}$$

has also been studied in this work. It has been examined on a spin-quartet PES and was found to have valid transition states. However, the reaction (reaction (5.17)) can also take place on a spin-doublet PES, as the bonding electrons are permitted to have opposite spin states, and proceeds entirely energetically downhill. In order to handle this possible reactant configuration on the doublet PES, a search for the doublet transition states was conducted and produced no valid transition states as the PES region is markedly flat. Instead, a diffusion-limited rate coefficient is used to estimate the forward reaction rate coefficient in the high-pressure limit for the spin-doublet PES, and a composite rate coefficient for the overall bimolecular reaction is estimated via

$$k_{tot} = \frac{n_{s2}}{n_{s2} + n_{s4}} k_2 + \frac{n_{s4}}{n_{s2} + n_{s4}} k_4 = \frac{1}{3} k_2 + \frac{2}{3} k_4 \tag{5.23}$$

where k_2 and k_4 are the estimated rate coefficients for the spin-doublet and quartet PES's, respectively. Here, $n_{s2} = 2$ and $n_{s4} = 4$ are the number of possible combinations of electrons to produce the spin states for the doublet and quartet PES's, respectively. The composite rate coefficient for this reaction, k_{tot}, is curve-fit to the modified-Arrhenius format for use in this work.

5.5 Temperature and Pressure Ranges of Resulting Kinetic Model

The temperature range for the reactions studied in this work have been studied for a temperature range of 300K - 6,000K for all high-pressure rate constant data, and over a range of 500K - 6,000K for unimolecular reactions in order to aid in convergence

of the master equation solver. A higher temperature range may be explored within the theoretical framework of both CTST and NAST. However, given the exploratory nature of this work, it is strongly recommended that higher levels of theory are used, such as *CCSD(T)//MP2/6-311+G(3df)*, in order to improve the thermodynamic estimates of the quantum chemistry calculations. Also, some formulation of VTST may also prove useful in improving the upper-bound estimate of the rate coefficients in comparison with the CTST estimates.

The pressure range for the reactions presented in section 5.2 have been tested over a range of 1 Pa to 100 MPa using the modified strong collision (MSC) method for the energy grained master equation. The phenomenological rate coefficients produced by this method strongly support that the reactions involving a unimolecular reactant or product firmly operate in the low-pressure limit. However, the observed well-skipping phenomenon (here, where no unimolecular reaction intermediate is de-excited and stabilized) is independent of pressure over the temperature range of 300K - 6,000K, as expected. Given the results of the equilibrium analysis in the selection of species, utilizing the well-skipping reactions are suggested to be used in CFD-type applications to help minimize runtime costs accrued from large species counts, as the unimolecular products do not proceed as quickly as the well-skipping reactions in the pressure ranges that are typical of the hypersonic flow environment.

Chapter 6

Suflur Hexafluoride Injection into a Hypersonic Plasma Sheath Environment

Three models are presented in this chapter. The first is that of a 0D reactor, used to explicitly study the chemical timescales as functions of temperature, pressure, and initial concentration in an economical way. The second is that of a 1D TCNE multi-component Euler flow, providing an economical way to study the kinetics in the presence of advection. Lastly, a TCNE multi-component Euler 2D ARD simplified capsule geometry model is used to provide initial and/or inflow conditions for the first two models, as well as studying the affects of flow expansion on electron quenching. All model results will be examined and compared through the lens of the Damköhler number.

6.1 Sizing of a SF_6 Injection System

In order to properly engineer an injection system, a few universal parameters must be considered. These parameters are used to determine the SF_6 state as it enters the plasma sheath, allowing for the determination of its feasibility for use in the electron quenching process.

6.1.1 Governing Parameters

Damköhler Number

The first parameter is that of the Damköhler number. It is the prime dimensionless quantity of interest for the engineering problem of alleviating the plasma blackout. The injector and distance between the injector and transmitter is set by the desired Damköhler number:

$$Da = \frac{\tau_{res}}{\tau_{chem}} = \frac{\kappa(T)L}{U} \tag{6.1}$$

where τ_{res} is the fluid residence timescale, τ_{chem} is the chemical kinetics timescale, $\kappa(T)$ is the chemical timescale of interest, L is the domain length, and U is the average flow velocity within the vicinity of the injector and transmitter. In order to find the domain length, L, one simply manipulates equation (6.1):

$$L = \frac{Da\ U}{\kappa(T)} \tag{6.2}$$

This formulation of the domain length allows for a direct observation and quantification by varying Damköhler numbers, varying injector inlet flow quantities, and from chemical reaction rate data.

Corrected Flow per Unit Area

The second key parameter is that of the corrected flow per unit area, a dimensionless quantity that governs the mass flow rate of a compressible gas. It is expressed as:

$$\frac{\dot{m}\sqrt{T_t R}}{A P_t \sqrt{\gamma}} = \frac{M}{\left(1 + \frac{\gamma-1}{2}M^2\right)^{\frac{1+\gamma}{2(1-\gamma)}}} \equiv D(M) \tag{6.3}$$

From here, one observes that the mass flow, $\dot{m}$, of an ideal gas in a streamtube is governed by its total temperature, T_t, and total pressure, P_t, its gas properties R and γ, and the area, A, of the streamtube. The ratio of these quantities is conveniently set by the Mach number, M. Equation (6.3) has a maximum at $M = 1$, thus supporting

two identical values for the LHS depending on if the flow is subsonic or supersonic, as seen in figure 6-1.
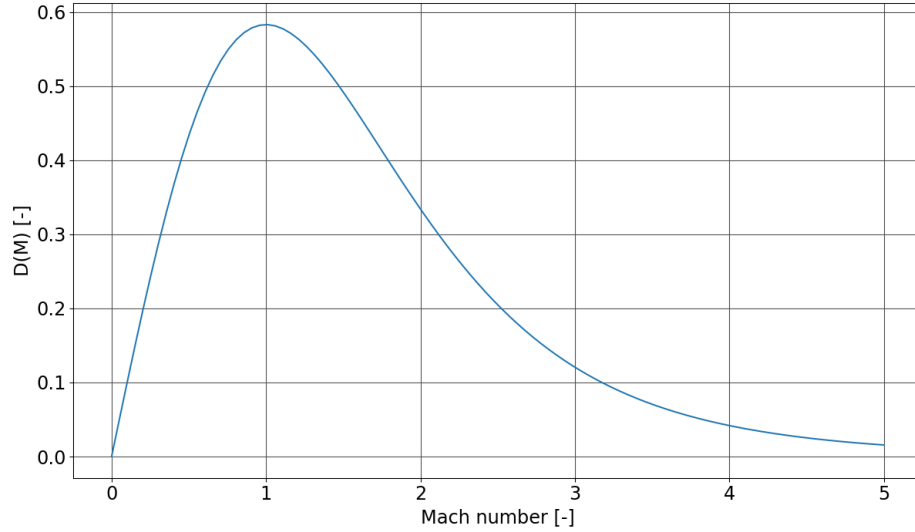
Figure 6-1: Function $D(M)$ versus Mach number for $\gamma = 1.33$.

Equation (6.3) will be utilized in solving for the density of the SF_6 that exits the injector.

Nozzle Area Ratio

The third key parameter for the system is the injector nozzle geometry, namely its area ratio. For this work, the area ratio will act merely as a sanity check for reasonable nozzle geometries (namely that the nozzle isn't exceedingly large). For a supersonic converging-diverging nozzle, it is also set by the mach number via:

$$\frac{A}{A^*} = \frac{1}{M} \left(\frac{2 + (\gamma - 1)M^2}{\gamma + 1} \right)^{\frac{\gamma+1}{2(\gamma-1)}} \tag{6.4}$$

where A^* is the nozzle throat area where the flow is choked and the throat Mach number, M^*, is unity. This equation can be easily derived by taking equation (6.3) at $M = M^* = 1$ and dividing it by itself as a general function of M (i.e. as stated above). Ignoring chemical reactions and changes in specific heats, all of equation (6.3)

143

LHS quantities, except for the flow area, are constant at any streamtube location for any Mach number.

Static Pressure at Injector Exit

In order to size the nozzle exit area, a static pressure must be decided. For a matched supersonic jet, the static pressure P should be equal to the static pressure of the external flow. One may also choose to under-expand the flow in order to mechanically displace the electrons as the jet expands further upon leaving the nozzle (it will be seen later why this choice might be worth considering in reality).

Once a static pressure is decided, the total pressure P_t for the SF_6 can be approximated via the isentropic flow relation:

$$P_t = P\left(1 + \frac{\gamma - 1}{2}M^2\right)^{\frac{\gamma}{\gamma - 1}} \tag{6.5}$$

where, as a reminder, γ is the ratio of specific heats for SF_6.

SF_6 Mole Fraction (Density)

The SF_6 mole fraction is unity at the exit of the nozzle by design. However, for a 0D reactor model, a mole fraction considered alongside the external flow environment must be calculated. In order to obtain the mole fraction, the density must be computed. The definition of mass flow for the SF_6 jet is given by

$$\dot{m}_{SF_6} = \rho_{SF_6}U_{SF_6}A_e \tag{6.6}$$

where A_e is the injector nozzle exit area. Rearranging for density gives:

$$\rho_{SF_6} = \frac{\dot{m}_{SF_6}}{U_{SF_6}A_e} \tag{6.7}$$

From here on out, the SF_6 subscript will be omitted for brevity. The velocity U can be determined via definition of exit Mach number and exit speed of sound (using SF_6 gas properties):

$$U = \left(M_e \sqrt{\gamma R T_e} \right) \tag{6.8}$$

where T_e is computed via the isentropic flow relation relating the SF$_6$ total temperature and exit Mach number to T_e. Substitution of equation (6.8) into equation (6.7) gives:

$$\rho = \frac{\dot{m}}{A_e} \frac{1}{M_e \sqrt{\gamma R T_e}} \tag{6.9}$$

The determination of $\dot{m}/A_e$ utilizes the corrected flow per unit area, and is found via:

$$\frac{\dot{m}}{A_e} = \frac{P_t \sqrt{\gamma}}{\sqrt{T_t R}} D(M_e) \tag{6.10}$$

and upon substitution gives, finally, for the density of SF$_6$ at the injector nozzle exit:

$$\rho = \frac{P_t \sqrt{\gamma}}{\sqrt{T_t R}} \frac{D(M_e)}{M_e \sqrt{\gamma R T_e}} \tag{6.11}$$

The determination of the mole fraction is straightforward. The molar concentration for a species s is found via

$$[s] = \frac{\rho_s}{M_s} \tag{6.12}$$

where M_s is the molar mass of species s. The mole fraction for a species s is then

$$X_s = \frac{[s]}{\sum_{s'} [s']} \tag{6.13}$$

The determination of all the key quantities of interest and the quantification method for the effectiveness of such a system have been presented. Several key parameters and their governance over the SF$_6$ fluid quantities of interest are outlined using a first-principles approach utilizing fundamental concepts with the assumption of isentropic nozzle flow.

While the mixing of the SF$_6$ jet and external flow will occur, the instantaneous

initial mole fractions are set due to conservation of mass and the supersonic nature of the SF_6 jet. The determination of the ionized air species are found via a model capsule problem, simulated in SANS, and will be explained in the following section. Afterwards, the 0D reactor problem for the assessment of the effectiveness of the SF_6 and air-plasma chemistry will be presented and assumptions outlined.

6.2   2D Expansion Flow

A simplified geometry of the ESA's Atmospheric Reentry Demonstrator (ARD) is used to generate a nominally 2D (non-axisymmetric) flow field. One can affectionately think of this capsule body as an extruded pizza slice, versus that of an axisymmetric capsule. Support for axisymmetric cases in SANS is not currently implemented, but is being actively worked on at the time of writing. However, this 2D case allows for a reasonable model flow field that can be used to study the electron quenching capabilities of SF_6.

An 11-species air baseline case will be examined. As previously mentioned, the geometry is a simplified version of the ARD capsule, the description of which can be found in section 2 of Takahashi et al [16]. The flight conditions for this case study correspond to the 75km point in the reentry trajectory, also given in the same Takahashi et al manuscript. The electron number density of the resulting flow field will be inspected to ensure that plasma blackout is occurring, namely, that the electron number density exceeds the critical plasma frequency for a S-band microwave signal. This plasma frequency is given by equation 1.1, which corresponds to an approximate electron number density of $n_{el} \sim 10^{-16}$.

6.2.1   11-Species Air Baseline Configuration Model

The free stream conditions for this baseline case are listed in Table 6.1. These conditions were selected with reference to the results of Takahashi et al [16] as their results indicated that the capsule was entirely blacked out at this particular simulated trajectory point.

146

Altitude [km]	u_∞ [m/s]	ρ_∞ [kg/m^3]	T_∞ [K]
75	7592	4.01E-5	201.7

Table 6.1: Free stream conditions for ARD simplified capsule geometry.

The 11-species air model used in this model has been developed by Park [36], the rates of which can be found in Appendix B. It is comprised of 27 reactions (51 when fully expanded for implementation). In this work, the preferential-dissociation reactions will retain their activation temperature formulation postulated by Park, where the activation temperature controlling those rates is $T_a = \sqrt{T_{tr}T_V}$. This formulation will allow for the modeling of the non-Boltzmann effects within the chemistry, even if only on an approximate basis.

Figure 6-2 shows the converged solution for the frequency bands of the transmitter that are blocked by the plasma sheath. This results shows that transmitters in the gigahertz range are expected to experience blackout at this point during re-entry, even with the transmitter located in the aft region of the vehicle where the flow is expanded and relatively cool in comparison to the windward region.
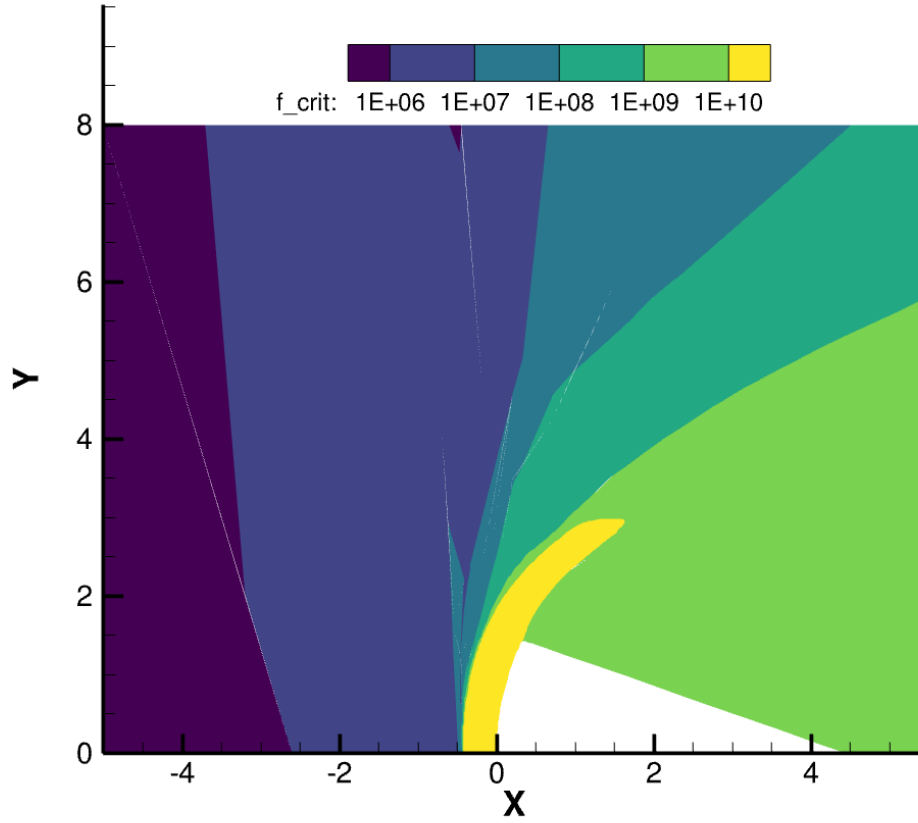
Figure 6-2: Critical frequency (in Hertz) corresponding to minimum transmitter signal required for signal penetration. As can be seen, the capsule is experiencing full plasma-blackout up through approximately 10 GHz.

Figure 6-3 shows the converged solution for the 11-species air baseline case. In comparison to the results of Takahashi et al [16], the TCNE multi-component Euler model shows reasonable agreement with the predicted number densities. As can be observed from the contours presented, plasma blackout will occur for gigahertz transmitters as regions of $n_{el} > 10^{16}$ encapsulate the entirety of the capsule body.
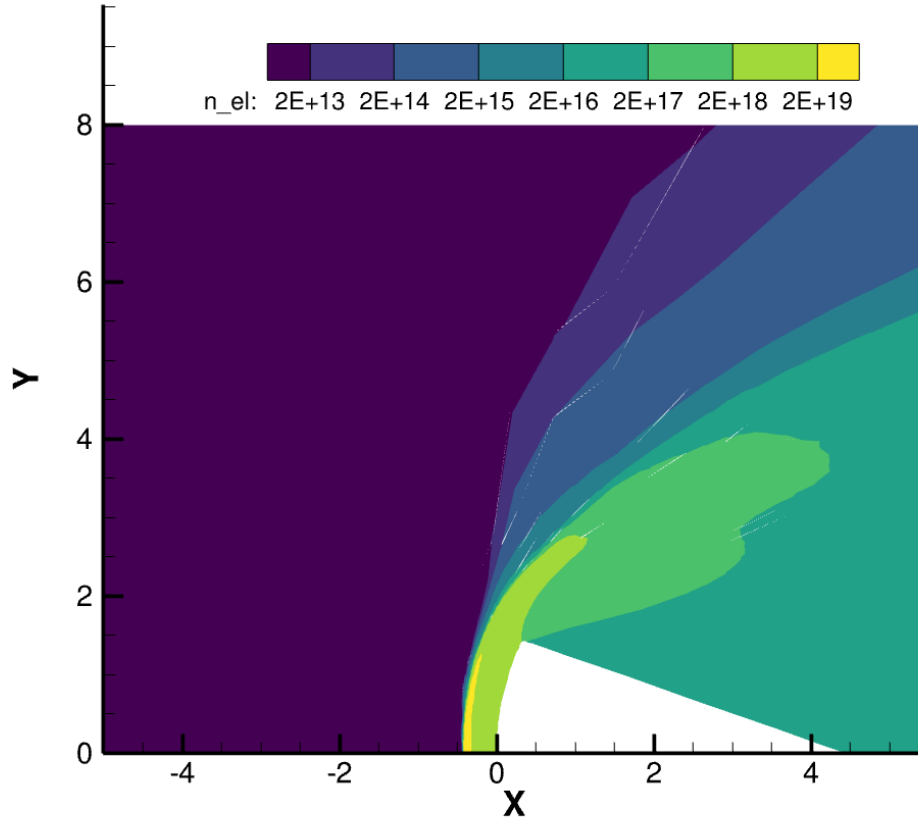
Figure 6-3: Electron number density contours for the 2D ARD simplified capsule geometry. As can be seen, the capsule is experiencing full plasma-blackout.

The case was ran with a DoF count of 2000 for polynomial order 1. Figure 6-4 shows the resulting adapted grid after 50 adaptation iterations. It has been adapted to the total enthalpy, as it should be conserved throughout the entirety of the domain because of the first law of thermodynamics. This also conveniently acts as a way to adapt for chemical compositions as the formation enthalpy of every species also is accounted for within the total enthalpy.
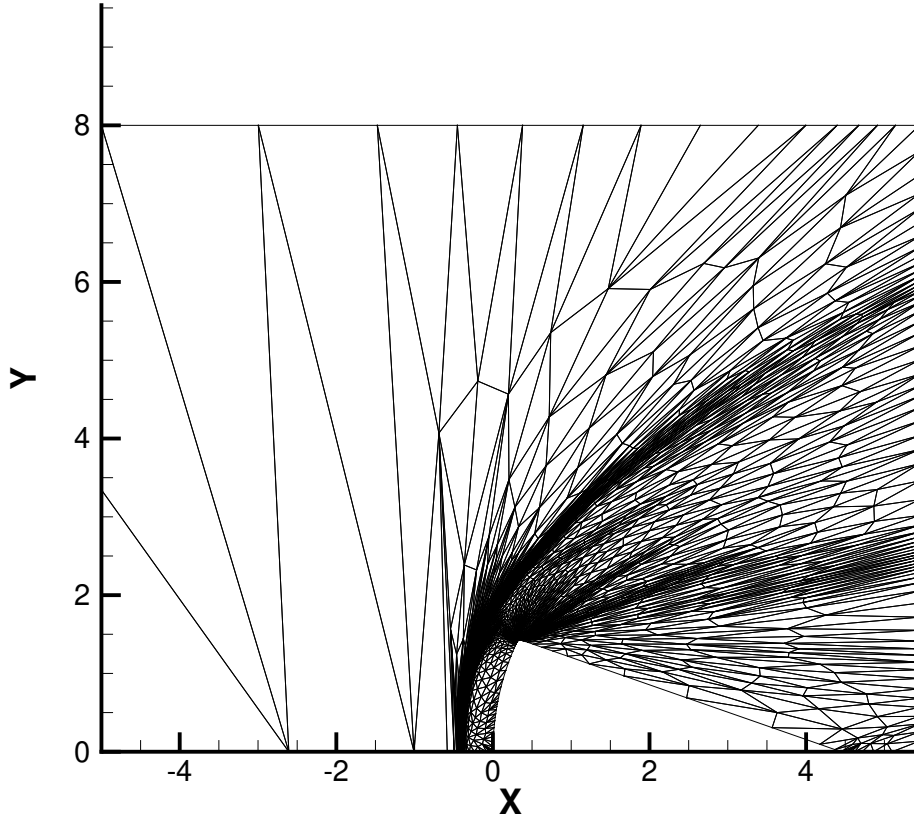
Figure 6-4: Adapt-iteration 50 mesh for the 2D ARD simplified capsule geometry, total enthalpy output functional.

Results from this case are used to inform initial mole fractions and temperature of the 0D reactor. They were averaged over the area traced out by the pink line segment shown in figure 6-5. This line segment corresponds to the capsule shoulder region between the capsule wall and the edge of the shockwave. The edge of the shockwave was determined approximately by the drop in temperature to that of the free stream. The numerical values used for the 0D calculation will be given in section 6.3.
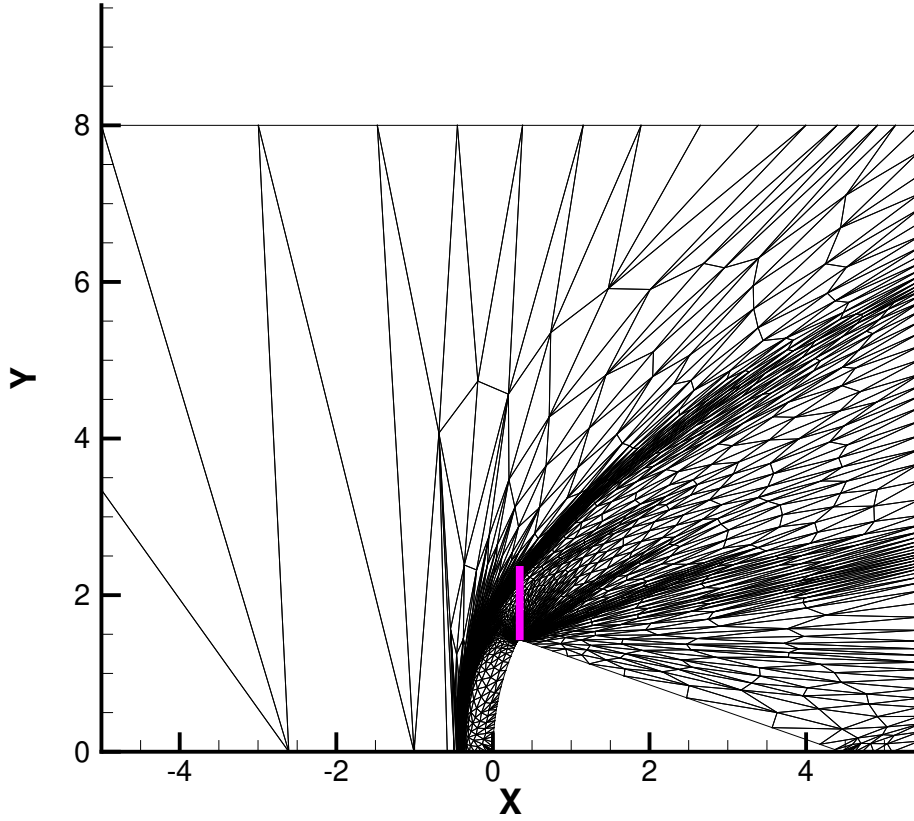
Figure 6-5: Adapt-iteration 50 mesh for the 2D ARD simplified capsule geometry, pink line indicates where species densities were sampled and averaged.

The pressure, transrotational temperature, and vibrational temperature contours are also presented in figures 6-6, 6-7, and 6-8. The shock is adequately resolved as shown. However, the "smearing" of the electron number density contours as seen in figure 6-3 can be attributed to the artifical viscosity used in stabilizing the calculation.
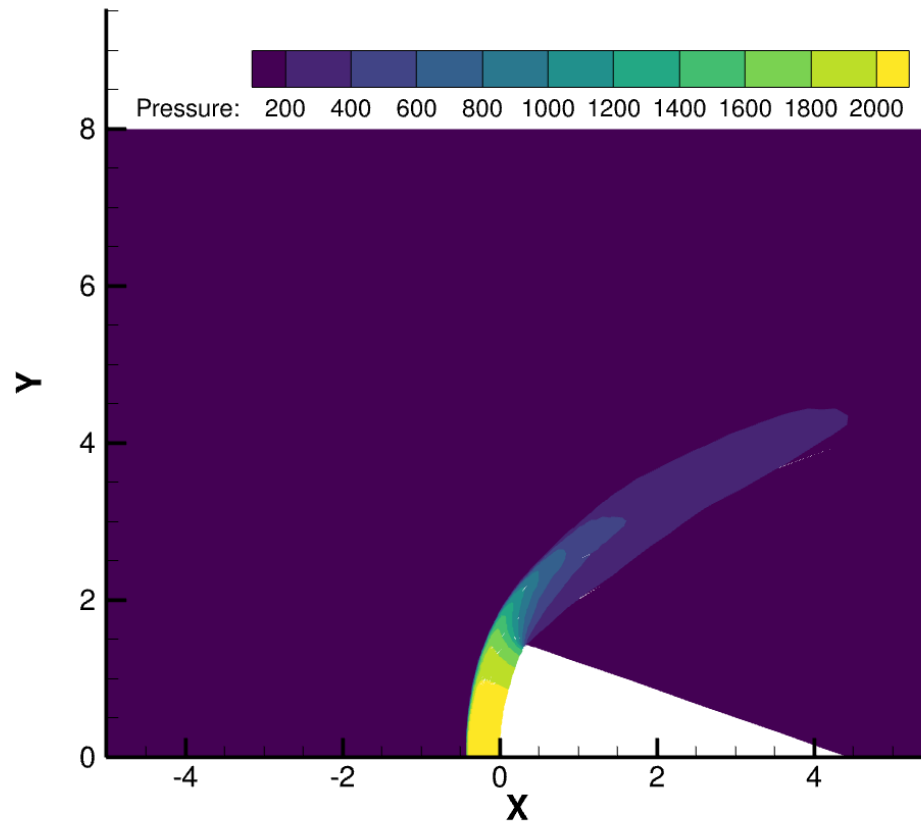
Figure 6-6: Pressure contours for the 2D ARD simplified capsule geometry.
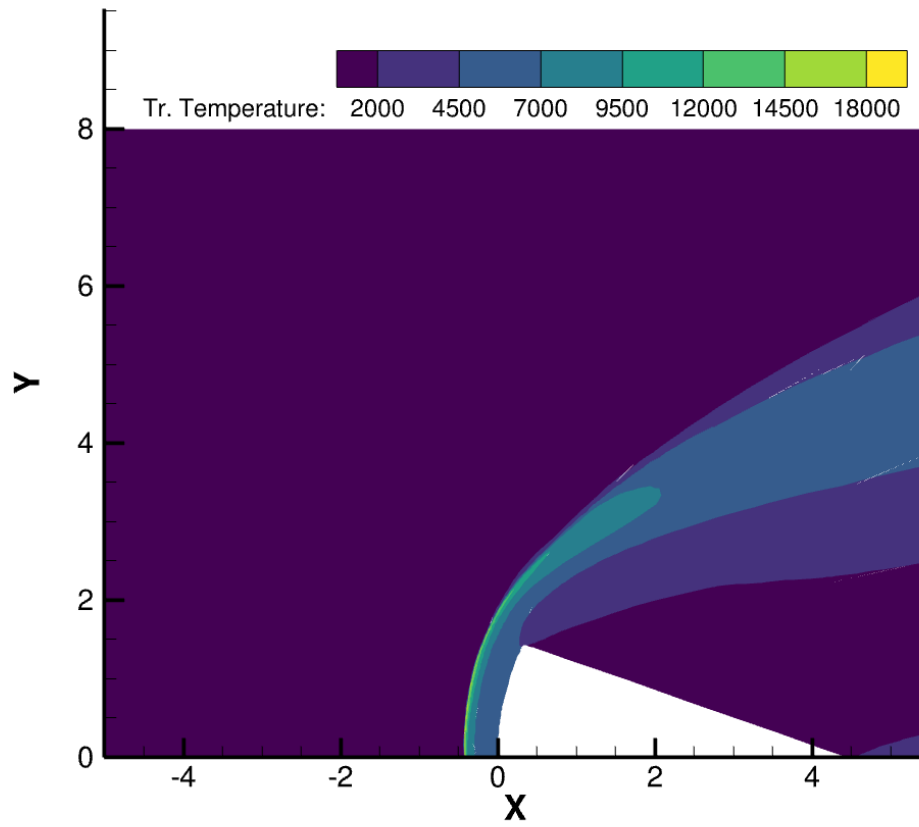
Figure 6-7: Transrotational temperature contours for the 2D ARD simplified capsule geometry.
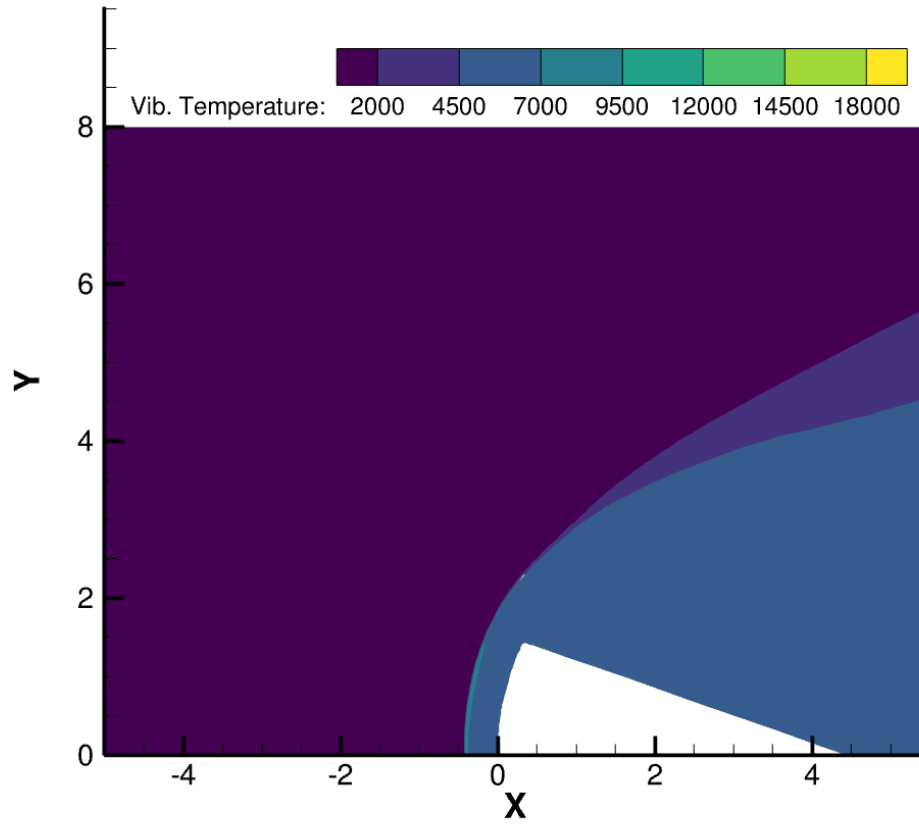
Figure 6-8: Vibrational temperature contours for the 2D ARD simplified capsule geometry.

Lastly, the x-velocity field is shown in figure 6-9. The speed in the expanding flow region on the leeward side of the capsule past the capsule shoulder is approximately 4000 meters per second.
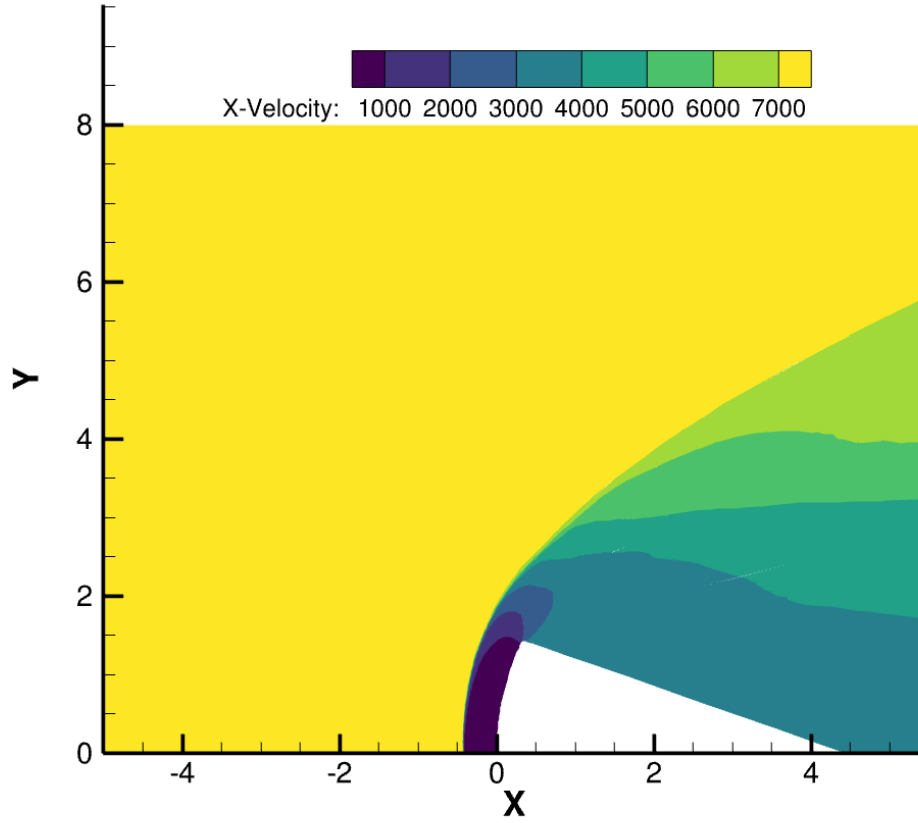
Figure 6-9: X-velocity contours for the 2D ARD simplified capsule geometry.

6.2.2 Output Functionals and Resulting Meshes

Total Enthalpy

The scalar output functional chosen for this work is that of the total enthalpy of equation (4.5), where $\alpha = 1$ and $\beta = 0$, integrated over the domain volume (domain area for the 2D problem). The cases were ran over target degree of freedom counts of 500, 1,000, 2,000, and 4,000. The results from these runs can be seen in figure 6-10. The results are converging by the time the target degree of freedom count is around 2,000, similar to what was observed in the validation cases and in Sabo et al [69].
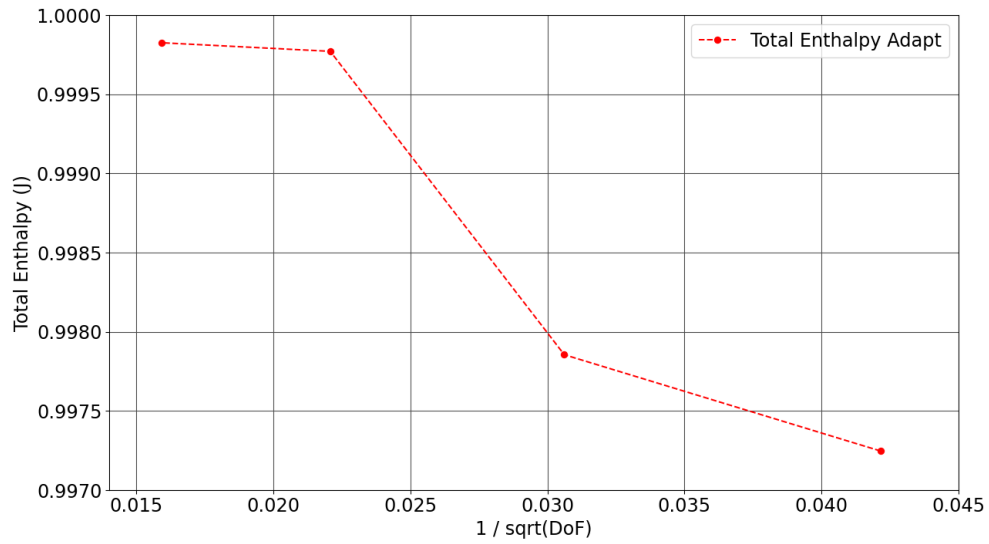
Figure 6-10: Dimensionless domain total enthalpy output as a function of DoF count.

The resulting meshes are seen in figures 6-11, 6-12, 6-13, and 6-14. It is clear that the and expansion regions become more and more refined as the adaptation process continues, indicating that these regions are the most important for minimization of discretization error in the total enthalpy output functional.
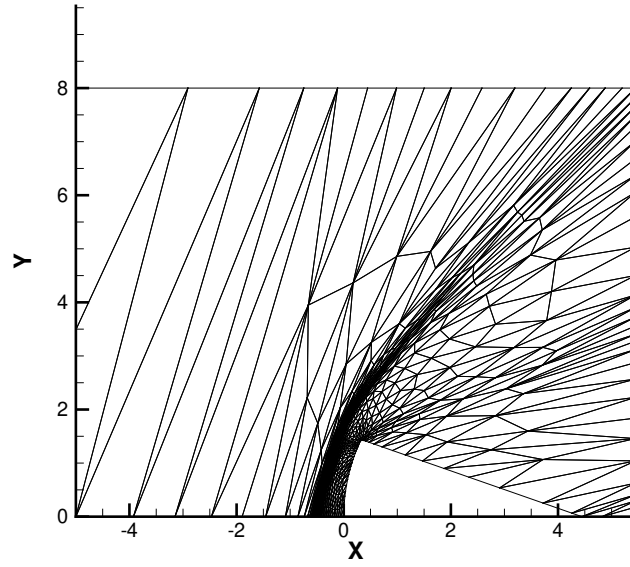
Figure 6-11: Total enthalpy adapted mesh for the target degree of freedom count of 500.
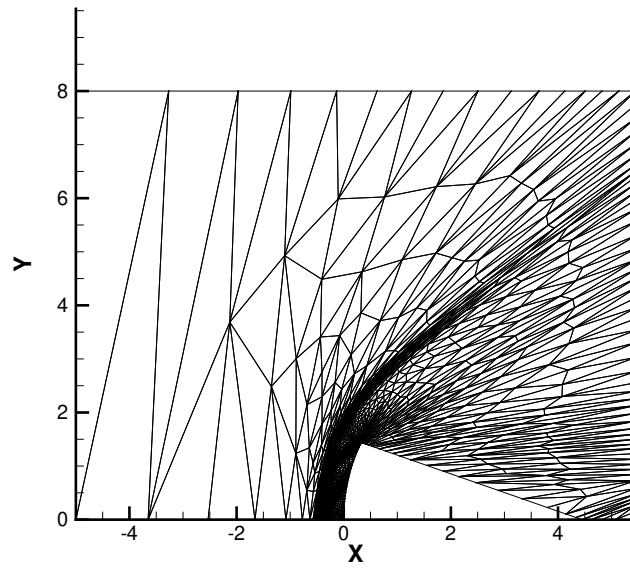
Figure 6-12: Total enthalpy adapted mesh for the target degree of freedom count of 1000.
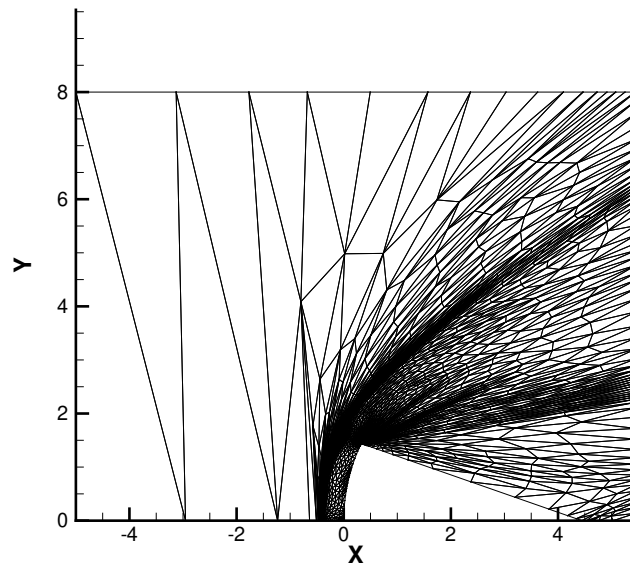
Figure 6-13: Total enthalpy adapted mesh for the target degree of freedom count of 2000.
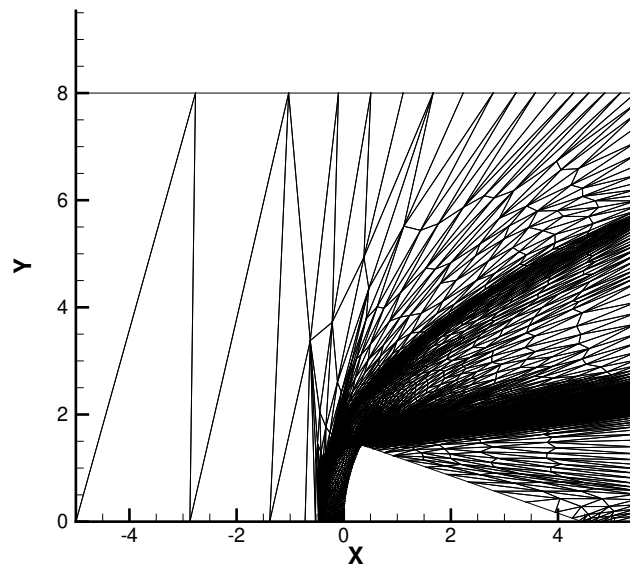
Figure 6-14: Total enthalpy adapted mesh for the target degree of freedom count of 4000.

6.3   0D Batch Reactor Model

A 0D batch reactor model provides an excellent way to study how SF_6 injection affects the timescales of electron quenching. As a reminder, the negative charge transferring from a lower mass particle (electron) to a higher mass particle (fluorine ion) allows for the effective decrease in critical plasma frequency. However, the critical piece for the alleviating of plasma blackout is how quickly this "charge transferring" process happens.

The velocity in the expanding flow region is approximately 4,000 meters per second and the length of the capsule is approximately 4 meters. The calculation of an approximate fluid residence time over the capsule is a mere 1 millisecond. In actual space-faring capsules, the residence time of the fluid may be even less, perhaps 0.5 milliseconds. Assuming the signal transmitter lies towards the top of the capsule, the time that the SF_6 has to quench the flow of electrons is small. If the transmitter is placed further upstream along the side of the capsule, the quenching time decreases further. Given that the capsule is blacked out with an electron number density on the order of $10^{16} - 10^{17}$, a two to three decade decrease in the electron number density is required to alleviate the blackout in the given time-span.

Utilizing the kinetic model developed in chapter 5, an array of temperatures, pressures, and initial SF_6 concentrations can be examined. Varying these parameters alters the rate coefficients and initial mole fractions of the air-plasma to which the SF_6 will be injected. A simplified capsule geometry is considered in section 6.2, and pressure and temperature bounds will be taken from its expanded flow field region, where a transmitter is most likely to reside. The initial concentrations of the air-plasma are taken from this model capsule flow field, as the plasma is inherently *not* in chemical equilibrium in the expanded shoulder region. The high concentration of electrons in a capsule geometry is developed in the high-temperature region at the front of the capsule, which can be thousands of Kelvin hotter than the expanded flow region. The chemical non-equilibrium allows for the larger initial electron concentration that is typically observed in an expanded flow region of a capsule. The degree of

thermal non-equilibrium also plays a significant role in the kinetics in this expanded flow region, but those effects will not be considered in this work.

The 0D reactor model will not be exploring the 11-species air model independently, as the initial concentrations of the weakly-ionized air are fully informed by CFD results. However, one case without SF_6 will be ran as a baseline to show the affects of *not* including SF_6 on the electron number density (i.e. show that the capsule remains blacked out). The 0D reactor model will be assumed thermalized, namely the transrotational and vibrational temperatures are equal ($T_{tr} = T_V$) at the starting time-step. This thermalization allows for a reduction in the temperature parameter space, allowing for a simpler analysis of chemical non-equilibrium effects without the additional effects from thermal non-equilibrium.

With all of these factors considered, the primary representative test case for the 0D model comprises of the parameters listed in table 6.2. The batch reactor simulation was carried out via Cantera [73], as mentioned in chapter 4. The nozzle exit was matched to the external pressure at the capsule shoulder wall and the exit Mach number M_e set to 5. The total temperature of the SF_6 is set to 20,500 K, a rather extreme value for this example, but serves to match the static temperatures in the external flow field, allowing for the densities to be easily matched by simple addition. The high total temperature also reduces the overall mass flow of SF_6, an undesired consequence, but truly tests the quenching capability of it in this model framework. The overall density is set in order to maintain consistency between the external flow-field and that of the SF_6 leaving the nozzle. Cantera automatically normalizes the mole fractions to unity, thus for the case without SF_6 present, the SF_6 is simply omitted from the input deck without any loss in applicability, but simply requires the density to be changed to that of the external flow field from the averaging of the SANS results.

6.3.1   11-Species Air Model

The 11-species air model takes the inlet conditions given in table 6.2 and sets $X_{SF_6} = 0$ and the density to $\rho = 2.749035$ e-04. The simulation is ran for a total of 2

Quantity	Value	Unit
X_{N_2}	1.020344 e-01	[-]
X_{O_2}	2.184972 e-03	[-]
X_N	1.846639 e-01	[-]
X_O	1.013491 e-01	[-]
X_{NO}	2.306845 e-03	[-]
$X_{N_2^+}$	4.858349 e-06	[-]
$X_{O_2^+}$	1.447582 e-06	[-]
X_{N^+}	2.428917 e-05	[-]
X_{O^+}	2.602836 e-05	[-]
X_{NO^+}	9.089442 e-05	[-]
X_{e^-}	1.475178 e-04	[-]
X_{SF_6}	6.071655 e-01	[-]
Density	3.656546 e-03	kg / m^3
Temperature	4000.0	K

Table 6.2: Initial mole fractions, density, and temperature for the 0D reactor model.

milliseconds, which is sufficient for the flow to fully pass the capsule geometry at 4,000 meters per second. Figure 6-15 shows the time history of the electron number density from the 0D batch reactor model.
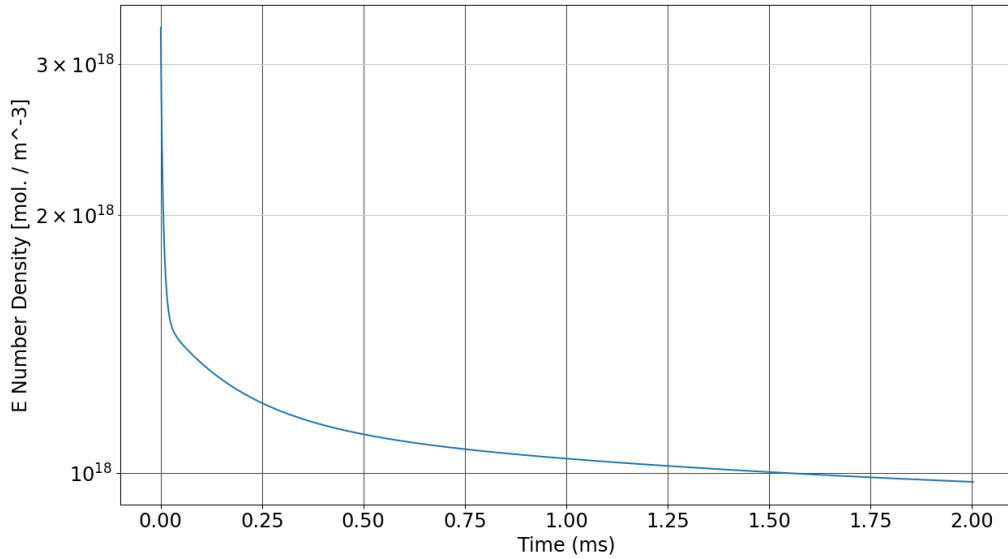
Figure 6-15: Electron number density for the 0D batch reactor model without SF_6 injection.

Comparing figure 6-15 to the electron number density contours of the SANS CFD solution in figure 6-3 shows that the results of the 0D batch reactor model and the SANS CFD are in good agreement. This agreement provides sufficient evidence for the applicability of a 0D bath reactor model for this particular problem.

6.3.2 36-Species Air-SF$_6$ Model

Utilizing the conditions described previously, the air-SF$_6$ mixture is also ran for 2 milliseconds. As seen in figure 6-16, the electron number density behaves as a pseudo first-order reaction over the course of the quenching process.
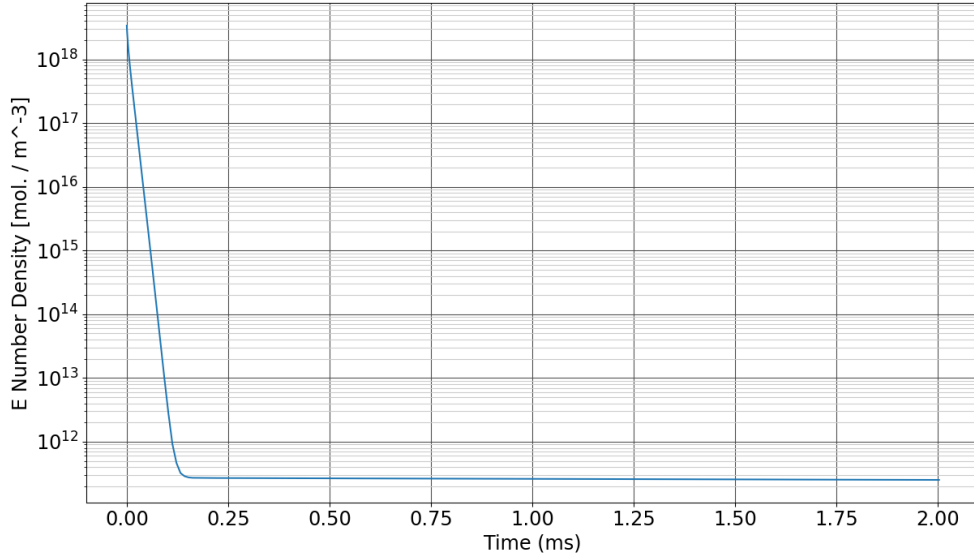
Figure 6-16: Electron number density for the 0D batch reactor model with SF$_6$ injection.

The rate of reduction is observed to have two main driving factors: 1) the use of electrophilic compounds (in this case, fluorine) readily quenches the electrons, and 2) the steep temperature reduction as a result of dissociating SF$_6$ cools the flow to ~ 1500 K, which promotes electronic recombination. This latter effect can be seen in figure 6-17. The temperature drop at the start of the simulation is found to be approximately 700 K in 1 nanosecond, or $\left| \frac{dT}{dt} \right|_{t=0} \approx \mathcal{O}(10^{11})$ K.

162

Clearly, the dissociation of SF_6 cools the flow and produces fluorine products, which are then available to ultimately recombine with electrons to produce F^-, completing the charge transfer process to heavier mass compounds.
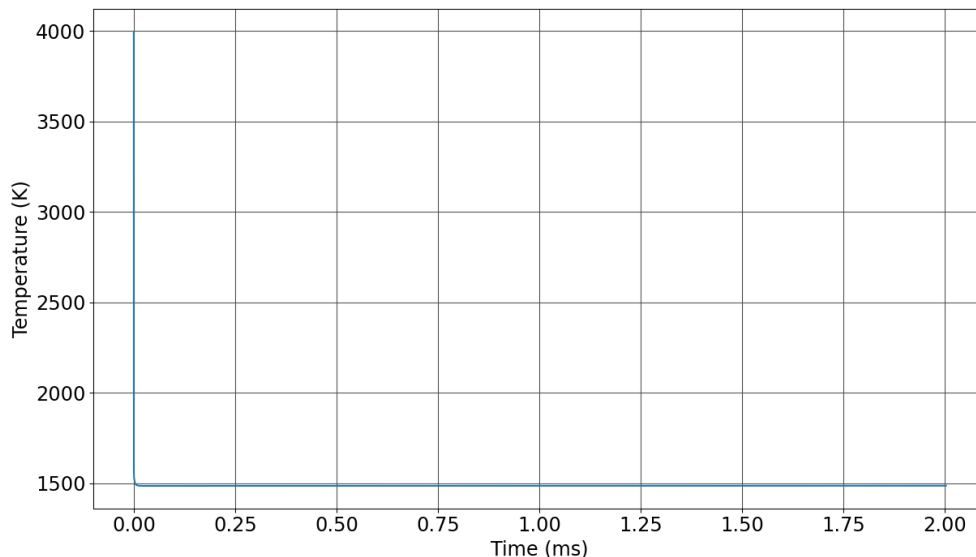
Figure 6-17: Temperature time history for the 0D batch reactor model with SF_6 injection. The highly endothermic dissociation of SF_6 contributes to the dramatic drop in temperature seen at the outset of the simulation.

6.3.3 Sensitivity Analysis

It is useful to identify which reactions the electron population is most sensitive to for several reasons. The first reason, which is the main concern for the engineering analysis, is which reaction dominates the chemical timescales for the electron recombination, and thus quenching, process. The second reason, which concerns future work, is to identify which chemical reactions rates ought to be further refined for the increased confidence in the modeling of the chemical kinetics.

The sensitivity of the electron concentration has been identified for the reactions surpassing a sensitivity threshold of $|S| > 0.1$, the time histories of which can be seen plotted in figure 6-18. It has been known in literature that the reaction

$$N + O \longrightarrow E + NO^+ \tag{6.14}$$

has been the primary producer of electrons within Park's 11-species air-plasma model. However, in this case, we see that the temperature reduction actually forces the reaction to favor the reverse direction.

More importantly, the recombination-dissociation reaction

$$e^- + F_2 \longrightarrow F + F^- \tag{6.15}$$

is shown to be the most dominant pathway for electron capture. This behavior indicates that some approximations to the overall electron quenching timescales can be carried out, which be seen in the following section.
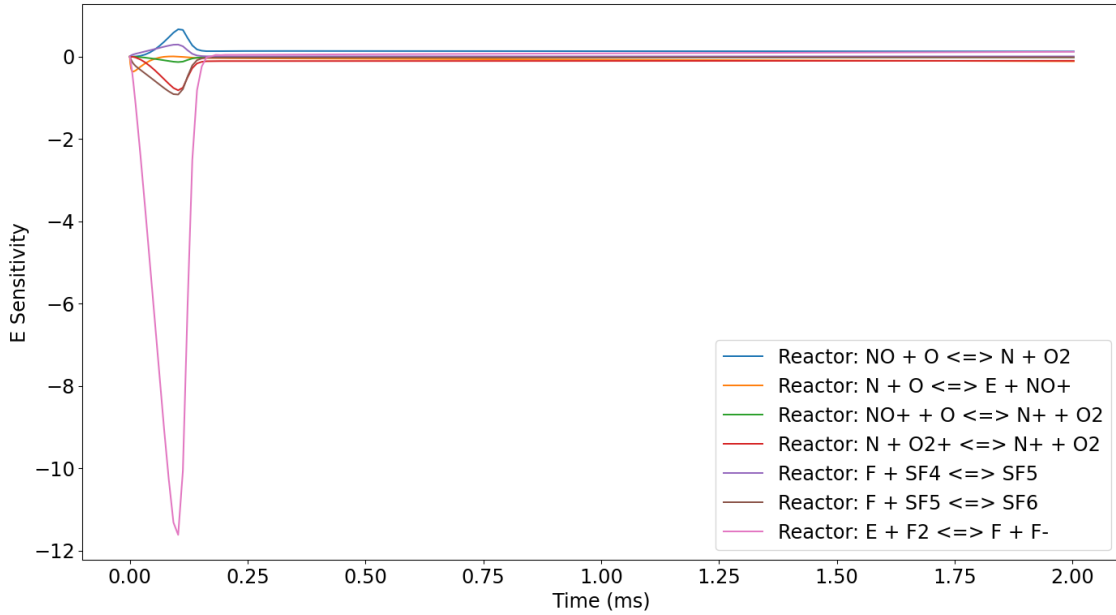
Figure 6-18: Most sensitive reactions for electron species production/depletion for 36-species air-SF_6 0D batch reactor model.

6.4   Analysis and Discussion of Results

The results generated and shown in figure 6-3 confirm the reduction of the electron number density by over 5 orders of magnitude within 0.125 milliseconds, much less than the required 1 millisecond from the flow residence time estimates. Restating the critical plasma frequency,

$$\omega_p \equiv \sqrt{\frac{n_e q_e^2}{\epsilon_0 m_e}} \tag{1.1}$$

this electron reduction produces an equivalent drop in the critical plasma frequency by a factor of $\sqrt{10^6}$ within 0.125 milliseconds. The conversion of the critical plasma frequency to that of a transmitter frequency is accomplished by dividing it by 2π:

$$f = \frac{\omega_p}{2\pi} \tag{6.16}$$

It is seen that the minimum required frequency of the transmitter has dropped by the factor of $\sqrt{10^6}$. Going from 10^{18} electrons per cubic meter to 10^{12} electrons per cubic meter corresponds to a maximum $\mathcal{O}(10 \text{ GHz})$ signal being attenuated to a maximum $\mathcal{O}(10 \text{ MHz})$ being attenuated. Now, a distance must be computed to assess whether or not this type of electron quenching system is feasible from an engineering perspective.

First, the sensitivity analysis shows that the electron population is most sensitive to the recombination-dissociation reaction

$$e^- + F_2 \longrightarrow F + F^- \tag{6.15}$$

which forward reaction rate (as written) increases as the temperature drops. Knowing this, an approximation for the overall electron depletion rate can be obtained via

$$\frac{d[e^-]}{dt} \approx -k(T)[F_2][e^-] \tag{6.17}$$
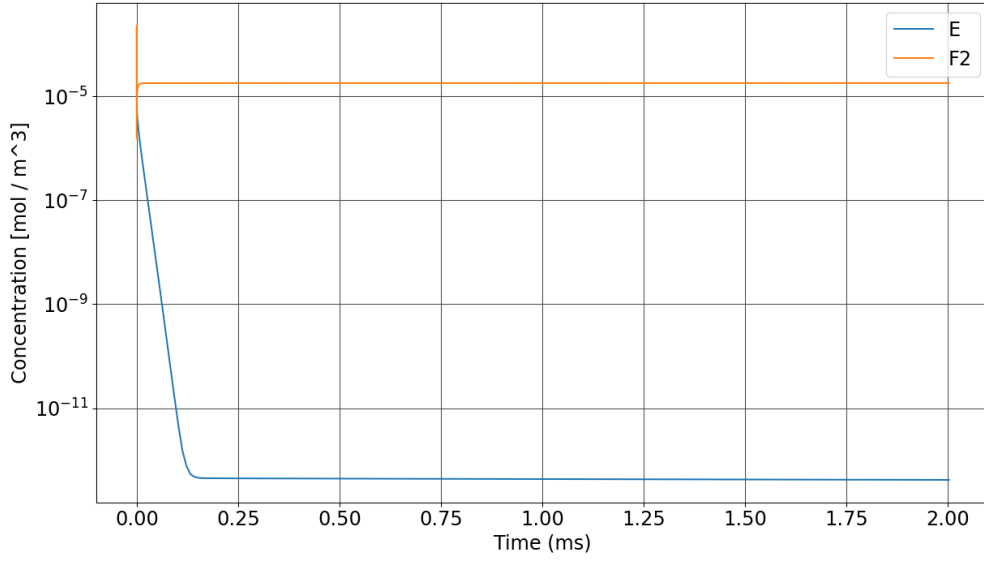
Figure 6-19: Time history of F_2 and electron concentration, indicating that $[F_2]/[e^-] \gg 1$ and that $[F_2]$ is essentially constant. This observation, combined with the sensitivity observations, supports the approximation of the chemical timescale of the electron quenching process as a pseudo first-order reaction with respect to $[F_2]$.

Second, the concentration of F_2 is seen to be relatively constant in figure 6-19 and much greater than the concentration of the electrons, thus one can assume that reaction (6.15) is flooded by F_2. Thus, one can further approximate the electron depletion rate given by equation (6.17) as a pseudo first-order reaction with a reaction rate $\kappa(T) = k(T)[F_2]$ as given via

$$\frac{d[e^-]}{dt} \approx -\kappa(T)[e^-] \tag{6.18}$$

Under these conditions, one integrates and finds

$$\kappa(T) = -\frac{\ln\left([e^-]/[e^-]_0\right)}{\Delta t} \tag{6.19}$$

which can be substituted into the Damköhler number in equation (6.1)

166

$$Da = \frac{\ln\left([e^-]_0/[e^-]\right)}{\Delta t} \frac{L}{U} \tag{6.20}$$

and thus gives the required length L for a given Damköhler number as

$$L = Da \frac{U\Delta t}{\ln\left([e^-]_0/[e^-]\right)} \tag{6.21}$$

The Damköhler number may be set by the engineer; however, for this work, a conservative estimate of 10 has been chosen. Ignoring momentum exchange from flow entrainment effects on the jet and instead taking the flow velocity U to be 4000 meters per second as an upper estimate (obtained from the SANS solution), the time it took for the electrons to be quenched Δt of 0.125 milliseconds, and the initial and 0.125 millisecond values of the electron concentrations of the representative case, $[e^-]_0$ and $[e^-]$, respectively, one finds the injector-transmitter separation distance L to be

$$\boxed{L = 10\frac{(4000 \text{ m/s})(0.000125 \text{ s})}{13.816} = 0.362 \text{ m}} \tag{6.22}$$

Given that the length of the model capsule is approximately 4 meters, this estimate of the required length L for the system indicates that this system is feasible for the quenching of electrons and alleviating plasma blackout under the current modeling approximations. Given a more realistic capsule design which is less "pizza" shaped, and thus likely shorter in length, this proposed method of alleviating plasma blackout comfortably fits within capsule size margins.

Chapter 7

Concluding Remarks and Future Work Identification

7.1 Feasibility of Electrophilic Compound Injection for Plasma Blackout Alleviation

Using SF_6 to as an electron quenchant in the plasma sheath of a hypersonic vehicle has been clearly demonstrated as a feasible option via a high-fidelity kinetics model. A first principles approach demonstrates that the use of an SF_6 injection system may reduce the electron number density by as much as five orders of magnitude in the span of a millisecond, assuming a well-mixed flow. If the flow is not well-mixed, the cold SF_6 jet positioned over the transmitter will effectively "punch out" an electron-free region, and given the higher electron affinity of SF_6 versus that of a single fluorine atom, any electrons that penetrate the cloud will be quenched immediately.

A few engineering realities must be considered for this system. Given the high mole fraction of SF_6 injected locally into the flow field, the static temperature of the injected SF_6 will be nearer to that of the nozzle exit temperature *if the jet produces no shocks*. This nozzle exit temperature will depend on the design parameters chosen by the engineer. The consequences from this potential situation are two-fold:

- the high mass-fraction of SF_6 in the local flow field will produce a relatively

low-temperature region, increasing electron recombination reactions

- the SF_6 remains intact in much higher quantities, increasing the electron quenching capabilities of the system if electrons permeate the highly-concentrated SF_6 region over the transmitter

A clever design may take advantage of an under-expanded nozzle flow to further "punch out" an optically thin window for a transmitter to transmit through, while also quenching any electrons that come into this highly-concentrated SF_6 region downstream of the injection point. Clearly, there are a few feasible options for engineering such a system.

The framework presented here allows for the full construction of a viscous TCNE model using *ab-initio* quantum chemistry methods. With the results produced by this methodology in this work, a fully viscous TCNE CFD model may be explored for the simulation of such a system, although it will be computationally expensive given the amount of species present. The methodology may also be used to further improve and refine estimates for current kinetic models and transport properties.

7.2   Future Work

Expanded Air-SF_6 Plasma Chemistry Model

For this work, electron recombination reactions with SF_6 and other species, such as SF_5, were not considered. The high-temperature case with rapid SF_6 dissociation to fluorine bi-products provides more than adequate quenching capability. In a lower-temperature case where SF_6 does not dissociate and shocks have *not* increased the temperature and dissociated the SF_6, the SF_6 will still work as it is more electrophilic than fluorine alone; however, the large amount of fluorine released via dissociation in the former case may act to improve the overall quenching rate. These increased fidelity models need to be explored for the adequate temperature and pressure ranges, keeping in mind that increasing the species count may make the CFD problem completely intractable. It is recommended that a 0D model, such as the ideal gas reactor, be

170

used to assess the concentrations of species present and determine which species are not required.

Another consideration is that of a pruning procedure for the desired species. While this work examined the equilibrium products and down-selected for species based on a low concentration cut-off, a more sophisticated and automated pruning procedure (such as that used in RMG [28]) for the sulfur and fluorine species mixed with air species may be developed. Doing so will allow for the reduction in species count for potential CFD simulations without excising certain rate-limiting chemical pathways or other critical chemical pathways.

Low-Pressure Kinetics of Models in the Literature

Noticeably, some chemical kinetic models in literature do not adequately account for the low-pressure kinetics and neglect to include collision species represented by $[M]$. It is strongly recommended going forward that unimolecular reactions and their associated reaction rate coefficients are specifically checked to be in the low-pressure limit, particularly if the pressures are anywhere below 100 atmospheres as demonstrated by this work. For a more quantitative way to estimate the onset pressure dependence for the rate coefficients, the author recommends to view the framework presented by Wong, Matheu, and Green [75].

To reiterate, as the temperature increases to larger and larger values, as seen in hypersonic flows and in this work, the rate coefficients are pushed further towards the low-pressure limit, as expected. Because the average reactant population energy increases, more collisions are required to thermally deactivate an unimolecular product into its energy well. The CTST formulation specifically calculates the high-pressure limit rate coefficient as it is assumed that no recrossing may occur from products back to reactants - this lack of recrossing is what identically happens in the high-pressure limit. Therefore, using a CTST rate coefficient for a low-pressure limit reaction is technically incorrect.

Jet Dynamics Considerations

While the detailed chemical kinetics involved in the electrophilic injection system are demonstrated to be feasible and understood in this work, the fluid dynamics of the jet injection mechanism must be considered in detail going forward. Two potential solutions exist for the jet to quench the electrons:

1. The SF_6 jet is designed in such a way as to mechanically displace the free electrons passing over the shoulder of the capsule by means of sufficiently under-expanding the injection nozzle flow, thereby reducing the electron number density and creating a stream of cool SF_6 over the transmitter.

2. The SF_6 jet mixes with the incoming flow, quenching the free electrons as they come into contact with each other by means of the chemical kinetics at play.

The under-expanding of a jet into the leeward flow over the capsule provides a potentially attractive solution to mitigate plasma blackout. However, the jet will need to be at a sufficiently high exit pressure in order to overcome the momentum of the incoming flow around the capsule shoulder. A 1-D momentum flux balance suggests that the static pressure of the jet will have to be on the order of 5,000 Pascals in order to cancel out the momentum of the incoming flow, and would have to be higher still to effectively displace it as the jet moves away from the nozzle exit plane. For a SF_6 reservoir pressure of 1 atmosphere and reservoir temperature of 1,000 Kelvin, utilizing an exit area on the order of 0.1 square meters, the mass flow rate for such a system is on the order of 10 kilograms per second. In this scenario, the SF_6 mole fraction is seven orders of magnitude higher than that of the free electrons. Even if one considers pulsing the jet to allow transmissions to be quickly transmitted, the weight of such a system designed in this way may be cost-prohibitive from the amount of SF_6 required. One way to effectively reduce the required mass is to increase the reservoir temperature; however, a power source for this may be prohibitive for the aforementioned reasons of weight considerations. Considering this system would only be used in re-entry conditions that produce weakly-ionized plasmas, one more

"exotic" solution for this particular problem may be utilize a thermal management system to transfer the heat from the thermal protection system on re-entry to the SF_6 tank, utilizing it as a heat sink, thereby increasing its reservoir temperature. While a thermal management system like one proposed here seemingly complicates the issue of heating the tank, many reasons can be imagined for the use of such thermal management systems on re-entry vehicles, particularly for reduced ablation rates and increased re-usability of the thermal protection system. Regardless, the mass of such a system in a practical setting is likely prohibitively large and is thus not recommended.

The second solution involves mixing the jet with the incoming flow. For the electrophilic compounds to recombine with the free electrons, they both need to come into contact with each other - the SF_6 stream and free-electrons must mix. A key quantity of interest to assess whether or not the system can perform would be a Damköhler number for the mixing time versus the residence time:

$$Da_{mr} = \frac{\tau_{mix}}{\tau_{res}} = \frac{U\tau_{mix}}{L} \tag{7.1}$$

which can be used to give the engineer an idea of how much length is required for the stream to sufficiently mix. Another key quantity is the comparison of the mixing and chemistry timescales:

$$Da_{mc} = \frac{\tau_{mix}}{\tau_{chem}} = \kappa(T)\tau_{mix} \tag{7.2}$$

where the $\kappa(T)$ from before is generated from the perfectly stirred ideal gas reactor analysis. Given that the residence timescales and the chemistry timescales can now be assessed, a suitable estimate for the mixing timescale needs to be determined. For the capsule explored in this work, the Reynolds number based on the diameter of the capsule and free stream conditions is $Re_D \approx 6.1 \times 10^4$, indicating that the assumption of laminar flow around the capsule is reasonable [76, 77]. The supersonic laminar crossflow jet problem has been studied under similar (local) conditions for this problem by Kawai and Lele [78]. The use of large-eddy simulation is shown

to give qualitative agreement with experimental data for the key physics and flow structures in their model problem; however, chemical reactions were not considered in their work. One key parameter of interest that Kawai and Lele highlight is the jet-to-crossflow momentum flux ratio,

$$J = \frac{\rho_{jet} U_{jet}^2}{\rho_{amb} U_{amb}^2} \tag{7.3}$$

which is used to determine the jet penetration distance. For this type of flow, it is not obvious where the optimal location of the injector would be to minimize the denominator in equation 7.3. However, if the injector were placed near the capsule shoulder, the velocity, U_{amb}, is approximately 3,000 meters per second and the ambient density, ρ_{amb}, is approximately 2.7×10^{-4} kilograms per cubic meter. For an ambient jet pressure of 800 Pascals, the tank pressure required for a Mach 2 jet is approximately 6,000 Pascals. For a tank temperature of 1,000 Kelvin, the resulting exit jet velocity is approximately 430 meters per second and exit jet density is 2.3×10^{-2} kilograms per cubic meter. Plugging in these values results in a jet-to-crossflow momentum flux ratio of $J = 1.75$, indicating the jet will adequately penetrate, similar to what is shown by Kawai and Lele [78]. However, consideration must be shown to the highly 3-dimensional nature of realistic capsule re-entry flows produced by non-zero angles-of-attack, and it must be determined how the jet will proceed downstream in order to ensure that it quenches the electrons above the transmitter all the way through to the shockwave edge so that the signal can propagate through the entire shock layer to the outside world. For this type of system under these conditions, the resulting mass flow rate for a nozzle exit area of 0.1 square meters is approximately 1 kilogram per second, an order of magnitude lower than the first potential solution, with a SF_6 mole fraction 5 orders of magnitude larger than that of the electrons.

Ultimately, several key areas must be addressed:

1. What are the engineering criteria for the determination of τ_{mix}?

2. What range of jet-to-crossflow momentum flux ratios produce temporally (τ_{mix}) adequate mixing as quantified by Da_{mr} and Da_{mc}?

174

3. Given the capsule geometry and the post-shoulder flow expansion, where is the optimal jet injection location for adequate electron quenching throughout the shock layer above the transmitter, and what parameters govern this location? For example, how does the location depend on the ratio of the jet penetration distance to the shockwave edge distance away from the capsule body?

4. How do 3-dimensional flow features produced from re-entering capsule geometries at non-zero angles-of-attack affect the ability of the jet to sufficiently mix and quench electrons within the plasma sheath? How do the pathlines for the SF_6 and electrons vary? Do the electrons remain quenched above the transmitter?

5. Do alternative, non-circular nozzle exit geometries provide better, more robust SF_6 coverage, such as that of a circumstantially distributed nozzle array (e.g. array of mini-axisymmetric nozzles, rectangular "strip" nozzle) around part of the capsule versus that of a single axisymmetric nozzle?

An numerical experiment that could help begin to address these questions is that of a hypersonic, laminar, chemically reacting flat plate with an injection port for SF_6. The viscous TCNE equations defined in this work would govern this flow field. The free stream inlet conditions for such a flow would utilize the flow field profiles generated from the capsule geometry of a simpler model, such as the one developed in this work. A test matrix that includes the injection location, injection angle, and jet-to-crossflow momentum flux ratio would serve as a baseline matrix to begin assessing the performance of such a system. Key quantities of interest that govern Da_{mr} and Da_{mc} should also be explored, particularly in the assessment of the mixing timescale τ_{mix}. The quantities required for the viscous flow involving the compounds presented in this work, and how to calculate them, are presented in appendix D and chapter 2, respectively.

Appendix A

Chemical Species Properties

Table A.1: Chemical species properties used in air-SF$_6$ plasma model. Characteristic vibrational temperature, Θ_{vib}, calculated using MP2/6-311+G(3df) level of theory. For more accurate results, one should use a higher level of theory, such as CCSD(T)//MP2/6-311+G(3df), at the expense of increased computational effort.

Species	Molar Mass [g/mol]	Θ_{vib} [K]
e	5.485799 e-04	-
F	18.998	-
F$^-$	18.998	-
F$_2$	37.996	1422
FO	34.997	1939
N	14.007	-
N$^+$	14.007	-
N$_2$	28.014	3158
N$_2^+$	28.014	4560
NF	33.005	1815
NF2	52.003	859, 1425, 1643
NO	30.006	4674
NO$^+$	30.006	3142
NOF	49.004	868, 1670, 3239
NSO	62.071	463, 844, 2564
O	15.999	-
O$^+$	15.999	-
O$_2$	31.998	2146
O$_2^+$	31.998	2210
OSN	62.071	494, 1067, 1510
S	32.065	-
S$^+$	32.065	-
S$_2$	64.130	987
S$_2$O	80.129	544, 999, 1691
SF	51.063	1198
SF$_2$	70.061	500, 1167, 1208
SF$_3$	89.059	228, 530, 679, 831, 1034, 1238
SF$_4$	108.057	329, 511, 663, 762, 762, 804, 1060, 1250, 1288
SF$_5$	127.055	363, 530, 530, 680, 771, 771, 829, 867, 956, 1251, 1251, 1292
SF$_6$	146.053	507, 507, 507, 756, 756, 756, 897, 897, 897, 933, 933, 1123, 1383, 1383, 1383
SN	46.072	2296
SO	48.063	1490
SO$_2$	64.061	724, 1623, 1942
SO$_2$F	83.059	585, 615, 791, 1090, 1719, 2109
SO$_2$F$_2$	102.057	546, 547, 772, 773, 785, 1209, 1255, 1864, 2215
SOF$_2$	86.059	527, 555, 748, 1043, 1139, 1967

Appendix B

Chemical Kinetics Model Data

Table B.1: Selected reactions for air plasma, Arrhenius reactions:
$k_f(T_f) = A T_f^{\beta} \exp\left(-E_a/T_f\right)$.
The activation temperature of the preferential-dissociation reactions $T_a = \sqrt{T_{tr}T_V}$.

No.	Reaction	A	β	E_a [K]	T_f	T_r	Ref.
1	$N_2 + M_1 \longrightarrow N + N + M_1$	7.0 e21	-1.60	113,200	T_a	T_{tr}	[36]
2	$N_2 + M_2 \longrightarrow N + N + M_2$	3.0 e22	-1.60	113,200	T_a	T_{tr}	[36]
3	$N_2 + e \longrightarrow N + N + e$	1.2 e25	-1.60	113,200	T_a	T_{tr}	[36]
4	$O_2 + M_1 \longrightarrow O + O + M_1$	2.0 e21	-1.50	59,500	T_a	T_{tr}	[36]
5	$O_2 + M_2 \longrightarrow O + O + M_2$	1.0 e22	-1.50	59,500	T_a	T_{tr}	[36]
6	$NO + M_3 \longrightarrow N + O + M_3$	5.0 e15	0.00	75,500	T_a	T_{tr}	[36]
7	$NO + M_4 \longrightarrow N + O + M_4$	1.1 e17	0.00	75,500	T_a	T_{tr}	[36]
8	$NO + O \longrightarrow N + O_2$	8.4 e12	0.00	19,450	T_{tr}	T_{tr}	[36]
9	$N_2 + O \longrightarrow NO + N$	6.4 e17	-1.00	38,400	T_{tr}	T_{tr}	[36]
10	$N + O \longrightarrow NO^+ + e$	8.8 e08	1.00	31,900	T_{tr}	T_{tr}	[36]
11	$O + O \longrightarrow O_2^+ + e$	7.1 e02	2.70	80,600	T_{tr}	T_{tr}	[36]
12	$N + N \longrightarrow N_2^+ + e$	4.4 e07	1.50	67,500	T_{tr}	T_{tr}	[36]
13	$NO^+ + O \longrightarrow N^+ + O_2$	1.0 e12	0.50	77,200	T_{tr}	T_{tr}	[36]
14	$N^+ + N_2 \longrightarrow N_2^+ + N$	1.0 e12	0.50	12,200	T_{tr}	T_{tr}	[36]
15	$O_2^+ + N \longrightarrow N^+ + O_2$	8.7 e13	0.14	28,600	T_{tr}	T_{tr}	[36]
16	$O^+ + NO \longrightarrow N^+ + O_2$	1.4 e05	1.90	26,600	T_{tr}	T_{tr}	[36]
17	$O_2^+ + N_2 \longrightarrow N_2^+ + O_2$	9.9 e12	0.00	40,700	T_{tr}	T_{tr}	[36]
18	$O_2^+ + O \longrightarrow O^+ + O_2$	4.0 e12	-0.09	18,000	T_{tr}	T_{tr}	[36]
19	$NO^+ + N \longrightarrow O^+ + N_2$	3.4 e13	-1.08	12,800	T_{tr}	T_{tr}	[36]
20	$NO^+ + O_2 \longrightarrow O_2^+ + NO$	2.4 e13	0.41	32,600	T_{tr}	T_{tr}	[36]
21	$NO^+ + O \longrightarrow O_2^+ + N$	7.2 e12	0.29	48,600	T_{tr}	T_{tr}	[36]
22	$O^+ + N_2 \longrightarrow N_2^+ + O$	9.1 e11	0.36	22,800	T_{tr}	T_{tr}	[36]
23	$NO^+ + N \longrightarrow N_2^+ + O$	7.2 e13	0.00	35,500	T_{tr}	T_{tr}	[36]
24	$O + e \longrightarrow O^+ + e + e$	3.9 e33	-3.78	158,500	T_e	T_e	[36]
25	$N + e \longrightarrow N^+ + e + e$	2.5 e34	-3.82	168,600	T_e	T_e	[36]
26	$O^+ + e \longrightarrow O + h\nu$	1.07 e11	-0.52	0	T_e	-	[36]
27	$N^+ + e \longrightarrow N + h\nu$	1.52 e11	-0.48	0	T_e	-	[36]

$M_1 = N_2, O_2, NO, N_2^+, O_2^+, NO^+$.
$M_2 = N, O, N^+, O^+$.
$M_3 = N_2, O_2, N_2^+, O_2^+, NO^+$.
$M_4 = N, O, NO, N^+, O^+$.

Table B.2: Selected reactions for SF_6 plasma Arrhenius reactions:
$k_f(T_f) = AT_f^{\beta} \exp\left(-E_a/T_f\right)$.

No.	Reaction	A	β	E_a [K]	T_f	T_r	Ref.
28	$S^+ + e + e \longrightarrow S + e$	3.13 e23	-1.5	120,230	T_e	T_e	[79]
29	$F + F + F \longrightarrow F_2 + F$	3.25 e-11	0	0	T_{tr}	T_{tr}	[79]
30	$F + S + F \longrightarrow SF + F$	1.69 e-10	0	0	T_{tr}	T_{tr}	[79]
31	$S + S + F \longrightarrow S_2 + F$	2.71 e-10	0	0	T_{tr}	T_{tr}	[79]
32	$SF_4 + F_2 \longrightarrow SF_6$	1.58 e13	0	7,340	T_{tr}	T_{tr}	[79]
33	$F_2 \longrightarrow F + F$	2.12 e13	0	16,970	T_{tr}	T_{tr}	[79]
34	$SF_5 + F_2 \longrightarrow SF_6 + F$	1.58 e13	0	2,438	T_{tr}	T_{tr}	[79]
35	$S_2 \longrightarrow S + S$	4.79 e13	0	38,749	T_{tr}	T_{tr}	[79]
36	$SF_4 + F \longrightarrow SF_3 + F_2$	3.98 e10	0	1,005	T_{tr}	T_{tr}	[79]
37	$SF_4 + F_2 \longrightarrow SF_5 + F$	1.58 e13	0	7,340	T_{tr}	T_{tr}	[79]
38	$SF_4 + F \longrightarrow SF_5$	3.98 e13	0	1,005	T_{tr}	T_{tr}	[79]
39	$SF_5 + F \longrightarrow SF_6$	1.00 e13	0	0	T_{tr}	T_{tr}	[79]
40	$SF_5 + SF_5 \longrightarrow SF_4 + SF_6$	1.00 e13	0	855	T_{tr}	T_{tr}	[79]
41	$F_2 + e \longrightarrow F + F + e$	1.81 e14	0	0	T_{tr}	T_{tr}	[79]
42	$F + e + F \longrightarrow F^- + F$	6.02 e12	0	40,000	T_{tr}	T_{tr}	[79]
43	$F^- + S^+ + F \longrightarrow SF + F$	4.41 e04	-2.5	0	T_{tr}	T_{tr}	[79]

Table B.3: Selected reactions for SF_6 plasma using Lennard-Jones method:
$k_f(T_f) = A \exp\left(B + CT_f + DT_f^2\right) \exp\left(-E/T_f\right)$.

No.	Reaction	A	B	C	D	E	T_f	T_r	Ref.
44	$SF_6 + SF_2 \longrightarrow SF_4 + SF_4$	3.14 e04	16.669	1.25 e-04	-8.10 e-09	15,082	T_{tr}	T_{tr}	[79]
45	$SF + SF \longrightarrow F_2 + S_2$	3.14 e06	16.549	1.03 e-04	-5.72 e-09	12,468	T_{tr}	T_{tr}	[79]
46	$F + SF \longrightarrow F_2 + S$	3.14 e06	16.347	1.50 e-04	-1.07 e-08	22,267	T_{tr}	T_{tr}	[79]
47	$F + SF \longrightarrow SF_2$	3.14 e06	16.347	1.50 e-04	-1.07 e-08	0	T_{tr}	T_{tr}	[79]
48	$F_2 + S \longrightarrow SF_2$	3.14 e05	16.572	9.99 e-05	-5.34 e-09	5,027	T_{tr}	T_{tr}	[79]
49	$SF + F_2 \longrightarrow SF_2 + F$	3.14 e05	16.345	1.47 e-04	-1.05 e-08	5,027	T_{tr}	T_{tr}	[79]
50	$SF + SF \longrightarrow S + SF_2$	3.14 e06	16.549	1.03 e-04	-5.72 e-09	0	T_{tr}	T_{tr}	[79]
51	$S_2 + F_2 \longrightarrow SF_2 + S$	3.14 e04	16.654	9.99 e-05	-5.34 e-09	15,082	T_{tr}	T_{tr}	[79]
52	$SF_2 + F \longrightarrow SF_3$	3.14 e05	16.473	1.50 e-04	-1.07 e-08	5,027	T_{tr}	T_{tr}	[79]
53	$SF_2 + F_2 \longrightarrow SF_3 + F$	3.14 e04	16.432	1.47 e-04	-1.05 e-08	15,082	T_{tr}	T_{tr}	[79]
54	$SF + F_2 \longrightarrow SF_3$	3.14 e05	16.345	1.47 e-04	-1.05 e-08	5,027	T_{tr}	T_{tr}	[79]
55	$SF_2 + SF_2 \longrightarrow SF_3 + SF$	3.14 e04	16.669	1.03 e-04	-5.71 e-09	27,421	T_{tr}	T_{tr}	[79]
56	$SF_3 + F \longrightarrow SF_4$	3.14 e06	16.567	1.44 e-04	-1.01 e-08	0	T_{tr}	T_{tr}	[79]
57	$SF_2 + F_2 \longrightarrow SF_4$	3.14 e04	16.432	1.47 e-04	-1.05 e-08	15,082	T_{tr}	T_{tr}	[79]
58	$SF_3 + SF_3 \longrightarrow SF_2 + SF_4$	3.14 e06	16.489	1.44 e-04	-1.01 e-08	0	T_{tr}	T_{tr}	[79]
59	$SF_2 + SF_2 \longrightarrow SF_4 + S$	3.14 e04	16.669	1.03 e-04	-5.71 e-09	27,965	T_{tr}	T_{tr}	[79]
60	$SF_3 + F_2 \longrightarrow SF_5$	3.14 e05	16.488	1.44 e-04	-1.01 e-08	5,027	T_{tr}	T_{tr}	[79]

Table B.4: Selected reactions for SF_6 plasma using other rates:
$k_f(T_f) = A + BT_f + CT_f^2 + DT_f^3 + ET_f^4$.

No.	Reaction	A	B	C	D	E	T_f	T_r	Ref.
68	$F + e + e \longrightarrow F^- + e$	3.20 e-07	-0.69 e-11	7.65 e-15	-4.03 e-19	8.13 e-24	T_e	T_e	[79]
69	$F + e \longrightarrow F^- + h\nu$	1.52 e09	-2.08 e05	2.30 e01	-1.12 e-03	2.03 e-08	T_e	-	[79]
70	$F_2 + e \longrightarrow F^- + F$	6.14 e15	-3.00 e11	-1.96 e08	2.81 e04	0	T_e	T_e	[79]
71	$F + F \longrightarrow F_2 + h\nu$	-1.73 e01	5.83 e-02	-1.43 e-07	5.94 e-09	-3.40 e-13	T_{tr}	-	[79]

Table B.5: Selected reaction rates for air-SF$_6$ plasma "interfacial" species.

No.	Reaction	A	β	E_a [K]	T_f	T_r	Level of Theory	Ref.
72	F + NO + M $\longrightarrow$ NOF + M	2.87 e14	-1.45	3,981	T_{tr}	T_{tr}	MP2/cc-pvtz	This work
73	NF$_2$ + N $\longrightarrow$ NF + NF	8.80 e07	1.66	30,420	T_{tr}	T_{tr}	MP2/cc-pvtz	This work
74	NF$_2$ + O $\longrightarrow$ NF + FO	3.97 e08	1.69	33,776	T_{tr}	T_{tr}	MP2/cc-pvtz	This work
75	NF$_2$ + S $\longrightarrow$ NF + SF	8.17 e07	1.65	23,775	T_{tr}	T_{tr}	MP2/cc-pvtz	This work
76	S + NO $\longrightarrow$ SN + O	5.15 e10	1.04	33,054	T_{tr}	T_{tr}	MP2/cc-pvtz	This work
76.1	S + NO + M $\longrightarrow$ NSO + M	4.21 e02	1.62	9,354	T_{tr}	T_{tr}	MP2/cc-pvtz	This work
76.2	NSO + M $\longrightarrow$ SN + O + M	6.50 e08	-0.11	24,295	T_{tr}	T_{tr}	MP2/cc-pvtz	This work
77	S + NO $\longrightarrow$ SO + N	9.33 e09	1.17	33,228	T_{tr}	T_{tr}	MP2/cc-pvtz	This work
77.1	OSN + M $\longrightarrow$ S + NO + M	1.64 e07	0.25	5,652	T_{tr}	T_{tr}	MP2/cc-pvtz	This work
77.2	OSN + M $\longrightarrow$ SO + N + M	1.07 e03	1.36	18,731	T_{tr}	T_{tr}	MP2/cc-pvtz	This work
78	S$_2$O + M $\longrightarrow$ S$_2$ + O + M	1.75 e20	-2.85	60,916	T_{tr}	T_{tr}	MP2/cc-pvtz	This work
79	SO$_2$F + M $\longrightarrow$ SO$_2$ + F + M	3.20 e19	-2.86	19,922	T_{tr}	T_{tr}	MP2/cc-pvtz	This work
80	NOF + M $\longrightarrow$ NF + O + M	2.15 e20	-2.88	57,980	T_{tr}	T_{tr}	MP2/6-311+G(3df)	This work
81	S$_2$ + O $\longrightarrow$ S + SO	6.85 e09	1.03	3,108	T_{tr}	T_{tr}	MP2/6-311+G(3df)	This work
82	SF + O $\longrightarrow$ SO + F	1.96 e10	0.99	1,352	T_{tr}	T_{tr}	MP2/6-311+G(3df)	This work
83	F + N + M $\longrightarrow$ NF + M	2.25 e14	0.00	0	T_{tr}	T_{tr}	Diff-Limited (hard sphere)	This work
84	F + O + M $\longrightarrow$ FO + M	2.23 e14	0.00	0	T_{tr}	T_{tr}	Diff-Limited (hard sphere)	This work
85	S + O + M $\longrightarrow$ SO + M	2.36 e14	0.00	0	T_{tr}	T_{tr}	Diff-Limited (hard sphere)	This work
86	S + N + M $\longrightarrow$ SN + M	2.32 e14	0.00	0	T_{tr}	T_{tr}	Diff-Limited (hard sphere)	This work
87	F + SO$_2$F $\longrightarrow$ SO$_2$F$_2$	3.57 e08	2.136	28,760	T_{tr}	T_{tr}	CCSD(T)//B3LYP/6-311G(d,p)	[80]
88	F$_2$ + SO$_2$ $\longrightarrow$ SO$_2$F$_2$	5.01 e02	2.965	194,110	T_{tr}	T_{tr}	CCSD(T)//B3LYP/6-311G(d)	[80]
89	SO$_2$F + SF$_5$ $\longrightarrow$ SF$_6$ + SO$_2$	1.05 e01	2.945	117,521	T_{tr}	T_{tr}	CCSD(T)//B3LYP/6-311+G(3df)	[80]
90	SO$_2$ $\longrightarrow$ O + SO	2.93 e15	0.00	50,450	T_{tr}	T_{tr}	G2M(RCC2)//B3LYP/6-311+(3df)	[81]
91	O + SO $\longrightarrow$ S + O$_2$	1.81 e13	0.00	6,980	T_{tr}	T_{tr}	G2M(RCC2)//B3LYP/6-311+(3df)	[81]

Appendix C

Transition State Data

Table C.1: Transition state information for air-SF_6 plasma "interfacial" reactions. All free-energy changes are relative to the reactants.

No.	Reaction	$\Delta G^\ddagger$, ΔG_p [kJ/mol]	Frequencies [cm^{-1}]	Level of Theory
72	$F + NO + M \longrightarrow NOF + M$	16.7, -278.3	324.1885i, 158.5606, 1192.4994	MP2/cc-pvtz
73	$NF_2 + N \longrightarrow NF + NF$	253.2, -26.9	1186.3569i, 151.5379, 236.2114, 283.6214, 465.9030, 1164.2932	MP2/cc-pvtz
74	$NF_2 + O \longrightarrow NF + FO$	279.8, 216.5	702.5305i, 89.0953, 150.2313, 184.7214, 332.5108, 1188.5001	MP2/cc-pvtz
75	$NF_2 + S \longrightarrow NF + SF$	198.0, 235.4	1532.8621i, 126.8645, 177.8898, 342.4132, 527.7852, 1154.3936	MP2/cc-pvtz
76.1	$SN + O + M \longrightarrow NSO + M$	71.8, 82.8	563.2092i, 335.8400, 1994.8013	MP2/cc-pvtz
76.2	$NSO + M \longrightarrow S + NO + M$	190.9, 103.3	375.9086i, 151.3135, 1088.3400	MP2/cc-pvtz
77.1	$OSN + M \longrightarrow S + NO + M$	57.0, -116.0	1301.3127i, 319.7563, 1176.2518	MP2/cc-pvtz
77.2	$OSN + M \longrightarrow SO + N + M$	160.2, 84.5	1107.6894i, 273.8308, 897.2407	MP2/cc-pvtz
78	$S_2O + M \longrightarrow S_2 + O + M$	465.2, 503.1	188.6108i, 103.8507, 1074.2998	MP2/cc-pvtz
79	$SO_2 + F + M \longrightarrow SO_2F + M$	36.7, -157.4	225.3639i, 81.8528, 320.1333, 497.8940, 1116.0383, 1359.6358	MP2/cc-pvtz
80	$NOF + M \longrightarrow NF + O + M$	433.4, 469.0	313.7499i, 71.2617, 1289.3818	MP2/6-311+G(3df)
81	$S_2 + O \longrightarrow S + SO$	26.6, -97.5	694.8930i, 182.8642, 537.0580	MP2/6-311+G(3df)
82	$SF + O \longrightarrow SO + F$	12.3, -87.0	309.3966i, 189.3266, 851.4581	MP2/6-311+G(3df)

Appendix D

Transport Coefficient Data

Table D.1: Neutral species, pure-gas $\Omega_{s,s}^{(1,1)*}$ collision integral curve-fit parameters.

Species	A	B	C
F	5.4945e-04	-2.4410e-01	3.2415e+00
F_2	-1.2582e-02	1.4232e-02	2.5137e+00
FO	-1.4768e-02	2.8663e-02	2.5210e+00
N	-6.2678e-03	-1.4634e-01	3.1436e+00
N_2	-1.3553e-02	2.6309e-02	2.6041e+00
NF	-1.6502e-02	5.1887e-02	2.5114e+00
NF2	-1.7368e-02	8.4563e-02	2.4758e+00
NO	-1.3160e-02	2.0396e-02	2.5887e+00
NOF	-1.5584e-02	7.0169e-02	2.4713e+00
NSO	-1.1531e-02	-1.9666e-02	3.3013e+00
O	-2.8100e-03	-2.0039e-01	3.2125e+00
O_2	-1.2561e-02	1.0836e-02	2.5816e+00
OSN	-1.3519e-02	1.4596e-02	3.0867e+00
S	-1.7641e-02	7.3045e-02	2.5805e+00
S_2	-1.4813e-02	3.8003e-02	3.0258e+00
S_2O	-5.1270e-03	-1.1297e-01	3.7503e+00
SF	-1.7338e-02	8.3596e-02	2.5986e+00
SF_2	-1.2588e-02	2.1444e-02	2.9099e+00
SF_3	-8.8107e-03	-5.8271e-02	3.3683e+00
SF_4	-2.7140e-03	-1.5174e-01	3.7882e+00
SF_5	9.8399e-04	-2.3188e-01	4.2171e+00
SF_6	6.2636e-03	-3.1331e-01	4.5737e+00
SN	-1.7643e-02	8.6665e-02	2.6248e+00
SO	-1.5889e-02	7.3247e-02	2.6411e+00
SO_2	-1.3160e-02	2.9870e-02	2.9082e+00
SO_2F	-1.1781e-02	-7.0316e-03	3.1221e+00
SO_2F_2	-4.3485e-03	-1.2306e-01	3.6621e+00
SOF_2	-9.5259e-03	-3.1999e-02	3.2121e+00

Table D.2: Neutral species, pure-gas $\Omega_{s,s}^{(2,2)*}$ collision integral curve-fit parameters.

Species	A	B	C
F	-9.9872e-04	-2.1133e-01	3.2341e+00
F_2	-1.7427e-02	1.1026e-01	2.1918e+00
FO	-2.0180e-02	1.3651e-01	2.1517e+00
N	-9.9508e-03	-7.3709e-02	2.9614e+00
N_2	-1.8603e-02	1.2682e-01	2.2615e+00
NF	-2.2254e-02	1.6729e-01	2.1056e+00
NF2	-2.2566e-02	1.9353e-01	2.0747e+00
NO	-1.8132e-02	1.1918e-01	2.2547e+00
NOF	-2.0722e-02	1.7551e-01	2.0889e+00
NSO	-1.3478e-02	3.6027e-02	3.1116e+00
O	-5.4653e-03	-1.4711e-01	3.1178e+00
O_2	-1.7412e-02	1.0696e-01	2.2609e+00
OSN	-1.6236e-02	8.3632e-02	2.8411e+00
S	-2.3466e-02	1.9115e-01	2.1561e+00
S_2	-1.8143e-02	1.1739e-01	2.7376e+00
S_2O	-5.6975e-03	-8.3305e-02	3.6704e+00
SF	-2.2329e-02	1.8967e-01	2.2068e+00
SF_2	-1.5921e-02	9.8682e-02	2.6298e+00
SF_3	-1.0169e-02	-1.3735e-02	3.2255e+00
SF_4	-2.7139e-03	-1.3258e-01	3.7531e+00
SF_5	2.5632e-03	-2.3953e-01	4.2992e+00
SF_6	8.6876e-03	-3.3754e-01	4.7277e+00
SN	-2.2831e-02	1.9588e-01	2.2220e+00
SO	-2.0766e-02	1.7575e-01	2.2643e+00
SO_2	-1.6674e-02	1.1029e-01	2.6153e+00
SO_2F	-1.4186e-02	5.5789e-02	2.9023e+00
SO_2F_2	-4.8239e-03	-9.5435e-02	3.5906e+00
SOF_2	-1.1690e-02	2.5232e-02	3.0148e+00

Table D.3: Polarizabilities, α, and effective electron count, N_{eff}, for collision integral equilibrium radii, r_e, using Lennard-Jones like phenomenological model potential [39]. Level of theory corresponds to ab-initio results computed in this work for polarizability calculations. Atoms/molecules with atypical ground spin multiplicities have their spin multiplicities, s, explicitly stated.

Species	α [Å^3]	$N_{\text{in/bond}}$ [-]	$N_{\text{out/nonbond}}$ [-]	Multiplicity s [-]	Level of Theory
F	0.438	2	7	2	MP2/6-311+G(3df)
F$^-$	0.980	2	8	1	MP2/6-311+G(3df)
F$_2$	1.070	2	12	1	MP2/6-311+G(3df)
FO	1.231	2	11	2	MP2/6-311+G(3df)
N	0.999	2	5	4	MP2/6-311+G(3df)
N$^+$	0.551	2	4	3	MP2/6-311+G(3df)
N$_2$	1.694	4	6	1	MP2/6-311+G(3df)
N$_2^+$	2.460	4	5	2	MP2/6-311+G(3df)
NF	1.560	2	10	3	MP2/6-311+G(3df)
NF2	2.038	4	15	2	MP2/6-311+G(3df)
NO	1.491	4	7	2	MP2/6-311+G(3df)
NO$^+$	1.031	4	6	1	MP2/6-311+G(3df)
NOF	1.837	6	12	1	MP2/6-311+G(3df)
NSO	5.460	6	11	4	MP2/6-311+G(3df)
O	0.652	2	6	3	MP2/6-311+G(3df)
O$^+$	0.364	2	5	2	MP2/6-311+G(3df)
O$_2$	1.287	4	8	3	MP2/6-311+G(3df)
O$_2^+$	0.777	4	7	2	MP2/6-311+G(3df)
OSN	4.574	4	13	4	MP2/6-311+G(3df)
S	2.587	10	6	3	MP2/6-311+G(3df)
S$^+$	1.578	10	5	2	MP2/6-311+G(3df)
S$_2$	5.555	4	8	3	MP2/6-311+G(3df)
S$_2$O	6.449	8	10	1	MP2/6-311+G(3df)
SF	2.970	2	11	2	MP2/6-311+G(3df)
SF$_2$	3.307	4	16	1	MP2/6-311+G(3df)
SF$_3$	3.900	6	21	2	MP2/6-311+G(3df)
SF$_4$	3.994	8	26	1	MP2/6-311+G(3df)
SF$_5$	4.313	10	31	2	MP2/6-311+G(3df)
SF$_6$	4.310	12	36	1	MP2/6-311+G(3df)
SN	3.453	4	7	2	MP2/6-311+G(3df)
SO	3.222	4	8	1	MP2/6-311+G(3df)
SO$_2$	3.759	8	10	1	MP2/6-311+G(3df)
SO$_2$F	3.857	10	14	2	MP2/6-311+G(3df)
SO$_2$F$_2$	4.117	12	20	1	MP2/6-311+G(3df)
SOF$_2$	3.861	8	16	1	MP2/6-311+G(3df)

Bibliography

[1] R Earl Good and Joseph J Rossi. An injection system for alleviation of radio blackout during re-entry. *Air Force Cambridge Research Laboratories Report*, (AFCRL-66-160), 1966.

[2] Graham V Candler, Heath B Johnson, Ioannis Nompelis, Pramod K Subbareddy, Travis W Drayna, and Vladimyr Gidzak. Development of the us3d code for advanced compressible and reacting flow simulations. *53rd AIAA Aerospace Sciences Meeting*, (AIAA 2015-1893), January, 2015.

[3] Kojiro Suzuki and Yasumasa Watanabe. Study on chemical factory in hypersonic wind tunnel flow using ablation and electric discharge. *44th AIAA Thermophysics Conference*, (2013-2773), June, 2013.

[4] John D Anderson Jr. *Hypersonic and High-Temperature Gas Dynamics*. AIAA, Reston, Virginia, second edition edition, 2006.

[5] Michael J Wright, Graham V Candler, and Deepak Bose. A data-parallel line relaxation method for the navier-stokes equations. *13th Computational Fluid Dynamics Conference*, (AIAA-97-2046), 1997.

[6] R Earl Good. Electron attachment to atomic fluorine in thermally ionized air. *NASA Contractor Report*, (NASA CR-516), 1966.

[7] Christopher A Grasso, Joseph E Riedel, and Andrew T Vaughan. Reactive sequencing for autonomous navigation evolving from phoenix entry, descent, and landing. *SpaceOps 2010 Conference*, (2010-2221), 2010.

[8] Conventional prompt global strike and long-range ballistic missiles: Backgrounds and issues. *Congressional Research Service Report*, (R41464), January, 2019.

[9] David E Mather, Jeffrey M Pasqual, Jamey P Sillence, and Paul Lewis. Radio frequency (rf) blackout during hypersonic reentry. *AIAA/CIRA 13th International Space Planes and Hypersonics Systems and Technologies*, (2005-3443), 2005.

[10] Tony C Lin, L K Sproul, D W Hall, and John Sontowski. Reentry plasma on electromagnetic wave propagation. *26th AIAA Plasmadynamics and Lasers COnference*, (95-1942), June, 1995.

[11] Minseok Jung, Hisashi Kihara, Ken Abe, and Yusuke Takahashi. Numerical simulation of plasma flows and radio-frequency blackout in atmospheric reentry demonstrator mission. *47th AIAA Fluid Dynamics Conference*, (2017-3308), June, 2017.

[12] Ryan P Starkey. Electromagnetic wave/magnetoactive plasma sheath interaction for hypersonic vehicle telemetry blackout analysis. *34th AIAA Plasmadynamics and Lasers Conference*, (2003-4167), June, 2003.

[13] F G Blottner. Prediction of the electron number density distribution in the laminar air boundary layer on sharp and blunt bodies. *AIAA Fluid and Plasma Dynamics Conference*, June, 1968.

[14] E S Levinsky and F L Fernandez. Approximate nonequilibrium air ionization in hyersonic flows over sharp cones. *AIAA Journal*, 2(3), March, 1964.

[15] V H Shui, P L Singh, B Kivel, and E R Bressel. Electron attachment at high temperatures. *AIAA 17th Aerospace Sciences meeting*, (AIAA 79-0252), 1979.

[16] Yusuke Takahashi, Kazuhiko Yamada, and Takashi Abe. Prediction performance of blackout and plasma attenuation in atmospheric reentry demonstrator mission. *Journal of Spacecraft and Rockets*, 51(6):1954–1964, 2014.

[17] Daniil A Andrienko and Iain D Boyd. Simulation of o_2-n collisions on *ab-initio* potential energy surfaces. *54th AIAA Aerospace Sciences Meeting*, (AIAA 2016-1249), January, 2016.

[18] Daniil A Andrienko and Iain D Boyd. Master equation simulation of o_2-n_2 collisions on an ab-inition potential energy surface. *47th AIAA Thermophysics Conference*, (AIAA 2017-3163), June, 2017.

[19] Paolo Valentini and Thomas E Schwartzentruber. Ab initio based model for high temperature nitrogen rovibrational excitation and dissociation. *54th AIAA Aerospace Sciences Meeting*, (AIAA 2016-0500), January, 2016.

[20] Ross S Chaudhry, Narendra Singh, maninder S Grover, Thomas E Schwartzentruber, and Graham V Candler. Implmentatino of a nitrogen chemical kinetics model based on *ab-Initio* data for hypersonic cfd. *AIAA 2018 Joint Thermophysics and Heat Transfer Conference*, (AIAA 2018-3439), June, 2018.

[21] Y B Zel'dovich. The oxidation of nitrogen in combustion and explosions. *Acta Physicochimica USSR*, 21:577–628, 1946.

[22] Roger C Millikan and Donald R White. Systematics of vibrational relaxation. *Journal of Chemical Physics*, 39, August, 1963.

[23] Chul Park. Assessment of two-temperature kinetic mmodel for ionizing air. *AIAA 22nd Thermophysics Conference*, (3), June, 1987.

[24] Paolo Valentini, Thomas E Schwartzentruber, Jason D Bender, and Graham V Candler. Dynamics of nitrogen dissociation from direct molecular simulation. *Physical Review Fluids*, 1(043402), August, 2016.

[25] Hao yu Sun, Zhiwei Cui, Jiajie Wang, Yiping Han, Peng Sun, and Xiaowei Shi. Analysis of electromagnetic scattering characteristics of plasma sheat surrounding a hypersonic aerocraft based on high-order auxiliary differential equation finite-difference time-domain. *Physics of Plasmas*, (25, 063514), 2018.

[26] M. J. Frisch, G. W. Trucks, H. B. Schlegel, G. E. Scuseria, M. A. Robb, J. R. Cheeseman, G. Scalmani, V. Barone, G. A. Petersson, H. Nakatsuji, X. Li, M. Caricato, A. V. Marenich, J. Bloino, B. G. Janesko, R. Gomperts, B. Mennucci, H. P. Hratchian, J. V. Ortiz, A. F. Izmaylov, J. L. Sonnenberg, D. Williams-Young, F. Ding, F. Lipparini, F. Egidi, J. Goings, B. Peng, A. Petrone, T. Henderson, D. Ranasinghe, V. G. Zakrzewski, J. Gao, N. Rega, G. Zheng, W. Liang, M. Hada, M. Ehara, K. Toyota, R. Fukuda, J. Hasegawa, M. Ishida, T. Nakajima, Y. Honda, O. Kitao, H. Nakai, T. Vreven, K. Throssell, J. A. Montgomery, Jr., J. E. Peralta, F. Ogliaro, M. J. Bearpark, J. J. Heyd, E. N. Brothers, K. N. Kudin, V. N. Staroverov, T. A. Keith, R. Kobayashi, J. Normand, K. Raghavachari, A. P. Rendell, J. C. Burant, S. S. Iyengar, J. Tomasi, M. Cossi, J. M. Millam, M. Klene, C. Adamo, R. Cammi, J. W. Ochterski, R. L. Martin, K. Morokuma, O. Farkas, J. B. Foresman, and D. J. Fox. Gaussian16 Revision C.01, 2016. Gaussian Inc. Wallingford CT.

[27] Giuseppe M. J. Barca, Colleen Bertoni, Laura Carrington, Dipayan Datta, Nuwan De Silva, J. Emiliano Deustua, Dmitri G. Fedorov, Jeffrey R. Gour, Anastasia O. Gunina, Emilie Guidez, Taylor Harville, Stephan Irle, Joe Ivanic, Karol Kowalski, Sarom S. Leang, Hui Li, Wei Li, Jesse J. Lutz, Ilias Magoulas, Joani Mato, Vladimir Mironov, Hiroya Nakata, Buu Q. Pham, Piotr Piecuch, David Poole, Spencer R. Pruitt, Alistair P. Rendell, Luke B. Roskop, Klaus Ruedenberg, Tosaporn Sattasathuchana, Michael W. Schmidt, Jun Shen, Lyudmila Slipchenko, Masha Sosonkina, Vaibhav Sundriyal, Ananta Tiwari, Jorge L. Galvez Vallejo, Bryce Westheimer, Marta Wloch, Peng Xu, Federico Zahariev, and Mark S. Gordon. Recent developments in the general atomic and molecular electronic structure system. *The Journal of Chemical Physics*, 152(15):154102, April 2020.

[28] Connie W. Gao, Joshua W. Allen, William H. Green, and Richard H. West. Reaction Mechanism Generator: Automatic construction of chemical kinetic mechanisms. *Computer Physics Communications*, 203:212–225, 2016.

[29] Aleksandr O Lykhin, Danil S Kaliakin, Gwen E DePolo, Alexander A Kuzubov, and Sergey A Varganov. Nonadiabatic transition state theory: Application to intersystem crossings in the active sites of metal-sulfur proteins. *International Journal of Quantum Chemistry*, 116(10):750–761, 2016.

191

[30] Aleksandr O Lykhin and Sergey A Varganov. Intersystem crossing in tunneling regime: T1   S0 relaxation in thiophosgene. *Phys. Chem. Chem. Phys.*, 22(10):5500–5508, 2020.

[31] Peter A Gnoffo, Roop N Gupta, and Judy L Shinn. Conservation equations and physical models for hypersonic air flows in thermal and chemical nonequilibrium. *NASA Technical Paper*, (2867), 1989.

[32] E. V. Kustova and G. P. Oblapenko. Reaction and internal energy relaxation rates in viscous thermochemically non-equilibrium gas flows. *Physics of Fluids*, 27(1), 2015.

[33] Brian Freno, Brian Carnes, and V G. Weirs. Code-Verification Techniques for Hypersonic Reacting Flow in Thermochemical Nonequilibrium. pages 1–28, 2019.

[34] Jong Hun Lee. *Basic Governing Equations for the Flight Regimes of Aeroassisted Orbital Transfer Vehicles.* 1984.

[35] Graham V. Candler and Robert W. MacCormack. Computation of weakly ionized hypersonic flows in thermochemical nonequilibrium. *Journal of Thermophysics and Heat Transfer*, 5(3):266–273, 1991.

[36] Chul Park. Review of chemical-kinetic problems of future NASA missions, I: Earth entries. *Journal of Thermophysics and Heat Transfer*, 7(3):385–398, 1993.

[37] Paul V. Marrone and Charles E. Treanor. Chemical relaxation with preferential dissociation from excited vibrational levels. *Physics of Fluids*, 6(9):1215–1221, 1963.

[38] David L Miller, Justin C Schoof, and Michael L Hobbs. Thermochemical plots using JCZS2i piece-wise curve fits. (October), 2013.

[39] A. Laricchiuta, G. Colonna, D. Bruno, R. Celiberto, C. Gorse, F. Pirani, and M. Capitelli. Classical transport collision integrals for a Lennard-Jones like phenomenological model potential. *Chemical Physics Letters*, 445(4-6):133–139, 2007.

[40] James R. Stallcop, Harry Partridge, and E. Levin. Collision integrals for the interaction of the ions of nitrogen and oxygen in a plasma at high temperatures and pressures. *Physics of Fluids B*, 4(2):386–391, 1992.

[41] Grant E. Palmer and Michael J. Wright. Comparison of methods to compute high-temperature gas viscosity. *Journal of Thermophysics and Heat Transfer*, 17(2):232–239, 2003.

[42] R N Gupta, J M Yos, R A Thompson, and K.-P. Lee. A Review of Reaction Rates and Thermodynamic and Transport Properties for an 11 Species Air Model for Chemical and Thermal Nonequilibrium Calculations to 30 000 K. (1232), 1990.

[43] Kenneth Sutton and Peter A. Gnoffo. Multi-component diffusion with application to computational aerothermodynamics. *7th AIAA/ASME Joint Thermophysics and Heat Transfer Conference*, 1998.

[44] L Spitzer. *Physics of Fully Ionized Gases*. Interscience, New York, 1962.

[45] J Hirschfelder, R Byron Bird, and Charles F Curtiss. *Molecular theory of gases and liquids; rev. version*. Structure of matter series. Wiley, New York, NY, 1964.

[46] Terry N. Olney, N.M. Cann, Glyn Cooper, and C.E. Brion. Absolute scale determination for photoabsorption spectra and the calculation of molecular properties using dipole sum-rules. *Chemical Physics*, 223(1):59–98, October 1997.

[47] A. B. Murphy and C. J. Arundell. Transport coefficients of argon, nitrogen, oxygen, argon-nitrogen, and argon-oxygen plasmas. *Plasma Chemistry and Plasma Processing*, 14(4):451–490, December 1994.

[48] A. B. Murphy. Transport coefficients of air, argon-air, nitrogen-air, and oxygen-air plasmas. *Plasma Chemistry and Plasma Processing*, 15(2):279–307, June 1995.

[49] Junwei Lucas Bao and Donald G. Truhlar. Variational transition state theory: theoretical framework and recent developments. *Chemical Society Reviews*, 46(24):7548–7596, 2017.

[50] Carl Eckart. The penetration of a potential barrier by electrons. *Phys. Rev.*, 35:1303–1309, Jun 1930.

[51] Harold S Johnston and Julian Heicklen. Tunneling corrections for unsymmetrical eckart potential energy barriers. *The Journal of Physical Chemistry*, 66(3):532–533, 1962.

[52] Joshua W. Allen, C. Franklin Goldsmith, and William H. Green. Automatic estimation of pressure-dependent rate coefficients. *Phys. Chem. Chem. Phys.*, 14(3):1131–1155, 2012.

[53] A.Y. Chang, J.W. Bozzelli, and A.M. Dean. Kinetic analysis of complex chemical activation and unimolecular dissociation reactions using QRRK theory and the modified strong collision approximation. *Zeitschrift für Physikalische Chemie*, 214(11), January 2000.

[54] F Lindemann. Discussion on "the radiation theory of chemical action". *Transactions of Faraday Society*, 17:598, 1922.

[55] Vsevolod D. Dergachev, Mitra Rooein, Ilya D. Dergachev, Aleksandr O. Lykhin, Robert C. Mauban, and Sergey A. Varganov. NAST: Nonadiabatic statistical theory package for predicting kinetics of spin-dependent processes. *Topics in Current Chemistry*, 380(2), February 2022.

[56] Dmitri G. Fedorov, Shiro Koseki, Michael W. Schmidt, and Mark S. Gordon. Spin-orbit coupling in molecules: Chemistry beyond the adiabatic approximation. *International Reviews in Physical Chemistry*, 22(3):551–592, July 2003.

[57] Elliot H. Lieb. Variational principle for many-fermion systems. *Physical Review Letters*, 46(7):457–459, February 1981.

[58] C. C. J. Roothaan. New developments in molecular orbital theory. *Reviews of Modern Physics*, 23(2):69–89, April 1951.

[59] G. G. Hall. The molecular orbital theory of chemical valency VIII. a method of calculating ionization potentials. *Proceedings of the Royal Society of London. Series A. Mathematical and Physical Sciences*, 205(1083):541–552, March 1951.

[60] Chr. Møller and M. S. Plesset. Note on an approximation treatment for many-electron systems. *Physical Review*, 46(7):618–622, October 1934.

[61] Dieter Cremer. Møller-plesset perturbation theory: from small molecule methods to methods for thousands of atoms. *Wiley Interdisciplinary Reviews: Computational Molecular Science*, 1(4):509–530, May 2011.

[62] Marshall C. Galbraith, Steven Allmaras, and David L. Darmofal. A verification driven process for rapid development of CFD software. In *53rd AIAA Aerospace Sciences Meeting*. American Institute of Aeronautics and Astronautics, January 2015.

[63] David L. Darmofal, Steven Allmaras, and Masayuki Yano. An adaptive, higher-order discontinuous galerkin finite element method for aerodynamics. In *21st AIAA Computational Fluid Dynamics Conference*. American Institute of Aeronautics and Astronautics, June 2013.

[64] Masayuki Yano and David L. Darmofal. An optimization-based framework for anisotropic simplex mesh adaptation. *Journal of Computational Physics*, 231(22):7626–7649, 2012.

[65] Hugh Alexander Carson. *Provably Convergent Anisotropic Output-Based Adaptation for Continuous Finite Element Discretizations*. PhD thesis, Massachusetts Institute of Technology, Department of Aeronautics and Astronautics, February 2019.

[66] Arthur C. Huang. *An Adaptive Variational Multiscale Method with Discontinuous Subscales for Aerodynamic Flows*. PhD thesis, Massachusetts Institute of Technology, Department of Aeronautics and Astronautics, February 2020.

[67] Benjamin Luke Streatfield Couchman. *Application of Output-Based Adaptation to Hypersonic Problems*. PhD thesis, Massachusetts Institute of Technology, Department of Aeronautics and Astronautics, To Appear 2022.

[68] Marshall C Galbraith, Steven R Allmaras, and David L Darmofal. A verification driven process for rapid development of cfd software. *53rd AIAA Aerospace Sciences Meeting*, January, 2015.

[69] Kevin M. Sabo, Benjamin L. Couchman, Wesley L. Harris, and David L. Darmofal. Investigation of Thermochemical Non-Equilibrium Models in Hypersonic Flows Using Output-Based grid Adaptation. *AIAA Science and Technology Forum and Exposition, AIAA SciTech Forum 2022*, pages 1–24, 2022.

[70] Georgy Shoev and Yevgeniy Bondar. Numerical study of non-equilibrium gas flows with shock waves by using the Navier-Stokes equations in the two-temperature approximation. *AIP Conference Proceedings*, 1770(2016), 2016.

[71] Brian Carnes, V. G. Weirs, and Thomas Smith. *Code verification and numerical error estimation for use in model validation of laminar, hypersonic double-cone flows.* 2019.

[72] G. P. Oblapenko. Calculation of vibrational relaxation times using a kinetic theory approach. *The Journal of Physical Chemistry A*, 122(50):9615–9625, November 2018.

[73] David G. Goodwin, Raymond L. Speth, Harry K. Moffat, and Bryan W. Weber. Cantera: An object-oriented software toolkit for chemical kinetics, thermodynamics, and transport processes. `https://www.cantera.org`, 2021. Version 2.5.1.

[74] Jeffrey I Steinfeld, Joseph S Francisco, and William L Hase. *Chemical Kinetics and Dynamics.* Prentice-Hall, Inc., Englewood Cliffs, NJ, 1989.

[75] Bryan M. Wong, David M. Matheu, and William H. Green. Temperature and molecular size dependence of the high-pressure limit. *The Journal of Physical Chemistry A*, 107(32):6206–6211, July 2003.

[76] Michael Wright, Mark Loomis, and Periklis Papadopoulos. Aerothermal analysis of the project fire II afterbody flow. *Journal of Thermophysics and Heat Transfer*, 17(2):240–249, April 2003.

[77] Michael J. Wright, Dinesh K. Prabhu, and Edward R. Martinez. Analysis of apollo command module afterbody heating part i: AS-202. *Journal of Thermophysics and Heat Transfer*, 20(1):16–30, January 2006.

[78] Soshi Kawai and Sanjiva Lele. Mechanisms of jet mixing in a supersonic crossflow: A study using large-eddy simulation. *44th AIAA/ASME/SAE/ASEE Joint Propulsion Conference and Exhibit*, pages 1–16, July 2008.

[79] R Girard, J B Belhaouari, J J Gonzalez, and A Gleizes. A tow-temperature kinetic model of SF_6 plasma. *Journal of Physics D : Applied Physics*, 32:2890–2901, 1999.

[80] Yuwei Fu, Mingzhe Rong, Kang Yang, Aijun Yang, Xiaohua Wang, Qingqing Gao, Dingxin Liu, and Anthony B. Murphy. Calculated rate constants of the chemical reactions involving the main byproducts SO2F, SOF2, SO2F2 of SF6 decomposition in power equipment. *Journal of Physics D: Applied Physics*, 49(15), 2016.

[81] Chih Wei Lu, Yu Jong Wu, Yuan Pern Lee, R. S. Zhu, and M. C. Lin. Experiments and Calculations on Rate Coefficients for Pyrolysis of SO2 and the Reaction O + SO at High Temperatures. *Journal of Physical Chemistry A*, 107(50):11020–11029, 2003.